Mechanical competition triggered by innate immune signaling drives the collective extrusion of bacterially-infected epithelial cells

Effie E. Bastounis[1], Francisco S. Alcalde[2], Prathima Radhakrishnan[1,3], Patrik Engström[4], María J. Gómez Benito[2], Matthew Welch[4], José M. García Aznar[2], Julie A. Theriot[1,+]

[1]*Department of Biology and Howard Hughes Medical Institute, University of Washington,* Seattle, WA, USA

[2]*Department of Mechanical Engineering, University of Zaragoza, Zaragoza, Spain*

[3]*Biophysics Program, Stanford University,* Stanford, CA, USA

[4]*Department of Molecular and Cell Biology, University of California Berkeley, Berkeley, CA, USA*

[+] Corresponding Author:

Julie A. Theriot, Ph.D.
Department of Biology
University of Washington
Life Sciences Building, Room 575
Box 351800
Seattle, WA 98195-1800
USA

Email: jtheriot@uw.edu
Phone: (206) 543-3397

ABSTRACT

Intracellular bacterial pathogens often reprogram their mammalian host cells, including cell mechanical properties, to promote their own replication and spread. However, it is unclear whether mammalian host cells may modulate their biomechanics in response to infection in a way that would benefit the host by limiting bacterial infection. Inspired by this question, we monitored epithelial cell monolayers infected with low levels of *Listeria monocytogenes.* We found that, as the bacteria replicate and spread from cell to cell over several days, the infected host cells within the infection focus get progressively compressed by surrounding uninfected cells. Surrounding uninfected cells become highly polarized and move directionally towards the infection focus, squeezing the infected cells that eventually get extruded from the monolayer. Extruded cells continue adhering to the cellular monolayer, giving rise to a 3-dimensional (3D) mound of infected cells. We hypothesized that 3D mounding was driven by changes in the biomechanics of uninfected cells surrounding the mounds (surrounders) as well as the infected cells that eventually compose the mound (mounders). Indeed, we found that infected mounders, but not surrounders, become softer during infection and adhere more weakly on deformable matrices mimicking their natural environment. Through a combination of transcriptomics, pharmacological and genetic perturbations, we find that differentially upregulated innate immunity signaling, and downregulated cell-cell and cell-matrix adhesion pathways synergistically can drive the observed cellular competition between infected mounders and surrounders. Most importantly we find that activation of NF-κB is critical for mound formation, and show evidence that our findings extend to bacterial pathogens other than *L. monocytogenes*. Overall, our findings highlight the dynamic remodeling capability of epithelial tissue, and propose a novel biomechanical mechanism employed by host epithelial cells to eliminate bacterial infection.

INTRODUCTION

During the progression of bacterial infection, host cells and pathogens communicate with one another using a wide variety of chemical and biochemical signals. Also important, but sometimes underappreciated, are mechanical signals that contribute to host-pathogen communication. Example of mechanical signals include the forces that cells are able to transduce to each other and to their extracellular matrix. These cell-generated forces are critical for maintaining tissue integrity and barrier functions.

The biomechanical interactions between host cells and bacterial pathogens are dictated by both the pathogen and the host. It has been previously shown that there are ways through which intracellular pathogens can manipulate host cell functions, including host cell mechanotransduction, in order to spread more efficiently[1-3]. Rajabian *et al* showed that secreted *Listeria monocytogenes* (*L.m.*) toxin InlC reduces host epithelial cell cortical tension to promote bacterial cell-to-cell spread[3], showcasing that actin-based motility triggered by the polymerization of host cell actin behind the moving bacteria is not the sole force *L.m.* uses in order to power its intercellular spread. Similarly, we showed that when *L.m*. crosses through basement membranes such as those of the placenta, it secretes the InlP toxin which leads to a weakening of the tensional forces between host epithelial cells and their extracellular matrix, thus facilitating apico-basal bacterial spread[4]. *Rickettsia parkeri*, a bacterial pathogen that undergoes actin based motility like *L.m.*, powers its intracellular spread by reducing intercellular tension between host epithelial cells through secretion of the effector protein Sca4 that disrupts cell-cell junctions[1].

All the above studies examine how bacteria can manipulate host cell mechanics to promote their spread. However, it is very plausible that host cells could recognize bacterial pathogens and mount a response against them by actively changing their mechanics. In the past it has been suggested that in the intestinal epithelium proliferating stem cells at the crypts of the intestine drive the motion of cells upwards with cells extruding occasionally at the apex of the intestinal villi. These cell extrusion events can have dual, opposing effects when it comes to *L.m.* infection. They can grant *L.m.* the opportunity to easily access E-cadherin on host epithelial cells lining the intestinal villi and infect them, but they could also emerge as a result of a mechanism that host cells employ to get rid of already infected cells. The latter would be beneficial for the host since infected extruded cells would be eliminated through the fecal route[5]. Cell compression can lead to apoptosis and subsequent cell extrusion[6] and mechanisms proposed depend on cell confluency and include lamellipodial protrusions of cells surrounding

the extruded cell or a “purse-string” actomyosin ring formed around the extruding cell[7]. However, whether *L.m.*-infected epithelial cells undergo apoptosis and get extruded and what are the mechanisms, mechanical and biochemical, regulating such process remains obscure.

To address this question, we monitored epithelial cell monolayers infected with low levels of *L.m.* and found that as the bacteria replicate and spread intercellularly, the host cells pertaining in the infection focus (infected mounders) get progressively squeezed and eventually collectively extruded by surrounding uninfected cells (surrounders). We discovered that this process of massive infected cell extrusion (infection mounding) is driven by changes in cellular stiffness and force transduction that the two battling cell populations, the surrounders and the infected mounders, undergo. Consistent with this finding, when we perturbed host cell mechanotransduction by means of pharmacological or genetic perturbations, we found that actomyosin contractility contributes to infection mounding but cell-cell force transduction through adherens junctions is necessary. Moreover, we found that infected cell death follows infected cell extrusion and that innate immunity signals and specifically NF-κB activation are drivers in this mechanical competition that is not limited solely to infection by *L.m..* Overall, our findings underline the dynamic remodeling capability of epithelial tissue and propose mechanical forces being a major driver employed by host epithelial cells to eliminate bacterial infection.

RESULTS

Infection with *Listeria monocytogenes* induces changes in the organization and kinematic behavior of host epithelial cells

To address whether infection elicits changes in the kinematic behavior of host cells, we infected Madin-Darby Canine Kidney (MDCK) epithelial cells grown in a confluent monolayer on glass coverslips with wild-type *L. monocytogenes* (*L.m.*). We used a low multiplicity of infection so that on average fewer than one in 10^3 host cells was invaded, resulting in well-spaced infectious foci that could be observed over a period of several days. Cells were maintained with the membrane-impermeable antibiotic gentamicin in the culture medium so that bacteria could only spread directly from cell to cell using actin-based motility, and the *L.m.*-infected foci grew to include several hundred host cells over a period of 24-48 h. Whereas MDCK cells in uninfected monolayers exhibited regularly spaced nuclei confined to a single plane (Fig. 1A), cells in *L.m.*-infected foci formed large three-dimensional mounds over the time of observation, with host cells piling on top of one another to form structures up to 50 μm tall (Fig. 1B). We observed formation of similar infection mounds in monolayers of human A431D epithelial cells, indicating that this phenomenon is not unique to canine epithelial cells (Fig. S1B-C).

Formation of these large mounds was due to active directional movement by the host cells. From 24 h post-infection (pI) onwards, we monitored the movement of Hoechst-stained host cell nuclei via time-lapse confocal 3D microscopy. Uninfected MDCK cells in confluent monolayers moved randomly with very low speeds and rarely translocated more than a fraction of one cell diameter over 20 hours, appearing to be confined by their neighbors (Suppl. Movie 1; Fig. 1C, 1F). In contrast, *L.m.*-infected cells within foci and their nearby uninfected neighbors all moved rapidly and persistently toward the center of the focus, and the infected cells also moved upward, away from the cover slip, to form the three-dimensional mound (Suppl. Movie 2; Fig. 1D, 1G). Net cell speeds inside and near *L.m.*-infected foci increased by more than 3-fold relative to uninfected monolayers (Fig. 1E), and cell tracks became significantly straighter (Fig. S1A). The dramatic nature of this change in cell behavior is better appreciated by examination of the mean squared displacement (MSD) for cells in uninfected vs. infected monolayers (Fig. 1H-I). Over 16 hours of observation, the average MSD for uninfected cells remained under 50 μm^2, indicating a net displacement of about 7 μm. Movement over this time frame was strongly constrained and appeared subdiffusive (see Fig. S1D), with the average MSD reaching a plateau, rather than continuing to grow linearly with time as would be expected for unconstrained random movement. In contrast, the average MSD for cells in and near *L.m.*-

infected foci grew to over 1000 μm^2 over this same time frame, and increased superdiffusively, faster than linear with time, indicative of directed motion (Fig. 1H-K). Altogether these findings indicate that the host cells undergo a behavioral phase transition during infection, switching from a caged state where they are tightly confined by their neighbors to a superdiffusive, highly motile state at late times post-infection. Such transitions from jammed to unjammed or fluid-like behavior have been previously described for epithelia undergoing the epithelial to mesenchymal transition (EMT) or for cells exposed to compressive forces (such as in the case of bronchospasm in asthmatic patients)[8] but never before for cells during bacterial infection.

These behavioral changes were accompanied by changes in cell size, shape and packing in the epithelial monolayer. To measure changes in cell morphology, we performed cell segmentation based on the pericellular localization of the adherens junction protein E-cadherin (Fig. S2A). We used the fluorescent signal from *L.m.* constitutively expressing red fluorescent protein to identify the cells containing the bacteria forming the infection mound ("mounder" cells) and their nearby uninfected neighbors ("surrounder" cells). In uninfected monolayers, the MDCK cells formed regularly packed polygons, with the long axis of each cell oriented randomly with respect to the center of the field of view (Fig. 2A). At foci in infected monolayers, the infected mounder cells at the center of the focus had significantly smaller projected 2D area than uninfected cells, and uninfected surrounders were also slightly smaller (Fig. 2A-B). Strikingly, the orientation of the long axis of the surrounders pointed toward the center of the focus, and this preferential orientation persisted over more than 100 μm from the site of the mound, equivalent to more than 10 cell diameters (Fig. 2A, C). These surrounder cells also showed significantly more alignment of their long axes with respect to their immediate neighbors, indicating an increase in local nematic order within the monolayer (Fig. S2B-C). In addition we calculated the aspect ratio AR and shape factor q (ratio of cell perimeter to square root of area), dimensionless numbers that have previously been used to characterize cell shape changes during EMT and the jamming to unjamming transition[9], and found increases for both values in both infected mounders and uninfected surrounders as compared to cells in uninfected monolayers (Fig. S2A, D-F).

The changes in cell morphology for both infected mounders and surrounders suggested that there might be cytoskeletal rearrangements associated with infection. We performed immunostaining on *L.m.*-infected samples at 24 h pI and examined them through confocal microscopy. We found that F-actin localized pericellularly for cells in uninfected wells, whereas in infected wells cells both mounder and surrounder cells contained far less pericellular actin,

while actin comet tails were readily visible in infected cells (Fig. 2D). In addition, surrounders exhibited prominent F-actin stress fibers compared to infected mounders and to uninfected cells (Fig. 2D). Microtubules were also disrupted in infected cells, as were the intermediate filaments vimentin and cytokeratin, with vimentin most strongly reduced in the infected mounders relative to uninfected surrounders (Fig. 2D and S3). Altogether, the decreased fluorescence intensity of vimentin, tubulin and cytokeratin for the infected mounders as compared to surrounders is consistent with these cells displaying distinct mechanical properties that could contribute to the formation of the 3D mounds. Alternatively, changes in the organization of cytoskeletal filaments could be the result of infected mounders being squeezed and/or extruded rather than the initial cause of mounding.

Mechanical competition between infected mounder cells and uninfected surrounder cells drives mound extrusion

We found that infected mounders and surrounders have distinct shape characteristics and cytoskeletal organization when compared to each other and to uninfected cells. This led us to hypothesize that the formation of an extruded mound might require competition between two cell populations with distinct biomechanical properties. Indeed, when we infected epithelial cells with a high multiplicity of infection (MOI) so that all cells became infected, we did not observe mound formation (Fig. 3A-B). This finding suggests that mound formation may not simply be a consequence of loss of cell-substrate adhesion by infected cells, but instead may require the involvement of uninfected surrounder cells in a form of mechanical competition.

To test whether there is a difference in the mechanical properties of the surrounders versus the infected mounders, we first used traction force microscopy (TFM) to measure cellular traction forces with respect to the substrate. In TFM as cells actively engage their focal adhesions they pull on their extracellular matrix depending on how well their focal adhesions are organized and connected to the underlying cytoskeleton[10, 11]. By doing so they deform the gels on which they attach inducing displacements of the beads that are embedded within those gels. We can measure those displacements by following the movement of the beads through time-lapse microscopy and can then calculate the forces that cells exert on their matrix (Suppl. Movie 3)[12]. To that end, we placed MDCK cells in confluence on soft 3 kPa collagen I-coated polyacrylamide hydrogels and subsequently infected them. Cells were followed by live time-lapse epifluorescence microscopy from 4 h to 3 days pI. We discovered that, as the infection focus grows, the cells within the mound adhere more weakly to their matrix as compared to

surrounding uninfected cells, as evidenced by the deformation maps where blue color signifies very low deformations imparted by mounders and the traction stress maps where gray signifies low traction stresses (Fig. 3C). In addition, when we converted the deformations into polar coordinates and looked at the radial deformations u_r, we found that the surrounders just at the edge of the infection mound exert large deformations grabbing the substrate and pulling it outwards (*i.e.* away from the mound) as they move directionally towards the center of the focus (Fig. 3C). Overall these dynamic changes in traction force generation patterns indicate that mound formation is not caused by contraction of the infected cells, but rather by active movement of the uninfected surrounders, forcefully engaging the substrate to actively crawl toward the center of the focus, squeezing and extruding the infected cells.

When we then constructed kymographs by calculating the average radial deformation and bacterial fluorescence intensity as a function of radial distance from the center of the mound and found that indeed the highest radial deformations coincide with the edge of the infection focus (Fig. 3D). Interestingly, when we looked in more detail these kymographs (Fig. S4A-B), we observed that starting 20 h pI, the positive peak of mean radial displacement u_r coincides with the mean *L.m.* fluorescence intensity reaching background levels, meaning that the largest outward-pointing displacements (away from the focus) are exerted by uninfected surrounder cells just at the edge of the infection focus (Fig. S4B). This behavior persists up to 54 h pI with the peak of forces moving outwards as the infection focus grows. However, after 54 h pI it is interesting that the peak bacterial fluorescence starts decreasing due to infected cells having extruded and bacteria being therefore unable to spread anymore to cells at the basal cell layer (Fig S4B). Concurrently, the traction forces rise up suggestive of uninfected cells repopulating the region where previously weakly adhering infected mounders previously resided (Suppl. Movie 3).

The decrease in the traction stresses of the infected mounders could be caused by secreted *L.m.* proteins previously suggested to weaken cellular tension by interacting with either cell-cell or cell-matrix adhesion complexes, like the internalins C (InlC)[3] and P (InlP)[2]. To examine if this hypothesis is true, we infected MDCK cells with *ΔinlC*$^-$ and with *ΔinlP*$^-$ mutants and assessed the ability of host cells to form infection mounds at 24 h pI under these conditions. Since the pore-forming toxin listeriolysin O (LLO) could also play a role by activating signaling pathways that could affect mechanotransduction, we also infected cells with LLO^{G486D} *L.m.* that exhibits 100x less hemolytic activity than the wild-type protein[13]. The reason we used this strain is because the L.m. completely lacking LLO (*hly*$^-$ *L.m.*) were unable to escape vacuoles and

thus spread in MDCK. In all cases we were able to observe infection mounds at 24 h pI. While we found no differences in mound size when comparing *ΔinlC*$^{-}$ and *ΔinlP*$^{-}$ to WT *L.m.* infection mounds, we found that infection with LLO^{G486D} *L.m.* led to formation of smaller infection mounds compared to the other conditions (Fig. S5A-B), however, it is worth noting that the bacterial load in the LLO^{G486D} *L.m.* mounds was also decreased, most probably because bacteria are unable to efficiently escape vacuoles (Fig. S5B). Altogether, these results suggest that neither InlC nor InlP secreted bacterial effectors contribute to infection mound formation, reinforcing the idea that this cellular competition leading to infection mounding might be determined by the host cells rather than by the bacteria.

The decrease in the forces that mounders exert on their matrix could be due to changes in the organization of the focal adhesions of the cells only or it could be due to changes in the cytoskeletal integrity of cells resulting in reduced ability of the cells to transduce forces. To determine whether the bulk cytoskeletal stiffness of cells changes upon infection, we used atomic force microscopy (AFM) to measure the stiffness of surrounders or mounders at 24 h pI as well as of uninfected cells. In AFM we use a flexible cantilever at whose end a small tip is attached. This tip “gently” touches the surface of cells and records the small force between the probe and the surface, letting us determine the height and elastic properties of cells (Fig. S6A). First, we used a conical shaped tip terminated with a 130 nm diameter sphere and performed force mapping comparing mounders still attached to their substrate with nearby surrounders. We found that surrounders were stiffer and more spread out as compared to mounders (Fig. S6A-B). Since smaller tips probe local cellular properties, we also used a larger 5 μm diameter tip to measure the bulk cellular stiffness (Fig. 3G and S6C). Similar to the results using the small conical tip, we found that stiffness of surrounders is 4-fold higher than of mounders (Fig. 3G). Interestingly, we found that, as compared to cells originating from uninfected wells, surrounders are 2.5-fold stiffer whereas infected mounders are 1.6-fold softer (Fig. 3G).

Combined with the TFM results described above, these measurements help us to describe the sequence of mechanical events that results in mound formation. As compared to the steady-state cell behavior in uninfected epithelial monolayers, infected cells become softer, and lose the ability to generate strong traction forces on their substrates. At the same time, the nearby uninfected surrounder cells, particularly those physically closest to the infected cells, become stiffer and directionally polarized, gripping the substrate and actively pulling on it to move themselves directionally and persistently toward the center of the focus. The mechanical competition between the surrounder cells and the infected mounder cells results in the

mounders getting squeezed and ejected from the plane of the monolayer. In the geometry associated with the primary site of *L.m.* infection in animal hosts, the small intestine, this active extrusion of infected cells driven by changes in the mechanical behavior of the uninfected surrounders would drive the infected cells to be shed into the intestinal lumen, where they could be eliminated from the body by the fecal route.

Cell-cell adhesions and actomyosin contractility contribute to mound formation

As infected mounders and surrounders differ in cellular stiffness, cell-matrix contractility and cytoskeletal organization, we hypothesized that if we were to perturb cell-matrix or cell-cell force transduction via pharmacological or genetic manipulation for both cell populations that would affect mound formation and prevent the collective extrusion of infected cells. We first tested how inhibition of cell-matrix contractility of both mounders and surrounders would impact infection mounding. For that we infected cells with *L.m.* and 4 h pI treated cells with vehicle control, the ROCK inhibitor Y27632, or the myosin II inhibitor blebbistatin to decrease actomyosin generated contractility (Fig. 4A-B). In both cases we found a significant reduction in mound size at 24 h pI (Fig. 4A). This result reinforces the idea that cell-matrix contractility of the surrounders is crucial to eliciting the squeezing and subsequent extrusion of infected mounders.

We then examined the role of cell-cell force transduction in eliciting infection mounding by either infecting Δα-Ecatenin knockout MDCK or E-cadherin knockdown MDCK with *L.m.* and comparing infection mounding with that of WT MDCK (Fig. 4C-D and S7A). We found that when cell-cell adhesions are depleted infection mound formation is almost abolished. When we then performed TFM to measure the cell-matrix forces that Δα-Ecatenin knockout MDCK cells exert as the infection focus grows, we were unable to observe any differences in the cell-matrix traction stresses of mounders versus surrounders (Fig. 4E and Suppl. Movie 4). This result suggests that cell-cell and cell-matrix forces are tightly coupled, and that a difference in force transduction between the two populations *(i.e.* the infected mounders and the surrounders) is necessary for infection mounding to occur. Interestingly, we found that that infection foci for Δα-Ecatenin knockout MDCK infected with *L.m.* at 24 h pI, were much larger than for WT MDCK but also less dense in fluorescence intensity (Fig. S7 B-E). This observation is consistent with the idea that mound formation limits the ability of bacteria to spread within the basal cell monolayer. Given this important result we then asked whether these findings could be reproduced in human A431D that we previously found to exhibit infection mounding, much like MDCK at 24 h pI. Indeed, when we mixed A431D cells not expressing E-cadherin with cells

expressing full length E-cadherin to a ratio of 100:1 (just to get a few cells infected since E-cadherin is the receptor for *L.m.* invasion) and then infected them with *L.m.* we were able to abolish mound formation (Fig. S7F-K). However, infection focus size in the latter case was smaller as compared to control, presumably because E-cadherin is important for cell-to-cell spread of *L.m.* (Fig. S7H). This result is also important because it suggests that infection mounding does not occur because host cells get overloaded with bacteria, since infection foci in the 100:1 mixture of A431D cells are much denser in *L.m.* fluorescence as compared to controls. Altogether these findings suggest that cell-matrix and especially cell-cell force transduction of cells during infection is critical for mound formation and for infected cell extrusion.

Inspired by the inhibition of infection mounding when cell-cell adhesions are perturbed, we then asked the question of what would happen if we infected monolayers with a mixture of cells capable and incapable of forming cell-cell junctions capable of force transmission. We mixed α-catenin knockout MDCK cells with WT cells expressing E-cadherin-RFP (to distinguish WT cells from mutants) in varying ratios, specifically 1:3, 1:1, 3:1. When most of the host cells were WT (100% and 75%), infection mounding occurs normally, while when the majority of cells were α-catenin knockout MDCK cells (100% and 75%), infection mounding did not occur. Intriguingly, when cells were mixed 1:1 we only observed infection mounding in the cases where infected mounders and immediate surrounders happened to be predominately WT in that region of the monolayer (Suppl. Movie 5 and Fig. S8A) but not otherwise (Suppl. Movie 6). This result suggests that the presence of functional E-cadherin-based cell-cell junctions, at least in the infected mounders and the uninfected cells immediately surrounding the infection mound, is necessary for infection mounding to occur.

Finally, to examine whether there are any differences in the organization of cell-cell adhesions during infection that could explain why lack of adherens junctions prohibits infection mounding, we performed immunostaining for a number of adherens (E-cadherin, β-catenin) and tight (ZO-1) junction proteins. We found that, as compared to uninfected cells, both β-catenin, E-cadherin and ZO-1 localization appears perturbed for infected mounders with slightly increased intracellular fluorescence intensity as compared to cells from uninfected wells (Fig. S8B). Given that mounders have compromised cell-cell junctions, our results suggest that it is most probably the ability of surrounders to transduce forces through their intact cell-cell junctions which is necessary for infection mound formation.

Computational modeling suggest that cellular stiffness, cell contractility and cell-cell adhesions are critical for mounding

Thus far we have shown experimentally that cellular stiffness, cell-matrix and cell-cell force transduction play key roles in the collective extrusion of *L.m.*-infected cells. To better understand how these mechanical signals contribute to infection mounding and explore the precise mechanism of action, we followed a computational approach. We hypothesized that infection mounding could be driven by: (1) decrease in cell stiffness of infected mounders compared to surrounders due to major cytoskeletal alterations; or (2) a weakening of cell-matrix contractility of infected mounders making it easier for surrounders to squeeze them; or (3) robust cell-cell adhesions especially for surrounders as compared to infected mounders, allowing surrounders to transmit long-range intercellular forces against mounders; or (4) a combination of the above.

The computational model we built retained two important features as an initial approach. First the problem is formulated in 3D and second, for simplicity, bacterial infection is considered fixed (*i.e.* bacteria do not spread or replicate). The model assumes that cells form a monolayer, where each cell has a hexagonal shape with six neighbors and can deform in all the directions of the monolayer (Fig. 5A). For simplicity of computation, cells are divided in three different parts[14]: the contractile, the adhesive and the expanding/protruding domains (Fig. S9A). The cells are assumed to have a passive stiffness representing the stiffness arising from the cytoskeleton, including the intermediate filaments, and an active contractility representing the actomyosin contractile apparatus. The interaction of cells with their matrix is also considered through contact interactions and cell-cell adhesions as a continuous material. The assumed mechanotransduction mechanism is depicted in Fig. 5A. Briefly, if the cell-matrix displacements are large when cells contract, new cell-ECM adhesions will be formed. If cell-matrix displacements are small and if there is tensional asymmetry, new protrusions will form at the edge of the cells experiencing minimum stress, followed by another round of cell contraction. If there is no tensional asymmetry, there will be no protrusion and the given cell will just contract (Fig. 5A). In a stable monolayer at steady state (Fig. 5B), all forces are balanced, and no net cell displacement occurs in each round of the simulation.

Using this model, we examined what would happen to the cell displacements and maximum principal stress (maximum tensile stress) in four different cases assuming that infected cells decrease their passive stiffness and their active contractility, as indicated by our experimental results described above. The four different cases we considered initially were: 1)

all cells are uninfected; 2) seven cells are infected; 3) seven cells are infected and uninfected cells in contact with infected ones create new cell-ECM adhesions; and 4) seven cells are infected but cell-cell adhesions are disrupted so no cell-cell force transmission can occur (unlike the other cases in which there will be tight cell-cell contact and significant cell-cell forces). We found that when all cells are uninfected during the contraction phase cell displacements and principal stresses are symmetrical and cells do not create protrusions, since there is no tensional asymmetry (Fig. 5C-D case 1; see also Fig. S9B). However, in case 2 where seven cells are infected, we observe that the uninfected cells in close proximity develop tensional asymmetry but since they are unable to form new cell-ECM adhesions, healthy uninfected cells get displaced away from the center of the infection focus (Fig. 5C-D case 2). This outward displacement of surrounding cells is the opposite of our observed experimental result. In marked contrast, if we allow uninfected cells to form new cell-ECM adhesions during the protrusion phase (Fig. 5C-D case 3), we find that uninfected cells in close proximity to infected cells develop tensional asymmetry and are displaced towards the infection focus (Fig. C-D case 3), forming mounding. Finally, when cell-cell adhesions are absent (case 4) there is no tensional asymmetry and therefore no protrusion formation (Fig. 5C-D case 4). These last two behaviors are consistent what we observe *in vitro* during infection when cells are able to adhere to each other (case 3) or when adherens junctions are compromised (case 4).

Using our model, we can also examine the cell displacements in the vertical direction (z-axis) during *in silico* infection and assess which conditions would give rise to infection mounding. As depicted in Fig. 5E that shows the vertical displacements of cells in monolayers where seven cells are infected (marked with an asterisk) the scenario that gives rise to significant initial infection mounding (*i.e.* squeezing of infected cells in the x- and y-axis and an increase in their height in the z-axis) is case 3. This study reinforces the idea that surrounders need to form protrusions towards the infection focus and subsequently new active cell-ECM adhesions are created in order for infection mounding to happen. The orientation and stresses generated by formation of these new adhesions in the *in silico* model are consistent with what we had previously observed by TFM (Fig. 3C-D, Fig. 4E).

Finally, we examined what would happen if only one of the various mechanical cellular parameters were altered during infection, specifically the passive cellular stiffness, or the active cellular contractility, with and without the presence of cell-cell adhesions. If only the active contractility of infected cells decreases to levels lower of those of uninfected surrounder cells, that is sufficient to elicit infection mounding (Fig. 5F and S9C). Similarly, if the passive stiffness

only of infected cells decreases to levels lower than those of uninfected cells, that is also sufficient to elicit infection mounding, although to a lesser extent (Fig. 5F and S9C). Importantly, if passive stiffness of infected cells decreases as compared to uninfected cells but cell-cell adhesions are disrupted, mound formation is abolished completely (Fig. 5F and S9C). Altogether, these results indicate that, for infection mounding to occur, infected cells have to either decrease their passive stiffness or active contractility, and surrounding uninfected cells need to be able to protrude and form new active cell-ECM adhesions. In addition, cell-cell adhesions are critical since lack of those stalls infection mounding (Fig. 5E-F).

RNA sequencing reveals distinct transcriptional profiles between mounders, surrounders and uninfected cells

To understand what signaling processes might regulate the mechanical and cytoskeletal changes associated with infection mound formation and to understand how those differ in the two battling populations (surrounders versus infected mounders), we followed a transcriptomics approach. To that end, we infected cells for 24 h with *L.m.* and then used flow cytometry to sort the cells in two groups infected (mounders) and uninfected (surrounders), and extracted their RNA. In parallel, we also extracted the RNA from completely uninfected cells (uninfected) seeded in a separate well at same density (Fig. 6A). We then performed RNA sequencing on these three populations. As shown by the volcano plots, all groups show significant numbers of differentially expressed genes when compared to each other (Fig. 6B). The biggest differences in differentially expressed genes (DEGs) are observed between uninfected cells versus mounders or surrounder cells, but there are also a considerable number of genes upregulated or downregulated when comparing surrounders to mounders (Table S1). Consistent with the results shown in the volcano plots, when we perform principal components analysis (PCA) on our samples (N = 4 replicates per condition), we indeed observe three distinct clusters in the PCA space (Fig. 6C). PC1 separates cells based on the well they originate from (*i.e.* exposed or not exposed to bacteria) whereas PC3 separates cells on the presence of or absence of intracellular bacteria.

We then performed pathway enrichment analysis for the DEGs we identified, which revealed multiple pathways significantly perturbed when comparing the different groups (Fig. 6D; Figure S10; Table S2). Compared to cells not exposed to infection, infected mounders showed significant downregulation in 31 genes related to tight junctions and ZO-1 is one of the key genes downregulated. To a lesser degree, pathways related to adherens junctions, focal

adhesions and regulation of the actin cytoskeleton were also downregulated. Surrounders showed significant downregulation of genes related to endocytosis, the actin cytoskeleton, adherens junctions and to a lesser degree focal adhesions and tight junctions. We also found that a lot of genes previously associated with the EMT were up- or down-regulated for the two populations originating from an infected well as compared to uninfected cells that had never been exposed to bacteria. EMT-associated genes that were significantly upregulated included VIM, SNAI1, SNAI2 while genes that were significantly downregulated include ZO-1 and E-cadherin (Table S1). Finally, a lot of genes associated with the Rho-family of GTPases crucial for the regulation of the actin cytoskeleton and actomyosin contractility, as well as integrin-related genes, were differentially regulated both for mounders and surrounders as compared to uninfected cells (Table S1). Altogether these results hint at significant infection-related changes in gene expression for regulators of the cytoskeleton, cell-cell and cell-matrix adhesion elements and EMT-associated transcription factors.

Surprisingly, mounders showed upregulation in genes associated with DNA replication and ferroptosis, and both mounders and to a lesser degree surrounders showed upregulation of cell cycle-related and apoptosis pathways. We hypothesized that these findings are most probably hinting at some kind of stress response or death-related process that infected cells are undergoing which might be linked to the mounding phenotype. To test this hypothesis, we first measured the number of cells collectively on uninfected and on infected wells at different MOIs at 24 h pI. We found no significant differences in the number of cells between conditions suggesting that hyperproliferation in infection is probably not occurring (Fig. S11A). We then performed the BrdU assay that is commonly used for assaying proliferation but also apoptosis. Only 1% of cells from uninfected wells were BrdU-positive, as compared to 0.5% of surrounders and 8% of mounders (Fig. S11B). Interestingly, the mounders that appeared BrdU-positive coincided with the infected cells having the most *L.m.* fluorescence (Fig. S11C), suggesting that most probably BrdU staining captures apoptosis rather than proliferation. We also performed the TUNEL assay to assess DNA fragmentation in cells from uninfected and *L.m.*-infected wells, and found that the latter to exhibit 2-fold increase in TUNEL-positive cells (Fig. S11D). Finally, we used a live-dead stain to identify dead cells after infection and confirmed through microscopy that a number of the extruded cells in the infection mounds do retain the stain (Suppl Fig. 11E). Overall these findings suggest that cells within in the mounds are undergoing cell death, reinforcing the idea that infection mounding is a process which is beneficial for the host since infected cells are being cleared out of the monolayer. It also raises the question of whether the

infected cells undergo death and are therefore extruded or alternatively if the extrusion of cells from the substrate leads to their subsequent death.

Most importantly, surrounders and to a lesser degree infected mounders showed upregulation of genes associated with the IL-17, NF-κB and TNF signaling pathways, which indicates that, although surrounder cells are not themselves infected with bacteria, their distinct mechanical behavior might arise from cytokines released in infection which influence their phenotype, including their gene expression as well as their mechanical behavior. Indeed, when we performed a multiplex immunoassay on the supernatant of cells that were infected for 4 h or 24 h compared to uninfected cells' supernatant, we found several cytokines enriched for cells infected for 24 h as compared to uninfected cells or cells infected for 4 h (Fig. 6E). Out of the 12 cytokines we tested we detected no or very low signal for 9 cytokines, namely: IFN-γ, IL-2, IL-6, IL-7, IL-15, IP-10, IL-10, IL-18, TNF-α. However, compared to uninfected cells, we found that GM-CSF (granulocyte-macrophage colony-stimulating factor, cytokine) was enriched 25-fold, IL-8 (chemokine) was enriched 39-fold and MCP-1 (monocyte chemoattractant protein 1, chemokine) was enriched 520-fold at 24 h pI (Fig. 6E). Interestingly, gene expression of CSF1 (gene encoding GM-CSF) and of CCL2 (gene encoding MCP-1) were significantly upregulated-fold at 24 h post-infection to a greater extent for surrounders as compared to infected mounders (Figure 6G and Table S1). Finally, it is of great interest that all three identified cytokines have been implicated in the past with NF-κB signaling, as being NF-κB activators[15, 16] or as being expressed and secreted in response to NF-κB activation[17-20] or both[21-23]. Intriguingly, MCP-1 has also been implicated in the past in the epithelial to mesenchymal transition of breast cancer cells that adopt a polarized fibroblast-like shape upon exposure to this cytokine[24].

To assess whether cytokine signaling alone, without cells being infected, can induce the polarization and nematic ordering we observed in surrounder cells, we seeded MDCK cells on transwell inserts and infected them or not with *L.m.*. We then placed underneath the inserts cells seeded as monolayers on coverslips so that they would share the same supernatant as the infected cells just above them. When we examined the morphology of MDCK cells on the coverslips 24 h after continuous exposure to supernatant originating from *L.m.*-infected cells, we indeed found significant differences as compared to control cells (Fig. S12). Cells exposed to infected cell supernatant as compared to control cells had increased aspect ratio and area, and appeared also more tortuous in their shape. This result suggests that part of the response and collective behavioral change of the surrounder cells originates due to paracrine signaling.

Inhibition of apoptosis does not attenuate mounding, but perturbations in NF-κB signaling do

Given the evidence that infected mounder cells are undergoing some form of cell death, we sought to understand whether inhibition of cell death processes would stall mound formation. That is, infected cells undergoing some type of cell death associated with disorganization of their cytoskeleton and cell-cell adhesion complexes could be triggering their subsequent extrusion. To test this hypothesis, we treated infected cells at 4 h pI with either the pancaspase inhibitor Z-VAD-FMK or with GSK'872 to inhibit RIPK1 and 3, which are mediators of necroptosis previously associated with *L.m.* infection[25]. To our surprise, infection mounds both of cells treated with Z-VAD-FMK and GSK'872 were actually larger than the corresponding mounds of cell treated with vehicle control (Fig. 7A-B). This result is of major importance because it suggests that cell death occurs after the extrusion of infected cells, not before.

We found that NF-κB and NF-κB-related (*e.g.* IL-17, TNF) pathways are upregulated for cells originating from infected wells and that these cells also secrete cytokines related to NF-κB signaling at later times in infection. To directly examine whether the transcriptional factor NF-κB gets activated late in infection, we performed immunostaining and observed increased nuclear translocation of NF-κB for cells originating from infected wells but not for uninfected cells or infected cells treated with the NEMO binding peptide that inhibits NF-κB activation (Fig. S13A-B). We then treated cells with a variety of inhibitors that directly or indirectly inhibit the NF-κB pathway. More specifically, we treated *L.m.*-infected cells with the NF-κB essential modulator (NEMO) binding peptide that blocks the interaction of NEMO protein with IκB[26] therefore inhibiting NF-κB activation, and found a 25% reduction in infection mound size compared to infected cells treated with vehicle control (Fig. 7C-D). Since NF-κB activation has been shown to lead to increased iNOS levels and production of nitric oxide[27], we also treated cells with the L-NIL inhibitor of iNOS and found a similar reduction in mound size (Fig. 7C-D). Finally given that mTOR has been shown to activate NF-κB[28] and cytokine signaling[29], we treated cells with the mTOR inhibitor rapamycin and found a similar decrease of 31% in infection mound size compared to cells treated with vehicle control (Fig. 7C-D). Treatment of infected cells with the NEMO-binding peptide also suppressed the loss of vimentin from the cells in the mound, to a comparable extent as the loss of cell-cell junctions (Fig. S13). This is consistent with the hypothesis that the cytoskeletal changes associated with the decrease in passive stiffness of the infected cells may be downstream consequences of NF-κB activation. Overall, these results suggest that innate immune signaling through NF-κB plays a role in promoting infection mound

formation in both the infected mounder cells and in the uninfected surrounders, contributing to the loss of mechanical stiffness in the infected cells and triggering cell shape changes and active motility responses similar to the EMT in the uninfected cells immediately surrounding the infection focus.

If our conclusion that NF-κB activation contributes to mound formation is correct, then we hypothesized that we would also observe infection mounding at late times post-infection if we were to infect epithelial host cells with a different intracellular bacterial pathogen that activates NF-κB. To assess this possiblity, we infected MDCK epithelial cells with *Rickettsia parkeri*, an intracellular pathogen unrelated to *L.m.* that is also able to use actin-based motility to drive intercellular spread in epithelial cells[1]. We tested two different bacterial strains, WT *R.p.* and the *OmpB*$^{-}$ *R.p.* mutant that was recently shown to get ubiquitinylated upon entry within host cells[30] and therefore activates host NF-κB, unlike the WT *R.p.* strain (Fig. S14A-B). Consistent with our prediction, we found that *OmpB*$^{-}$ *R.p.*-infected MDCK cells form infection mounds at 96 h pI but WT *R.p.*-infected MDCK cells do not form mounds at all (Fig. 7E-F). Similar to *L.m.*-infected MDCK cells inspected at 24 h pI, we found that tight junction protein ZO-1 localization was significantly perturbed for mounders in *OmpB*$^{-}$ *R.p.*-infected MDCK cells at 96 h pI (Fig. S13C). In marked contrast, both ZO-1 localization and the organization of host cell nuclei around infection foci of WT *R.p.*-infected MDCK resembled those of uninfected cells (Fig. S14C). Altogether these results support the idea that NF-κB signaling is key to eliciting the mechanical competition between mounders and surrounders that leads to mounding and clearance of infected cells.

DISCUSSION

Mechanical forces indirectly or directly drive the remodeling of tissues during morphogenesis and are crucial in regulating homeostatic mechanisms such as cell growth, proliferation and death[31]. In the context of the epithelium these forces can promote celll extrusion which is key in preventing accumulation of excess, aberrant or unfit cells, that eventually undergo death[32]. However, in the context of tumorigenesis, oncogene expression can also drive massive cell extrusion with the exception that extruded cells can remain proliferative with metastatic potential[31]. We find that infected epithelial cells get collectively extruded at late times pI and that these cells are positive for markers of cell death. Blocking death processes 4 h pI by means of pharmacological inhibitors does not attenuate infection mounding. Instead, infection mounds become bigger since extruded cells pile up more. This finding suggests that infection mounding is non-apoptosis dependent and that extrusion of infected cells does not occur due to cells undergoing death but due to increased sensitivity to mechanical stress leading to their compaction and extrusion. It also reinforces the idea that infection mounding is a beneficial for the host mechanism by eliminating infected cells out of the epithelial monolayer since these cells (1) eventually undergo death and (2) the bacteria they contain are unable to spread to neighboring cells therefore limiting infection spread in the basal monolayer. Consistent with these arguments, is our finding that there are no marks of increased cell proliferation for cells originating from infected wells as compared to uninfected wells that would otherwise support the possibility of infection metastasis.

We find that uninfected surrounders which are strongly adherent to their matrix and stiff, mechanically compete with L.m.-infected mounders that are weakly adherent and soft, a process that leads to the eventual extrusion and elimination of the latter population. Competition between two cell populations where one loses and gets eliminated and the other wins and eventually gets expanded, have been studied extensively in recent years and multiple theories and pathways have been implicated[33]. Processes involved in leading to looser cells' elimination can occur due to competition for limiting extracellular pro-survival factors such as in the case of the *Drosophila* wing where cell death or proliferation depends on the presence of soluble factors and the potential of cells to express the dMyc gene[34]. Communication through direct cell-cell contacts can also lead to elimination of looser cells, as when normal MDCK are mixed with cells expressing a constitutive active form of CDC42, which leads to enhanced EGF-MEK-ERK signaling and subsequent E-cadherin cleavage which promotes extrusion[31]. Consistent, with our findings that abolishment of adherens junctions completely blocks infection mounding, previous

studies have shown that E-cadherin-mediated adhesion is critical for apoptotic and non-apoptotic extrusion[35, 36] as are other members of adherens junctions, such as catenins[37]. Cell extrusion of looser cells can also be driven by differential sensitivity to mechanical stress. MDCK cells silenced for the polarity gene, scribble, which renders them hypersensitive to compaction get eliminated when they interact with wild-type cells in crowded conditions[38]. Signaling pathways suggested to be involved in mechanical cellular hypersensitivity include ROCK-mediated contractility[35] and myosin II activity[39], mTOR-p70S6K signaling, abundant winner cell vimentin and filamin expression[40, 41], the HIPPO pathway and compaction driven EGF-MEK-ERK signaling[39, 42]. However how exactly signaling is linked to cytoskeletal and mechanical changes in competing cells and which factors cause mounding as opposed to resulting from mounding is still unclear and potentially multi-factorial. In the context of L.m.-infection, we have evidence that innate immune signaling via cytokine secretion is sufficient to drive differential NF-κB activation which subsequently leads to differential changes in gene expression, cytoskeletal architecture and most importantly cell-cell adhesion organization between mounders and surrounders. Concurrent to these signaling events, mechanical resulting changes are sufficient to drive infection mounding. Although NF-κB inhibition attenuates mound formation infection mounds are still present making it plausible that additional signaling events (*e.g.* EGF-MEK-ERK) might play a role in the infection mound formation.

The nuclear factor-κB (NF-κB) family of transcription factors is key in the host response to infection by bacterial and viral pathogens in that it orchestrates the innate host immune response[43]. In mammals it consists of 5 proteins some of whose expression we find to be significantly upregulated in infection with L.m. (namely RelB, NF-κB1, NF-κB2) which associate with each other to form distinct transcriptionally active homo/heterodimer complexes that migrate to the nucleus. In normal cells at rest, NF-κB is inactive and retained in the cytoplasm. However, during infection proinflammatory cytokines and pathogen-associate molecular patterns activate cell surface receptors including immune receptors (e.g. TLRs), cytokine receptors (*e.g.* TNFRs) and growth factors (EGFRs)[44]. That leads to transferring of signals across the cell membrane to cause activation of the IKK complex that enables release of the NF-κB dimers, translocation to the nucleus and activation of downstream gene transcription. In turn, activation of NF-κB can induce the expression of genes encoding cytokines, chemokines and adhesion molecules (*e.g.* ICAM1, all of which we observe in infection of cells with L.m..

The importance of members of the NF-κB family in the immune response against pathogens has been widely studied for certain bacteria and viruses[43]. There are also pathogens

that have developed complex strategies of suppressing NF-κB activation to dampen the host immune responses or to maintain latency[45]. For instance, the Epstein–Barr virus activates NF-κB during latency, whereas suppresses it during the lytic cycle. Bacteria also modulate NF-κB signaling by either activation or inhibition, according to their own life cycle requirements to favor pathogen survival and spread. Pathogenic *Yersinia* spp. express the Yops Type III effector proteins ultimately inhibiting NF-κB signaling to block production of pro-inflammatory cytokines[46]. Similarly, *Shigella flexneri* T3SS effector OspG can modulate the host NF- κB function by blocking the degradation of IKK, thus blocking NF-κB activation, in response to TNFα stimulation[43]. Interestingly, a recent study showed that macrophages exposed to non-pathogenic *Rickettsia montanensis* secrete significantly more TNFα and express more NFKBIA (NF-κB inhibitor) compared to those exposed to pathogenic *Rickettsia conorii* (that cause life-threatening Mediterranean spotted fever)[47]. It appears as if the pathogenic *Rickettsia conorii* can evade immune signals by modulating the expression of several anti-inflammatory molecules including dampening the activation of NF-κB. Interestingly, we found that *OmpB*$^-$ R.p. infected MDCK but not wild-type RP infected ones, form infection mounds at 96 h pI similar to L.m.-infected MDCK at 24 h pI. In addition, we find that similar to L.m.-infected MDCK, *OmpB*$^-$ but not WT R.p. infected cells show NF-κB activation at these late times pI. OmpB outer membrane protein blocks poly-ubiquitylation of the bacterial surface proteins but is dispensable for cell growth in endothelial cells but not in macrophages[30]. Given previous studies, it appears that there is a link between poly-ubiquitinylation and NF-κB activation[48-50]. 90 % of *OmpB*$^-$ R.p. were positive for M1, K63 or K48-linked ubiquitin chains[30] and interestingly M1 and K63 are ubiquitin chains are also known to activate NF-κB[48-50]. Taken together, it is possible that unlike L.m., WT R.p. might have developed this strategy through expression of OmpB to block poly-ubiquitinylation and NF-kB activation, in order to avoid the formation of infection mounds and therefore continue spreading in the epithelial monolayers at late times pI. L.m. infection of certain cell types also leads to secretion of multiple host cell cytokines and NF-κB activation[43], although the specific trigger(s) from the bacterial side are still debatable with some dampening (*e.g.* InlC)[51] and others activating NF-κB (*e.g.* InlB, LLO)[52]. Recently, the Listeria Adhesion Protein (LAP) expressed by L.m. was shown to both promote adhesion of L.m. onto epithelial cells but also to activate NF-κB. NF-κB activation was shown to in turn upregulate TNF-α and IL-6, increasing epithelial permeability via cellular redistribution of host cell adhesion proteins[53]. These results are consistent with our findings that during late infection cells from infected wells show NF-κB signaling upregulation which is accompanied by dramatic change in cytoskeletal

and cell-cell adhesion organization. These changes enable the surrounders to become more motile and fluidized and to contribute to the extrusion of the infected cells.

Infection mounding is caspase independent, non-cell-autonomous (paracrine signaling, action upon a cell that depends on another cell is involved) and mechanically driven with cell-cell force transduction being necessary and cell-matrix force transduction contributing to infection mounding. Mechanisms describing infected or apoptotic cell extrusion have been previously described on the level mostly of single cell extrusion. The mechanical forces proposed to contribute to this phenomenon have been (1) in low density cell monolayers lamellipodial protrusions of surrounders are thought to drive extrusion whereas in (2) high density cells an actomyosin ring formed around the extruded cell is thought to be the driving force[6, 7]. In this study, we are not looking at the extrusion of a single cell but rather of a collective of cells. We find that both protrusions and active contractility of surrounders around the infection mounds along with long range transmission of forces through cell-cell junctional complexes for the surrounders appear sufficient for squeezing the soft, weakly adhering mounders together and for promoting their cell extrusion in mass. Thus the transmission of forces between cells by cadherin-based adherens junctions, which couple the force-generating actomyosin cytoskeletons of neighboring surrounder cells appears critical for mounding[54].

In the past it has been suggested that in the intestinal epithelium proliferating stem cells at the crypts of the intestine drive the motion of cells upwards with occasionally extruding extruding at the apex of the villi giving the opportunity for L.m. to access E-cadherin receptors and infect epithelial cells or extrude single infected cells[5, 55]. The idea that single infected cells get extruded from a cellular monolayer contributing either to infection clearance (beneficial for the host) or to bacterial dissemination (beneficial for the pathogen) has been previously suggested for infections including *Salmonella enterica* and L.m. [56, 57]. However, they precise biochemical mechanism is unclear, and we know even less did we know about the mechanics of such process.

We found that at late times post-infection mechanically-driven cellular competition promotes the collective extrusion of L.m.-infected epithelial cells. Intercellular forces are key in the formation of the mounds that arise from competition of surrounders with mounders which show differing levels of cellular contractility and stiffness. Innate immunity signals and in particular NF-kB activation promotes this mechanical cell competition which we provide evidence to generalizable and applicable in further bacterial infections that involve activation of

NF-κB. And what do we think is the biological significance of our findings and why this process represents of novel paradigm of hosts limiting infection spread? Epithelial monolayers in the intestine and lung are common sites of pathogen attack and therefore a general cooperative epithelial extrusion mechanism, like the one discovered herein, could quickly help to limit the local spread of infection, in the context of the intestine for instance by discarding the infected cells out of the host via the fecal route.

FIGURE LEGENDS

Figure 1. Kinematics of L.m.-infected host epithelial cells change dramatically 24 post-infection.

(**A-B**) Representative orthogonal views of (A) uninfected and (B) L.m. -infected host epithelial MDCK nuclei (nuclei: blue, L.m.: green). Samples were fixed at 24 h post-infection (pI). For (B) a single infection mound is shown. (**C-D**) 2D planar displacements of host nuclei basal layer (*i.e.* of cells attaching to the substratum). Cells were tracked between 24 to 44 h pI. Different colors represent different nuclei tracked which are colorcoded based on time. (**E**) Boxplot of the mean speed of migration of uninfected and L.m.-infected host nuclei. Nuclei where tracked between 24 to 44 h pI. The average speed of migration of all nuclei in a field of view over time was calculated for N=5 experiments. Boxes represent the interquartile range, horizontal bar the mean, whiskers indicate the 5-95% confidence interval and asterisk indicates *p*-value<0.01 (non-parametric Wilcoxon Rank Sum test). (**F-G**) Same as panels C-D but trajectories of host nuclei tracked in all 3 dimensions are shown. (**H-I**) Plots showing the weighted average for each delay of all MSD curves of host cell nuclei in a particular field of view tracked between 24 to 44 h pI. Panel H refers to uninfected host MDCK nuclei and panel I to L.m.-infected MDCK nuclei. The grayed area represents the weighted standard deviation over all MSD curves. The error bars show the standard error of the mean which is approximated as the weighted standard deviation divided by the square root of the number of degrees of freedom in the weighted mean. The red line represents the weighted mean MSD curve from which the diffusion coefficient *D* is calculated. The fit was made in the first 500 min. x and y -axes limits are the same in both panels to allow direct comparison with the exception that in panel B there is z zoomed inlet provided. **(J-K**) Boxplots of the average diffusion coefficient *D* (J) and of the average α (K) for uninfected or L.m.-infected MCDK cells (N=5 experiments). Asterisk indicates *p*-value<0.01 (non-parametric Wilcoxon Rank Sum test).

Figure 2. L.m.-infected cells get squeezed and surrounding uninfected cells become polarized and orient perpendicularly to the tangent of the infection focus

(A) Changes in cell area and orientation for uninfected MDCK cells (upper row) or L.m.-infected cells at 24 h pI (bottom row). Representative brightfield image (1st column), corresponding L.m. bacterial fluorescence (2nd column), segmented cells colorcoded based on their area (3rd column) and segmented cells colorcoded based on their orientation (5th column). Orientation is defined as the angle between the radial direction and the direction of the major axis of the cell. If the orientation is close to zero, cells are oriented radially towards the center of the image. If the

orientation is close to 90º the orientation is circumferential. Purple circle indicates the infection mound. 4th column indicates a zoomed version of the area of cells. (**B**) Boxplot of the average cell area (μm^2) for uninfected cells (brown, N=4211), surrounders (green, N=4285) and mounders (pink, N=949). Asterisk indicates *p*-value<0.01 (non-parametric Wilcoxon Rank Sum test). (**C**) Mean radial orientation for uninfected and L.m.-infected cells shown in panel A. Blue crosses show individual orientation values of cells along the radial direction and red crosses show the mean average cell orientation from the center of the focus outwards (x-axis). **(D)** Representative orthogonal views of uninfected epithelial MDCK nuclei (1st column) and L.m.-infected MDCK (3rd column) and corresponding F-actin organization (2nd and 4th column, upper row) and vimentin localization (2nd and 4th column, bottom row).

Figure 3. Competition between mounders and surrounders is mechanically-driven.

(A) Phase contrast image of host MDCK cells (left) and corresponding L.m. fluorescence image (right) for cells that are 20% infected at 24 h pI. Mound formation can be observed at the phase image due to infected mounders competing with uninfected surrounders. **(B)** Same as panel A but for cells that are 100% infected. Lack of cellular competition results in lack of infection mounding. **(C)** Representative phase contrast images (phase, 1st column), L.m. fluorescence images (L.m., 2nd column), cell-matrix deformation maps (2rd column, color indicates deformation magnitude in μm), radial deformation, u_r maps (4th column, positive deformations values in μm indicate deformations pointing away from the center of the focus, outwards), overlap of u_r maps and L.m. fluorescence (5th column) and traction stresses (6th column, color indicates stress magnitude in Pa) exerted by confluent MDCK host cells adherent onto soft 3 kPa hydrogels and infected with low dosage of L.m.. Rows refer to different time points pI indicated. (**D**) Kymograph of the mean radial deformation u_r (in μm) as a function of time, t (left image). The center of the polar coordinate system is considered at the center of the infection focus. Kymograph of the mean radial L.m. fluorescence intensity as a function of time, t (middle image). Overlap of kymographs of both previous kymographs (right image). **(E)** Boxplots of the cellular stiffness (Young's Modulus, kPa) of uninfected cells originating from uninfected wells (brown, N=68), surrounders (green, N=126) and infected mounders (pink, N=130). Cells were indented using a 5 μm diameter spherical tip at 24 h pI. P value<0.01 is indicated with an asterisk (non-parametric Wilcoxon Rank Sum test).

Figure 4. Lack of cell-cell adhesions stall infection mounding while actomyosin contractility inhibition attenuates it

(A) Boxplots showing relative infection mound size at 24 h pI for cells treated with vehicle control or 30 μM of Y27632 ROCK inhibitor or 50 μM of Myosin II inhibitor blebbistatin. Cells were infected with low dosage of L.m. and treated with inhibitors at 4 h post-infection. Mound size was assessed based on the fluorescence of host cell nuclei along multiple z-stacks spanning the entire mound. P value<0.01 is indicated with an asterisk (non-parametric Wilcoxon Rank Sum test). **(B)** Representative orthogonal views of MDCK nuclei (blue) infected with L.m. (white) and treated with vehicle control (left image) or 30 μM of Y27632 (right image). Samples were fixed at 24 h post-infection (pI). **(C)** Boxplots showing relative infection mound size at 24 h pI for WT MDCK cells, αE-catenin knockout MDCK cells and cells treated with siRNA against E-cadherin (siCDH1). P value<0.01 is indicated with an asterisk (non-parametric Wilcoxon Rank Sum test). **(D)** Representative orthogonal views of WT MDCK nuclei (blue) infected with L.m. (white) (left image) and αE-catenin knockout MDCK nuclei infected with L.m. (right image) at 24 h pI. **(E)** Representative phase contrast images (phase, 1st column), L.m. fluorescence images (L.m., 2nd column), cell-matrix deformation maps (2rd column, color indicates deformation magnitude in μm), radial deformation, u_r maps (4th column, positive deformations values in μm indicate deformations pointing away from the center of the focus, outwards), overlap of u_r maps and L.m. fluorescence (5th column) and traction stresses (6th column, color indicates stress magnitude in Pa) exerted by confluent of αE-catenin knockout MDCK host cells adherent onto soft 3 kPa hydrogels and infected with low dosage of L.m.. Rows refer to different time points pI indicated.

Figure 5. Computational modeling hints on cellular stiffness, cell contractility and cell-cell adhesions being critical for mounding.

(A) Schematic showing details of the computational model. Diagram on the left depicts the mechanotransduction mechanism assumed. Schematic on the right illustrates the whole model and indicates the position of two cells that are analyzed below. Infected cells are marked with an asterisk. Underneath of the whole model, sketch shows the two main types of cell-ECM adhesions. The one in red is always present and the yellow only appears in certain cases. (**B**) Simulation results showing the cell displacements (colorbar shows displacement magnitude in μm and arrows depict displacement direction) during the contraction phase for four different cases assuming that infection leads to softening of infected cells: (1) all cells are healthy, (2) seven cells are infected and uninfected neighboring cells in contact with infected cells cannot create new cell-ECM adhesions, (3) seven cells infected and uninfected neighboring in contact with infected cells create new cell-ECM adhesions and 4) seven cells are infected but all cell-

cell adhesions of both infected and uninfected cells are disrupted. (**C**) Same as panel B but showing cell displacements during cell protrusion phase for the four different cases we considered above. **(D)** Plots showing the cell displacements in the vertical (z) direction for the whole model in two different views. Same four cases as in panel B. Asterisks denote infected cells.

Figure 6. RNA sequencing reveals distinct transcriptional profiles displayed by mounders, surrounders and uninfected cells

(A) Sketch showing the 3 different populations that were used for RNA-sequencing (4 replicates) namely: uninfected cells from uninfected well (uninfected, brown), infected cells from infected well (infected mounders, pink) and uninfected cells from infected well (surrounders, green). (**B-D**) Volcano plots showing differentially expressed genes (DEGs) between all three groups. The $-\log_{10}$ p-values (y-axis) are plotted against the average $\log_2$ fold changes in expression (x-axis). Non DEGs are plotted in light gray. For each pair of conditions compared upregulated genes of each group are shown in the corresponding color. Number of genes that do not change or are differentially regulated are also shown. (B) Uninfected cells versus infected mounders, (C) uninfected cells versus surrounders and (D) surrounders versus infected mounders. **(E)** Principal component analysis (PCA) on top genes that have the ANOVA p value ≤ 0.05 on FPKM abundance estimations. PC1 is plotted versus PC3. Surrounders shown in green, infected mounders in pink and uninfected cells in brown. Dashed lines indicate separation based on PC1 on whether cells come from infected or uninfected well and on PC3 based on whether cells are carrying bacteria. **(F)** Pathway enrichment analysis based on the KEGG database on the DEGs identified. Infected mounders (pink) or surrounders (green) are compared to uninfected cells based on their enrichment score ($-\log_{10}p$). P-values were calculated by Fisher's exact test were used to estimate the statistical significance of the enrichment of the pathways between the groups compared. **(F)** Boxplots showing concentration (pg/mL) of cytokines in the supernatant of cells for cells originating from uninfected well or for cells at 4h pI or 24 h pI. Only cytokines whose expression was >1 pg/mL are displayed. P value<0.01 is indicated with an asterisk (non-parametric Wilcoxon Rank Sum test). **(G)** Boxplots showing gene expression at 24 h pI of infected mounders (pink) versus uninfected surrounders (green) as compared to non-infected cells for cytokines CSF2, CXCL8 and CCL2. P value<0.01 when comparing relative gene expression of surrounders versus infected mounders is indicated with an asterisk (non-parametric Wilcoxon Rank Sum test).

Figure 7. Inhibition of NF-κB activation but not of apoptosis attenuates mounding

(A) Boxplots showing relative infection mound size at 24 h pI for WT MDCK cells, cells treated with 5 μM GSK'872 to inhibit RIPK1 and 3 and 100 μM Z-VAD-FMK to inhibit caspases. P value<0.01 is indicated with an asterisk (non-parametric Wilcoxon Rank Sum test). **(B)** Representative orthogonal views of MDCK nuclei (blue) infected with L.m. (white) and treated with vehicle control (left image), or 5 μM GSK'872 (middle image), or 100 μM Z-VAD-FMK (right image). **(C)** Boxplots showing relative infection mound size at 24 h pI for WT MDCK cells, cells treated with 50 μM of NEMO binding peptide to inhibit NF-κB, or 5 μM LNIL to inhibit iNOS, or 1 μM Rapamycin to inhibit mTOR. **(D)** Representative orthogonal views of MDCK nuclei (blue) infected with L.m. (white) and treated with vehicle control (1st image), or 50 μM of NEMO (2nd image), or 5 μM LNIL (3rd image), or 1 μM Rapamycin (4th image). **(E)** Boxplots showing relative infection mound size at 24 h pI for MDCK cells infected with WT R.p. and with *OmpB*$^{-}$ R.p as compared to L.m. infected mounds of MDCK cells. **(F)** Representative orthogonal views of uninfected MDCK nuclei (blue) (right image), or MDCK infected with WT R.p. (middle image), or MDCK infected with *OmpB*$^{-}$ R.p. (right image). P value<0.01 is indicated with an asterisk (non-parametric Wilcoxon Rank Sum test).

SUPPLEMENTAL FIGURE LEGENDS

Supplemental Figure 1. Human epithelial A431D cells infected with L.m. also form infection mounds at 24 h pI, Related to Figure 1

(**A**) Boxplot of the track straightness (track displacement divided by track length) of uninfected and L.m.-infected host nuclei. Nuclei where tracked between 24 to 44 h pI. The average track straightness of all nuclei in a field of view over time was calculated for N=5 experiments. P value<0.01 is indicated with an asterisk (non-parametric Wilcoxon Rank Sum test).
(B-C) Representative orthogonal views of (B) uninfected and (C) L.m.-infected host A431D epithelial nuclei (nuclei: blue, *Listeria*: white). Samples were fixed at 24 h pI and in panel B a single infection focus is shown. (**D**) Sketch showing mean square displacement (MSD) versus time delay (τ) relationship for different types of motion. *D* is the diffusion coefficient. For normal diffusion the scaling is linear (purple), α = 1 while anomalous diffusion shows a power law behavior, with α > 1 termed superdiffusion (green) and α < 1 called subdiffusion (red).

Supplemental Figure 2. Cell shape and collective behavior changes in mounders versus surrounders, Related to Figure 2

(A) Representative images of uninfected MDCK (upper row) or L.m.-infected MDCK at 24 h pI, referring to Fig. 2A. 1st column shows E-cadherin localization used for cell segmentation shown in 2nd column. 3rd and 4th columns show cells colorcoded based on their aspect ratio (*AR,* major axis/minor axis) and on the shape factor *q* (perimeter/ $cell\ petimeter/\sqrt{area}$) respectively. **(B)** Schematic showing how orientation is defined as the angle θ between the radial direction and the direction of the major axis of the cell. If the orientation is close to zero, cells are oriented radially towards the center of the infection focus. If the orientation is close to 90º the orientation is circumferential. **(C)** Histogram of the average number of neighbors of a particular cell that have a similar orientation of the major axis ($\Delta\theta$=+/-10°C). The 100 closest cells based on the nearest neighbor distance of each cell were considered. Blue and red histograms correspond to fields of view comping from uninfected and infected wells respectively. (**D-E**) Boxplots of the average aspect ratio *AR* (B) and of the shape factor *q* (C) for uninfected cells (brown, N=4211), surrounders (green, N=4285) and infected mounders (pink, N=949). P<0.01 is indicated with an asterisk (non-parametric Wilcoxon Rank Sum test). **(F)** Scatter plots of the aspect ratio *AR* versus the shape factor *q*, for uninfected cells (dark brown) versus surrounders (green) (left) and versus mounders (right) (F). For each populations the best line fit is provided with the appropriate color.

Supplemental Figure 3. Changes in the host cell cytoskeleton for mounders as compared to surrounders, Related to Figure 2

(A) Representative orthogonal views of uninfected epithelial MDCK nuclei (left) and L.m.-infected MDCK cells (right) at 24 h pI. The image of the host nuclei (blue) is superimposed to the image of L.m. (white) for the infected setting and on the first row the corresponding localization of tubulin is shown while on the second row cells are stained for cytokeratin. **(B)** Boxplot of the ratio of mean actin (N=6 mounds), tubulin (N=6 mounds), vimentin (N=11 mounds) and cytokeratin (N=6 mounds) fluorescence intensity per cell of mounders to surrounders.). P<0.01 is indicated with an asterisk (non-parametric Wilcoxon Rank Sum test).

Supplemental Figure 4. Kymographs of mean radial deformation and L.m. fluorescence for MDCK cells infected with L.m., Related to Figure 3

(**A**) Kymographs of the mean radial deformation u_r (μm, right image), of the mean radial L.m. fluorescence intensity (middle image) and of their overlap (right image) as a function of time, t. The center of the polar coordinate system is considered at the center of the infection focus. The kymograph has been split in time segments of approximately 8 h and corresponding time intervals are indicated. **(B)** Mean radial host cell-matrix deformations, u_r (μm) versus distance

from the center of the mound outwards (in μm) is shown in solid lines. Mean radial L.m. fluorescence intensity versus distance from the center of the mound outwards is shown with the dashed lines. Lines are color-coded depending on time pI and shown for every 10 frames (50 min). Different plots show different time segments indicated by the colorbar as infection precedes from 4 h post-infection (top-left) to 62 h post-infection (bottom-right). Panels are chronologically ordered and correspond to the segments of the kymograph shown in panel A.

Supplemental Figure 5. Infection mounds for MDCK cells infected with different *Listeria* mutants, Related to Figure 3

(A) Representative orthogonal views of infected host epithelial MDCK with WT L.m., *ΔinlC* L.m., *ΔinlP* L.m. and LLO^{G486D} L.m. (nuclei: blue, L.m.: white). Samples were fixed at 24 h pI. **(B)** Boxplots showing size of infection mounds relative to MDCK infected with WT L.m.. for infection mounds created by infecting either with *ΔinlC* L.m., or *ΔinlP* L.m., or LLO^{G486D} L.m.. Samples were fixed at 24 h pI and examined through confocal microscopy. **(C)** Boxplots showing the relative bacterial fluorescence with respect to MDCK infected with WT L.m. fluorescence in the infection mounds. Infection mounds were created by infecting either with WT L.m., or *ΔinlC* L.m., or *ΔinlP* L.m., or LLO^{G486D} L.m.. Samples were fixed at 24 h pI and examined through confocal microscopy. L.m. fluorescence was calculated by integrating fluorescence along all 3 dimensions. $P<0.01$ is indicated with an asterisk (non-parametric Wilcoxon Rank Sum test).

Supplemental Figure 6. Reduction in cell stiffness for L.m.-infected MDCK cells, Related to Figure 3

(A) Height maps (1st row), cellular stiffness maps (2nd row) and force-separation plots for uninfected MDCK (left panels) or L.m.-infected MDCK (right panels). Cell stiffness was probed using a conical shape 130 nm-diameter sphere, and force-volume mapping. Data were analyzed using the Sneddon Model on the extend curves. **(B)** Force-separation density plots showing the measurements attained within the white boxes indicated in the cell stiffness maps in panel A. **(C)** Phase images of the uninfected cells (left image) and L.m.-infected cells (middle image) together with the L.m. fluorescence image (right image). These cells were probed with a 5 μm spherical tip and data were analyzed using the Hertz model on the extend curves and are shown in Figure 3E.

Supplemental Figure 7. Cell-cell adhesions are necessary for mounding, Related to Figure 4

(A) Relative with respect to β-actin gene expression of CDH1 obtained by RT-qPCR. The relative levels of expression are shown for cells treated with control siNT and with siCDH1. N=4 replicates are shown for each group treated with either siNT or siCDH1. **(B)** Boxplots showing the convex hull area (μm^2) of the infection foci of WT MDCK or αE-catenin KO MDCK at 24 h pI. **(C)** Boxplots showing the ratio of the integral of L.m. fluorescence intensity to the convex hull area (μm^2) for WT MDCK or αE-catenin KO MDCK infection foci at 24 h pI. **(D)** Phase contrast image (left) of WT MDCK cells infected with L.m. and L.m. fluorescence (right panel) for cells at 24 h pI. A single infection focus is shown. **(E)** Same as panel A but for αE-catenin KO MDCK infected with L.m.. **(F-G)** Representative orthogonal views of the nuclei of A431D cells not expressing E-cadherin mixed with cells expressing full length E-cadherin to a ratio of 100:1 in an uninfected setting (F) or when cells are infected with L.m. (G) at 24 h pI. **(H)** Boxplots showing the convex hull area (μm^2) of the L.m. infection foci of A431D cells expressing full length E-cadherin or A431D cells not expressing E-cadherin mixed with cells expressing full length E-cadherin to a ratio of 100:1. **(I)** Boxplots showing L.m. infection mound volume (μm^3) at 24 h pI for A431D cells expressing full length E-cadherin or A431D cells not expressing E-cadherin mixed with cells expressing full length E-cadherin to a ratio of 100:1. $P<0.01$ is indicated with an asterisk (non-parametric Wilcoxon Rank Sum test). **(J)** Phase contrast image (left) for A431D cells expressing full length E-cadherin and infected with L.m. and L.m. fluorescence (right panel) for cells at 24 h pI. A single infection focus is shown. **(K)** Same as panel H but for A431D not expressing E-cadherin mixed with cells expressing full length E-cadherin to a ratio of 100:1 and infected with L.m. at 24 h pI.

Supplemental Figure 8. Changes in the host cell-cell adhesions' organization for mounders as compared to surrounders, Related to Figure 4

(**A**) Representative orthogonal views of epithelial L.m.-infected MDCK cells (right) at 24 h pI and of E-cadherin fluorescence for host cells expressing 100% WT MDCK expressing Ecadherin-RFP (left two panels) or for 1:1 mixtures of WT MDCK expressing Ecadherin-RFP with αE-catenin KO MDCK. (**B**) Representative orthogonal views of uninfected epithelial MDCK nuclei (left) and L.m.-infected MDCK cells (right) at 24 h pI. The image of the host nuclei (blue) is superimposed to the image of L.m. (white) for the infected setting and on the first row the corresponding localization of E-cadherin is shown, in the 2nd row β-catenin localization and 3rd row ZO-1 localization.

Supplemental Figure 9. Computational modeling hints on cellular stiffness, cell contractility and cell-cell adhesions being critical for mounding, Related to Figure 5

(A) Sketch showing the three different parts in which cells are divided (contraction, adhesion and expansion) and the cell-cell unions. (**B**) Simulation results showing minimum principal stress during contraction in the passive part of the model for four different cases: 1) all cells are healthy, 2) seven cells infected, 3) seven cells infected and healthy cells in contact with infected cells create new cell-ECM adhesions and 4) seven cells infected and all cell-cell adhesions are disrupted. Note the stress asymmetry in cases 2, 3 for the cell closer to the infected cell. **(C)** Plots showing the role of the active and passive part of the cell model in driving infection mound formation and corresponding to Figure 5 E. Note that in case 5 only the active stiffness of infected cells is decreased (*i.e.* the cell contractility) and in case 6 only the passive stiffness of infected cells is decreased (*i.e.* cytoskeletal stiffness).

Supplemental Figure 10. Pathway enrichment analysis for the differentially expressed genes between uninfected cells, mounders and surrounders, Related to Figure 6

(A-C) Pathway analysis mapping genes to KEGG pathways. The dot plot shows the enrichment score values (x-axis) of the top ten most significant enrichment terms indicated in the y-axis. The size of the dots is proportional to the gene counts for each pathway and the dots are color-coded based on their corresponding p-values. Color gradient ranges from red to blue in order of increasing p-value. *I.e.* red indicates low p-values (high enrichment) and blue indicates high p-values (low enrichment). (A) Comparison of uninfected cells versus mounders. Left dot plot shows pathways upregulated for uninfected cells and right plot pathways upregulated for mounders. (B) Comparison of uninfected cells versus surrounders. Left dot plot shows pathways upregulated for uninfected cells and right plot pathways upregulated for surrounders. (A) Comparison of surrounders versus mounders. Left dot plot shows pathways upregulated for surrounders and right plot pathways upregulated for mounders.

Supplemental Figure 11. Cell proliferation and death in infection mounds, Related to Figure 7

(A) Boxplot showing number of cells that pass through the flow cell in 20 s (N=4). Cells originating either from an uninfected well or from L.m.-infected well (MOI=200 or 66.66) were collected in flow tubes at 24 h pI. No significant (ns) differences in the number of cells for the different conditions were detected. $P<0.01$ is indicated with an asterisk (non-parametric Wilcoxon Rank Sum test). **(B)** Boxplots showing ratio of BrdU positive to negative cells for uninfected MDCK (brown), surrounders (green) and L.m.-infected mounders (pink). Cells were stained with BrdU-FITC at 24 h pI. L.m. expressing mtagRFP was used in infection. **(C)** Bivariate density plot of RFP fluorescence (for L.m. containing cells) versus FITC fluorescence

(for BrdU stained cells). Gate separates cells in 4 distinct populations based on whether they are BRdU positive or negative, L.m. positive or negative. Left plot shows control uninfected, unstained cells. Middle plot shows uninfected, BrdU-stained cells. Right plot shows L.m.-infected, BrdU-stained cells. **(D)** Boxplot showing the percentage of TUNEL positive cells coming from uninfected (N=3) or L.m.-infected wells (N=3). Positive and negative controls supplied with the TUNEL kit used are also shown. **(E)** Representative phase contrast images of MDCK infection mounds (1st column), MDCK nuclei (2nd column), L.m. fluorescence image (3rd column), and dead cells stained with live-dead stain (4th column). Each row shows depicts a different representative mounds imaged.

Supplemental Figure 12. Uninfected cells exposed for 24 h to supernatant from L.m.-infected cells display changes in their morphology and increased polarity, Related to Figure 6

(A) Changes in cell shape morphology for cells exposed for 24 h to supernatant originating from L.m.-infected cells. First row refers to control cells and second row to cells exposed for 24 h to supernatant from L.m.-infected cells. Cells were seeded on transwell inserts and infected or not with L.m.. Non-infected cells seeded on coverslips were then places under the transwell inserts to share the same media as cells seeded on the transwell insertss. 24 h pI non-infected cells were fixed, immunostained and inspected via confocal microscopy. Representative image showing E-cadherin localization (1st column), segmented cells colorcoded based on their aspect ratio (2nd column), on their area (3rd column), on their shape factor q (4th column) and on their orientation (5th column). Orientation here is defined as the angle of the major axis of the cells relative to the positive x-axis, so that it ranges from -90º to 90º. **(B-D**) Boxplots of the average aspect ratio (B), cell area (μm^2), and shape factor q for cells not exposed (N=1059 cells) or exposed to supernatant from L.m. infected cells for 24 h (N=924 cells). Asterisk indicates *p*-value<0.01 (non-parametric Wilcoxon Rank Sum test).

Supplemental Figure 13. Vimentin organization in infection mounds for host , Related to Figure 7

(A) Representative orthogonal views of L.m.-infected MDCK cells treated with vehicle control (left) or with 50 μM of the NEMO binding peptide to inhibit NF-κB (right) at 24 h pI. The image of the host nuclei (blue) is superimposed to the image of L.m. (white) for the infected setting and the corresponding localization of vimentin is also shown. **(B)** Representative orthogonal views of uninfected epithelial αE-catenin KO MDCK nuclei (left) and L.m.-infected αE-catenin KO MDCK cells (right) at 24 h pI. The image of the host nuclei (blue) is superimposed to the image of L.m.

(white) for the infected setting and on the first row the corresponding localization of vimentin is also shown. **(C)** Boxplot of the ratio of mean vimentin fluorescence intensity per cell of mounders to surrounders (N=6 mounds) for control WT MDCK cells, αE-catenin KO MDCK cells and WT MDCK cell treated with the 50 μM the NEMO binding peptide to inhibit NF-κB. $P<0.01$ is indicated with an asterisk (non-parametric Wilcoxon Rank Sum test).

Supplemental Figure 14. NF-κB and ZO-1 localization in uninfected settings and during infection with L.m., WT RP and *OmpB*$^-$ RP, Related to Figure 7

(A) Representative confocal images of the maximum intensity projection of Hoechst-stained host MDCK nuclei superimposed to the maximum intensity projection of bacterial fluorescence around infection foci (left) and of NF-κB localization at a plane located at the basal cell monolayer (right). Uninfected MDCK, L.m.-infected MDCK at 24 h pI, WT R.p.-infected MDCK at 96 h pI, and *OmpB*$^-$ R.p.-infected MDCK at 96 h pI are shown. (**B)** Boxplots showing the normalized with respect to uninfected cells ratio of nuclear to cytoplasmic NF-κB for L.m.-infected MDCK treated with vehicle control (24 h pI), L.m.-infected cells treated with 50 μM NEMO binding peptide to inhibit NF-κB activation, WT R.p.-infected MDCK (96 h pI) and *OmpB*$^-$ R.p.-infected MDCK (96 h pI). (**C)** Representative confocal images of the maximum intensity projection of Hoechst-stained host cell nuclei superimposed to the maximum intensity projection of bacterial fluorescence around infection foci (left) and of ZO-1 maximum intensity projection (right). Uninfected MDCK at 72 h post-seeding, L.m.-infected MDCK at 24 h pI, WT R.p.-infected MDCK at 96 h pI, and *OmpB*$^-$ R.p.-infected MDCK at 96 h pI are shown.

SUPPLEMENTAL TABLE LEGENDS

Table S1. Differentially expressed genes between uninfected cells, infected mounders and uninfected surrounders. Table presents the DEGs identified when comparing the transcriptome of uninfected cells (UU) to surrounders (UI) (1st sheet), uninfected cells (UU) to infected mounders (II) (2nd sheet) and uninfected surrounders (UI) to infected mounders (II) (3rd sheet). Rows correspond to the genes identified and columns A-K correspond to different parameters explained within the table. Columns L-S provide the FPMK of genes in samples for each sample from the corresponding groups compared.

Table S2. KEGG pathways are significantly perturbed when comparing uninfected cells, infected mounders and uninfected surrounders. The gage package was used for pathway analysis which has precompiled databases for mapping genes to KEGG pathways so to perform pathway enrichment analysis of DEGs between all three populations. Table shows comparisons

performed between uninfected cells (UU) to surrounders (UI) (1st sheet), uninfected cells (UU) to infected mounders (II) (2nd sheet) and uninfected surrounders (UI) to infected mounders (II) (3rd sheet). KEGG pathways upregulated for each group are indicated. Rows show the KEGG pathways and column different parameters explained in the table including upregulated genes of each category.

SUPPLEMENTAL MOVIE LEGENDS

Movie S1. Time-lapse movie showing orthogonal views of uninfected MDCK epithelial nuclei over the course of 20 h. Orthogonal views of Hoechst-stained MDCK epithelial cell nuclei over the course of 20 h. Acquisition started at 48 h post-seeding and frame rate is 30 min. Time is shown on the lower right corner of the movie and scale bar on the lower left. One image from each different plane (i.e. x-y plane, x-z plane and y-z plane) are shown.

Movie S2. Time-lapse movie showing orthogonal views of L.m.-infected MDCK epithelial nuclei over the course of 20 h. Orthogonal views of Hoechst-stained MDCK epithelial cell nuclei over the course of 20 h. L.m. is shown in green. Acquisition started at 24 h post-infection for cells previously seeded for 24 h. Frame rate is 30 min. Time is shown on the lower right corner of the movie and scale bar on the lower left. One image from each different plane (i.e. x-y plane, x-z plane and y-z plane) are shown.

Movie S3. Traction force microscopy on WT host MDCK cells infected with low dosage of L.m.. Upper left image shows the phase contrast image of host MDCK cells. Scale bar and corresponding time post-infection are also indicated. Upper middle image the corresponding L.m. fluorescence image. The infection focus is centered in the middle of the field of view chosen. Upper right panel shows the cell-matrix deformations that cells are producing onto their matrix (color indicates deformation magnitude in μm). Bottom right image shows the radial deformation, u_r maps (positive deformations values in μm indicate deformations pointing away from the center of the focus, outwards) and bottom middle image the overlap of u_r maps and L.m. fluorescence. Finally bottom right image shows the traction stresses (color indicates stress magnitude in Pa) exerted by MDCK host cells adherent onto the soft 3 kPa hydrogels.

Movie S4. Traction force microscopy on αE-catenin knockout MDCK cells infected with low dosage of L.m.. Same as Movie S5 but for αE-catenin knockout MDCK cells.

Movie S5. Time-lapse movie of 50% αE-catenin knockout MDCK mixed with 50% WT MDCK cells infected with low dosage of L.m.. Time-lapse images show L.m. in green and WT MDCK cells only since they are expressing E-cadherin-RFP over the course of 30 h.

Acquisition started at 4 h post-infection and frame rate is 10 min. Field of view is centered on an infection focus of L.m. shown in green. Notice the formation of an infection mound.

Movie S6. Time-lapse movie of 50% αE-catenin knockout MDCK mixed with 50% WT MDCK cells infected with low dosage of L.m.. Same as Suppl. Movie 5 but infected cells do not form an infection mound.

MATERIALS AND METHODS

Mammalian cell culture conditions

Type II MDCK cells (generous gift from the Bakardjiev lab, University of California, San Francisco) were cultured in high glucose DMEM medium (Thermofisher; 11965092) containing 4.5 g/L glucose and supplemented with 10% fetal bovine serum (GemBio; 900-108) as previously suggested[58]. Passages used were between P10-P40. WT MDCK cells expressing E-cadherin-RFP were a generous gift from the Nelson lab, Stanford University[59]. αE-catenin knockout MDCK cells were also a generous gift from the Nelson lab, Stanford University[58]. A431D human epithelial carcinoma cells a were generous gift from Cara Gottardi, Northwestern University and were grown in DMEM with high glucose (4.5 g/l) in the presence of 10% FBS and 1% penicillin-streptomycin. Transduced cell lines that express full length E-cadherin were cultured in media supplemented with 800 µg/ml geneticin and were generated as described previously[58].

Infection of epithelial cells with L.m.

MDCK or A431D cells seeded on glass or polyacrylamide collagen I-coated substrates were infected as previously described with the following modifications[5, 60]. The day prior to infection, host cells were seeded at a density of $2x10^5$ cells/well for cells residing on wells of 24-well plates and grown for 24 h. L.m. liquid cultures were started from a plate colony, and grown overnight at room temperature in the dark without shaking, in Brain Heart Infusion (BHI) media (BD; 211059) supplemented with 200 µg/mL streptomycin and 7.5 µg/mL chloramphenicol. Flagellated overnight cultures of bacteria (O.D.600 approximately 0.8) were then washed twice by centrifugation at 2000 x g in PBS to remove any soluble factors. Infections were then performed in normal MDCK growth media by adding 1 mL of bacteria to 15 mL of media and then adding 1 mL of the mixture per well. After 30 min of incubation at 37 °C, samples were washed 3 times in PBS and then media was replaced with media supplemented with 20 µg/mL gentamicin. Multiplicity of infection (MOI) was determined by plating bacteria at different dilutions, on BHI agar plates with 200 µg/mL streptomycin and 7.5 µg/mL chloramphenicol and measuring the number of colonies formed two days post-infection. The resulting multiplicity of infection (MOI) was ~200 bacteria/cell. A similar approach was followed when A431D were infected with L.m.. All bacterial strains used in these studied are indicated in Table S1.

Analysis of infection via flow cytometry was performed at 7-8 h after infection, unless otherwise stated. For drug exposure experiments, unless otherwise indicated, media was removed from the cells and replaced with media containing either the drug or vehicle control 1 h post-infection.

Flow cytometry of MDCK cells infected with L.m.

7-8 h post-infection, infected MDCK cells were detached from the substrate by being incubated for 10 min with a mixture of 200 µL of 0.25% trypsin-EDTA. Solutions in each well were pipetted up and down 6 times to ensure single cell suspensions, and 200 µL of complete media was added to inactivate trypsin in each well. Suspensions were transferred into 35-µm cell strainers, (Falcon, 352235) and spun through at 500 x g followed by fixation in 1% paraformaldehyde. Samples were then washed once in PBS and stored in PBS with 1% BSA. Flow cytometry analysis was performed on the BD FACS Canto RUO analyzer (University of Washington Cell Analysis Facility). 10,000-20,000 cells were analyzed per each replicate. To ensure analysis of single cells, the bulk of the distribution of cell counts was gated using the forward versus side scatter plot. This gating strategy ensures that single cells are analyzed and debris or cell doublets or triplets are eliminated from the analysis. A second gating step was then performed to exclude cells that autofluoresce by measuring the fluorescence of control-uninfected cells and gating the population of infected cells to exclude autofluorescence.

MDCK cell transfection with siRNA

For each well of a 24-well plate, $2x10^4$ MDCK cells suspended in serum free media were reverse-transfected with siRNAs at 20 nM final concentration using 0.25 µL lipofectamine RNAiMAX (Invitrogen 13778075). The transfection mix was replaced by full media 8 h later. Synthetic siRNA pools (including 2 distinct siRNA sequences) to target CDH1 were purchased from Dharmacon (Table S4). MDCK cells were treated with control (non-targeting, siGLO and Kif11) or experimental siRNA in accordance with the manufacturer instructions. Specifically, to demonstrate that transfection performed was sufficient to get siRNAs into the cells, we transfected cells with synthetic siRNA, siGLO, that makes cell exposed to it fluorescent 24 h post-transfection To track cell cycle phenotype and to verify that knockdown has occurred with our protocol, we transfected cells with siKif11 which results in substantial cell death of transfected cells approximately 24-48 h post-transfection and can be verified by microscopy with phase optics. Bacterial infections were performed approximately 72 h after transfection.

RT-PCR

To confirm the knockdowns, MDCK cells treated with control (non-targeting) or experimental siRNA 72 h after transfection (approximate cell concentration was $1.6x10^5$ cells/ well) were harvested and lyzed using the QIAshredder Kit (Qiagen; 79656). mRNA was harvested using the RNeasy Plus Micro Kit (Qiagen; 74004) and eluted in 30 µL RNAase free water RNA concentrations were measured spectrophotometrically (NanoDrop) and were comparable

between conditions. cDNA was prepared using the Superscript III First-strand Synthesis SuperMix (Invitrogen; 18080085). RT-qPCR was performed using the SYBR qPCR Master mix by Arraystar Inc. Genes of interest were amplified using primers indicated in Supplementary Table S9. Briefly the steps followed were: (1) perform RT-qPCR for each target gene and the housekeeping gene GAPDH; (2) determine gene concentration using the standard curve with Rotor-Gene Real-Time Analysis Software 6.0; (3) calculate relative amount of the target gene relative to GAPDH.

Fabrication of polyacrylamide hydrogels and traction force microscopy (TFM)

Polyacrylamide hydrogel fabrication was done as previously described [60]. Glass-bottom plates with 24 wells (MatTek; P24G-1.5-13-F) were incubated for 1 h with 500 µL of 1 M NaOH, then rinsed with distilled water, and incubated with 500 µL of 2% 3-aminopropyltriethoxysilane (Sigma; 919-30-2) in 95% ethanol for 5 min. Following rinsing with water 500 µL of 0.5% glutaraldehyde were added to each well for 30 min. Wells were rinsed with water again and dried at 60°C. To prepare polyacrylamide hydrogels of 3 kPa, mixtures containing 5% acrylamide (Sigma; A4058) and 0.1% bis-acrylamide (Fisher; BP1404-250) were prepared[60]. Two mixtures were prepared, the second of which contained 0.03% 0.2 µm–diameter fluorescent beads (Invitrogen, F8811) for TFM experiments. 0.06% ammonium persulfate and 0.43% TEMED were then added to the first solution to initiate polymerization. First, 3.6 µL of the first mixture without the beads was added at the center of each well, capped with 12-mm untreated circular glass coverslips, and allowed to polymerize for 20 min. After coverslip removal 2.4 µL of the mixture containing tracer beads was added and sandwiched again with a 12-mm untreated circular glass coverslip and allowed to polymerize for 20 min. Next, 50 mM HEPES at pH 7.5 was added to the wells, and coverslips were removed. Hydrogels were UV-sterilized for 1 h and then activated by adding 200 µL of 0.5% weight/volume heterobifunctional cross-linker Sulfo-SANPAH (ProteoChem; c1111) in 1% dimethyl sulfoxide (DMSO) and 50 mM HEPES, pH 7.5, on the upper surface of the hydrogels and exposing them to UV light for 10 min. Hydrogels were washed with 50 mM HEPES at pH 7.5 and were coated with 200 µL of 0.25 mg/ml rat tail collagen I (Sigma-Aldrich; C3867) in 50 mM HEPES at pH 7.5 overnight at room temperature. Next morning, collagen was washed with HEPES and gels were stored in HEPES.

TFM was performed as previously described [1, 11, 61]. Prior to seeding hydrogels were equilibrated with cell media for 30 min at 37°C. Cells were then seeded to a concentration of $2x10^5$ cells per well directly onto the hydrogels 24 h prior to infection. Cells are then either infected or not with

low dosage of L.m. and imaging started 4 h post-infection. Multi-channel time-lapse sequences of fluorescence (to image the beads within the upper portion of the hydrogels) and phase contrast images (to image the cells) were acquired using an inverted Nikon Eclipse Ti2 with an EMCCD camera (Andor Technologies) using a 40X 0.60NA Plan Fluor air objective or a 20x 0.75NA Plan Apo air objective and MicroManager software package[62]. The microscope was surrounded by a box type incubator (Haison) maintained at 37°C and 5% CO_2. Images were acquired every 10 min for approximately 8 h. Subsequently, at each time interval we measured the 2D deformation of the substrate at each point using an image correlation technique similar to particle image velocimetry. We calculated the local deformation vector by performing image correlation between each image and an undeformed reference image which we acquired by adding 10% SDS at the end of each recording to detach the cells from the hydrogels. We used interrogation windows of 32 x 8 pixels (window size x overlap). Calculations of the two-dimensional traction stresses that cell monolayers exert on the hydrogel are described elsewhere [1, 10].

Atomic Force Microscopy (AFM) for determination of cell stiffness upon infection

A Bioscope Resolve AFM (Bruker, Santa Barbara) was used for MDCK cell stiffness measurements. The AFM operates with the Nanoscope 9.4 software and the data was analyzed using Nanoscope Analysis 1.9 software. The AFM was integrated with an inverted optical microscope (Zeiss AXIO Observer Z1) to allow for correlation with fluorescence and light microscopy. Fluorescence microscopy was used to position the AFM tip over the MDCK cells that resided on glass substrates and were immersed in PBS and was critical for assessing which cells have internalized fluorescent bacteria.

First, we measured cell stiffness using the PFQNM-LC-A-CAL probe (Bruker) that has a conical shape (15 degrees half-cone angle) terminated with 130 nm diameter sphere, and a spring constant 0.096 nN nm^{-1} (pre-calibrated by manufacturer using Laser Doppler Vibrometer). We performed force-volume mapping using a ramp size of 4 μm, windows of 30 μm x 30 μm, 64 samples per line x 64 lines, ramp rate of 10 Hz, and a trigger force threshold of 600 pN. Since the indentation depth of >0.5 μm far exceeded the diameter of the spherical tip apex (130 nm), data were analyzed using the Sneddon Model on the extend curves (no adhesion). A total of 5 different windows were recorded for each condition.

We also probed cellular stiffness using colloidal probes with 5 μm diameter spheres on a pre-calibrated silicon nitride cantilever purchased from Novascan (PT.Si02.SN.5.CAL). Spring constant was 0.16 Nm^{-1} (pre-calibrated by manufacturer). Force-distance spectroscopy

measurements were conducted with a ramp rate 0.2 Hz, trigger force threshold 1 nN, and ramp size 6 μm (to accommodate for increased adhesion due to larger contact area). At each field of view, we selected 4 cells and collected 10 measurements per cell. A total of 4 different fields of view were selected for each condition, leading to 16 cells examined per condition. Data were analyzed using the Hertz Model and the extend curves (no adhesion). Each AFM tip was used only for one experiment and then discarded.

RNA isolation and RNA sequencing

Sample Preparation G-MDCK cells G-MDCK cells were cultured in high glucose DMEM medium (Thermofisher; 11965092) containing 4500 mg/L glucose and supplemented with 10% FBS (GemBio; 900-108). To generate confluent cell monolayers, 24-well plates glass-bottom for microscopy were coated with 50 μg/ml rat-tail collagen-I (diluted in 0.2 N acetic acid) for 1 h at 37°C, air-dried for 15 min, and UV-sterilized for 30 min in a tissue culture hood. MDCK cells were seeded at a density of 2 × 10^5 cells/well for 24 h. 24 h post-seeding MDCK cells were exposed to L.m. (MOI=200) for 30 min. After washing out the bacteria three times with PBS, media containing 20 μg/mL gentamycin was added to cells to kill extracellular bacteria. 24 h post-infection cells were trypsinized and either left in tubes or sorted into infected and uninfected populations. All tubes containing cells for RNA extraction were treated in parallel (4 replicates per condition). Cells in solution were spun down and lyzed using the QIAshredder Kit (Qiagen; 79656). mRNA was harvested using the RNeasy Plus Micro Kit (Qiagen; 74004) and eluted in 30 μL RNAase free water. A NanoDrop ND-1000 spectrophotometer was used to determine concentration (abs 260) and purity (abs260/abs230) of total RNA samples. Agarose gel electrophoresis was used to check the integrality of total RNA samples (performed by Arraystar Inc.).

Library preparation and RNA sequencing: The total RNA was depleted of rRNAs by Arraystar rRNA Removal Kit. We used Illumina kits for the RNA-seq library preparation, which included procedures of RNA fragmentation, random hexamer primed first strand cDNA synthesis, dUTP based second strand cDNA synthesis, end-repairing, A-tailing, adaptor ligation and library PCR amplification. Finally, the prepared RNA-seq libraries were qualified using Agilent 2100 Bioanalyzer and quantified by qPCR absolute quantification method. The sequencing was performed using Illumina NovaSeq 6000 using the High-Output Kit with 2x150 read length. We had an average of 40 million reads per sample. The DNA fragments in well mixed libraries were denatured with 0.1M NaOH to generate single-stranded DNA molecules, loaded onto channels of the flow cell at 8 pM concentration, and amplified in situ using TruSeq

SR Cluster Kit v3-cBot-HS (#GD-401-3001, Illumina). Sequencing was carried out using the Illumina X- ten/NovaSeq according to the manufacturer's instructions. Sequencing was carried out by running 150 cycles.

***Transcriptome assembly and differentially expressed gene identification**:* Raw sequencing data generated from Illumina X-ten/NovaSeq that pass the Illumina chastity filter were used for following analysis. Trimmed reads (trimmed 5', 3'-adaptor bases) were aligned to the reference genome (CanFam3). Based on alignment statistical analysis (mapping ratio, rRNA/mtRNA content, fragment sequence bias), we determined whether the results can be used for subsequent data analysis. To examine the sequencing quality, the quality score plot of each sample was plotted. Quality score Q is logarithmically related to the base calling error probability (P): $Q = -10\log_{10}(P)$. For example, Q30 means the incorrect base calling probability to be 0.001 or 99.9% base calling accuracy (see Table S5). After quality control, the fragments were 5', 3'-adaptor trimmed and filtered ≤ 20 bp reads with Cutadapt software. The trimmed reads were aligned to the reference genome with Hisat 2 software. The fragment statistical information is listed in Table S6. In a typical experiment, it is possible to align 40 ~ 90% of the fragments to the reference genome. However, this percentage depends on multiple factors, including sample quality, library quality and sequencing quality. Sequencing reads are classified into the following classes: (1) Mapped : reads aligned to the reference genome (including mRNA, pre-mRNA, poly-A tailed lncRNA and pri-miRNA); (2) mtRNA and rRNA: fragments aligned to rRNA, mtRNA; and (3) Unmapped: Reads that are not aligned.

Differentially expressed genes and differentially expressed transcripts are calculated. The novel genes and transcripts are also predicted. The expression level (FPKM value) of known genes and transcripts were calculated using ballgown through the transcript abundances estimated with StringTie. The number of identified genes and transcripts per group was calculated based on the mean of FPKM in group ≥ 0.5. Fragments per kilobase of transcript per million mapped reads (FPKM) is calculated with the formula: $\boldsymbol{FPMK} = \frac{\boldsymbol{C} \times \boldsymbol{10^6}}{\boldsymbol{L} \times \boldsymbol{N}}$, where C is the number of fragments that map to a certain gene/ transcript, L is the length of the gene/transcript in Kb and N is the fragments number that map to all genes/transcripts. Differentially expressed gene and transcript analyses were performed with R package ballgown. Fold change (cutoff 1.5), p-value (≤ 0.05) and FPKM (≥ 0.5 mean in one group) were used for filtering differentially expressed genes and transcripts.

Principal Component analysis (PCA) and mRNA Function Enrichment Analysis

Principal Component Analysis (PCA) and Hierarchical Clustering scatter plots and volcano plots were calculated for the differentially expressed genes in R or Python environment for statistical computing and graphics. PCA was performed using the plotPCA function in R with genes that have the ANOVA p value ≤ 0.05 on FPKM abundance estimations (Not available for samples with no replicates). Kyoto Encyclopedia of Genes and Genomes (KEGG) pathway analyses of the whole data set of DEG were performed using the R package GAGE "Generally Acceptable Gene set Enrichment" (GAGE v.2.22.0) package implemented in R. The analysis allowed us to determine whether the differentially expressed mRNAs are enriched in certain biological pathways. The p-values calculated by Fisher's exact test are used to estimate the statistical significance of the enrichment of the pathways between the two groups. The R package "Pathview" v.1.12.0 and KEGGGraph v1.30.0 were used to visualize gene set expression data in the context of functional pathways.

Immunostaining of fixed samples

Uninfected or L.m.-infected MDCK cells residing on glass substrates were incubated with 1 µg/mL Hoechst (Thermofisher; D1306) to stain the cells' nuclei for 10 min at ?? degrees prior to fixation. The following steps were carried out at RT. Cells were washed with PBS and fixed with 4% EM grade formaldehyde in PBS for 10 min. Following a wash with PBS, samples were permeabilized for 5 min in 0.2% Triton X-100 in PBS and washed again with PBS. Samples were then blocked for 30 min with 5% BSA in PBS and then incubated with primary antibodies (Table S2) diluted 1:100 in PBS containing 2% BSA for 1 h. Samples were washed in PBS three times and then incubated with the appropriate secondary fluorescent antibodies (Invitrogen) diluted 1:250 in PBS containing 2% BSA for 1 h. For actin staining we used 0.2 µM AlexaFluor488 phalloidin. Samples were washed three times in PBS and stored in 1 mL PBS for imaging. *N* > 8 mounds were analyzed per condition (N> 1200 cells). For epifluorescence imaging, we used an inverted Nikon Eclipse Ti2 with an EMCCD camera (Andor Technologies) and a 40x 0.60NA Plan Fluor air or a 20x 0.75NA Plan Apo air objective and MicroManager software. For confocal imaging we used a Yokogawa W1 Spinning Disk Confocal with Borealis upgrade on a Leica DMi6 inverted microscope with a 50um Disk pattern, a 63x 1.2NA Plan Apo water objective and MicroManager software.

Multiplexed magnetic Luminex immunossay and data analysis

Samples were centrifuged at 8000xg to remove debris and assayed immediately. The remaining samples were stored at -80°C. The assay was performed at and all reagents were brought to room temperature before use. 25 µL of each standard or control was added into the appropriate

wells. 25 µL of assay buffer was added for standard 0 (background). 25 µL of assay buffer was added to the sample wells. 25 µL of tissue culture media solution was added to the background, standards, and control wells. 25 µL of sample supernatant was added into the appropriate wells. The beads were vortexed briefly, and 25 µL of the mixed beads was added to each well. We used the Canine Cytokine Magnetic Bead Panel 96-Well Plate Assay (Millipore Sigma, # CCYTMG-90K-PX13). The plate was sealed, wrapped with foil and incubated with agitation on a plate shaker over for 2 h. Following that, the well contents were gently removed, and the plate was washed two times by manually adding and removing 200 µL wash buffer per well. Then, 25 µL of detection antibodies were added into each well. The plate was again sealed and covered with foil and incubated with agitation for 1 h. After incubation, 25 µL Streptavidin-Phycoerythrin was added to each well containing the detection antibodies. (Plate was not washed after incubation with detection antibodies as per manufacturer's protocol). The plate was sealed and covered with foil and incubated with agitation for 30 min. Then, well contents were gently aspirated out, and the plate was washed two times. Finally, 150 µL of sheath fluid was added to all wells, and the beads were resuspended on a plate shaker for 5 min at room temperature. The plate was run on Bio-Plex 200 flow cytometer. Data analysis was performed using the Bio-Plex Manager 5.0. We used a 5-parameter log fit curve against the signal intensities for the analytes present in the Canine Cytokine Magnetic bead Panel (GM-CSF, IFN-γ, IL-2, IL-6, IL-7, IL-8, IL-15, IP-10, KC-like, IL-10, IL-18, MCP-1, TNF-A) to generate a standard curve for the assay. Sample signal intensities were then back interpolated to the standard curve to determine the analyte concentrations. The upper limit of quantitation (ULOQ) was determined as the highest point at which the interpolated data of the standard curve are within 25% (±) of the expected recovery. ULOQ represents the highest concentration of an analyte that can be accurately quantified. Similarly, the lower limit of quantitation (LLOQ) was determined as the lowest point at which the interpolated data of the standard curve are within 25% (±) of the expected recovery. LLOQ represents the lowest concentration of an analyte that can be accurately quantified.

Nuclear segmentation, tracking and characterization of dynamics of motion

We acquired time-lapse fluorescence confocal images of Hoechst-stained host epithelial cell nuclei and of the bacterial fluorescence using a spinning disk confocal with a 63x 1.2NA Plan Apo water objective at 30 min intervals. For each time point, z stacks including the total height of the cell layer was also acquired with a z spacing of 0.7 µm. To segment and track the host cell nuclei in 3D we used using IMARIS software (Bitplane) by first using the spot detection

(segmentation) and then the tracking modules. The x, y and z positions of all identified objects and tracks were exported for import into MATLAB (MathWorks) for further analysis was performed to calculate cell displacements and speeds of migration. For mean square displacement analysis (MSD) we used the @msdanalyzer MATLAB class[63]. We first computed for each cell its MSD as a function of time interval, Δt: $MSD(\Delta t) = \langle|\mathbf{r}_i(t + \Delta t) - \mathbf{r}_i(t)|^2\rangle$, where $\mathbf{r}_i(t)$ indicates the position of cell i at time t and $\langle\ldots\rangle$ denotes the average over all time t. We then calculated the weighted average of all MSD curves, where weights are taken to be the number of averaged delay in individual curves. In the average MSD plots the grayed area represents the weighted standard deviation over all MSD curves and the errorbars the standard error of the mean. We estimated the self-diffusion coefficient $D_s = \lim_{\Delta t \to \infty} MSD(\Delta t)/(4\Delta t)$ by linear weighted fir of the mean MSD curve on the first 500 min. Finally, for analysis of the motion type of the objects (i.e. diffusive, subdiffusive or superdiffusive) we performed log-log fitting and modeled the MSD curve by the following power law $MSD(\Delta t) = \Gamma \times t^{\alpha}$. For purely diffusive motion α=1, for subdiffusive α<1 and for superdiffusive α>1. To determine the power law coefficient we take the logarithm of the power law so that it turns linear: $\log(MSD) = \alpha \times \log(t) + \log(\Gamma)$ and by fitting log(MSD) versus log(t) we retrieve α. For more details please refer to @msdanalyzer MATLAB class[63].

Cell segmentation and extraction of cell shape characteristics

Epithelial cells were segmented based on pericellular E-cadherin localization using the Tissue Analyzer ImageJ plugin[64]. Masks of individual cells were exported and imported in MATLAB for further analysis. We used custom-made code for calculating the cell area, orientation, aspect ratio and tortuosity ($perimeter/\sqrt{area}$). To quantify whether there is any nematic ordering in the orientation of cells we calculated for each cells how many of its 100, 200 or 300 nearest neighbors share similar orientation and also used the OrientationJ plugin[65].

Characterization of mound volume and infection focus area

We acquired confocal images of Hoechst-stained host epithelial cell nuclei and of the fluorescent bacteria in fixed samples using a spinning disk confocal with a 63x 1.2NA Plan Apo water objective and a z spacing of 0.2 μm. The fields of view were selected so that the infection mounds are approximately at the center of field of view. To quantify the size of the mounds we integrated the fluorescence intensity of the nuclei for all the acquired z-stacks and then integrated along the x-axis obtaining a line integral. We then subtracted the minimum value and calculated the area under the curve as a proxy of the volume of the mound. For each different experiment all values

were normalized relative to the corresponding values for infected MDCK cells treated with vehicle control.

There is no standard metric in the field to measure the efficiency of *L. monocytogenes* cell-to-cell spread through a monolayer of host cells. To characterize the area of the infection focus we chose to draw a convex hull, the smallest convex polygon that encompasses a set of points, around the bacteria [60]. This is a computationally inexpensive and consistent way to measure the efficiency of *L. monocytogenes* spread.

Live/dead staining, TUNEL and BrdU assays

We used the NucRed Dead 647 ReadyProbes Reagent (Thermofisher; R37113), a cell impermeant stain that emits bright far-red fluorescence when bound to DNA, for staining dead cells. This reagent stains the cells without plasma membrane integrity and was used to measure cell viability. Briefly, one drop of this reagent was added in each well containing live cells and cells were incubated with this reagent for 20 min before samples were imaged.
In addition, we used the TUNEL assay for DNA fragmentation (ABCAM; ab66108) as a means to detect number of apoptotic cells. For staining cells for DNA fragmentation, we followed the manufacturer's instructions and quantified fluorescein-labeled DNA by flow cytometry for cells at 24 h post-infection. We used the BrdU staining kit for flow cytometry APC (eBioscience; 8817-6600-42) to identify proliferating cells. However, BrdU can also stain apoptotic cells due to the break-up of their genomic DNA by cellular nucleases. For the BrdU assay we followed the manufacturer's instructions and incubated cells at 24 h post-infection with 10 μm BrdU for 4 h at 37°C before harvesting the cells and proceeding with the above protocol.

Computational modeling of cell monolayers during infection

We assume the cells are arranged in the monolayer as regular hexagons with side length of 7 μm, the thickness of the monolayer is set to 7 μm in the undeformed state following experimental observations and previous computational works [66-68] . We model the mechanical behaviour of the cell distinguishing two main parts: active and passive. The active part represents the actomyosin contractility motors and the passive one the rest of the cytoskeleton [69, 70]. In this way, both parts are assumed linear elastic material, where the total stiffness of each cell is the sum of both ($E_{cell} = E_{active} + E_{passive}$). Following the experimental AFM measurements, the elastic modulus of uninfected cells is set in 1000 Pa and 250 Pa for the infected cells (E_{cell}). As a first approach, we assume both parts of the cells are working in parallel, as it is indicated in the Figure 5A , therefore, the active (E_{active}) and passive ($E_{passive}$) elastic modulus are 500 Pa for uninfected cells and 125 Pa for infected cells. We assume the

passive part of the cell nearly incompressible, thus the Poisson ratio is set to 0.48 [70]. The active part of the cell is mainly actomyosin contraction and we assume this contraction is not isotropic but that it just occurs in the plane of the monolayer. Thus, the Poisson ratio of the active part is assumed zero to uncouple effects in the monolayer plane and in the vertical direction for the active part of the cell.

We model the substrate as a linear elastic material with elastic modulus of 3 kPa corresponding to collagen I-coated polyacrylamide hydrogels used in the TFM experiments. We consider in the model both cell-cell and cell-matrix interactions. We model cell-cell interactions as a continuum and adopt a linear elastic model with stiffness of 4.9 nN/μm and 1.23 nN/μm in normal and shear direction, respectively. When we simulate the inhibition of cell-cell adhesions we set these values close to zero, meaning that cells do not interact anymore mechanically with each other. Meanwhile, the cell-ECM interactions are simulated as cohesive contacts. We assume that cells adhere in different ways to the substrate [14, 71] depending if there are cell-cell interactions or not. If the cell-cell adhesions are active (cell monolayer behaves collectively), its adhesion to the substrate is weaker than if the cell-cell adhesions are inhibited (cells forming the monolayer behave individually) which is also in agreement with the experimental observations. The rigid adhesion is assumed to be 1000 nN/μm both in normal and shear direction, and the weak one 10 nN/μm in normal direction and negligible in shear direction. We analyse a short period of time, in which just one contraction and, if it occurs, one protrusion event are simulated. These events could be repeated in time and as a result infection mounding would be more prominent.

We implement the model into a commercial finite element model (FE-based) ABAQUS[70]. To simulate cells two meshes are overlapping sharing the nodes to represent the active and passive components of the cell. We discretise the model with tetrahedral and hexahedral linear elements of average size 2 mm.

Data availability

The RNA sequencing data (FASTq files) generated during this study and subsequent analysis have been submitted to the Gene Expression Omnibus (GEO) database. These data are available at: https://www.ncbi.nlm.nih.gov/geo/query/acc.cgi?acc=GSE135123 and the series record that provides access to all of the data is GSE135123. All the differential expression analysis results of this study are included as supplementary tables in this article.

Name and source	Species	Genotype/Descriptions

JAT607	*L. monocytogenes* 10403S	ActAp::mTagRFP
JAT605	*L. monocytogenes* 10403S	GFP
Δ*inlC*	*L. monocytogenes* 10403S	Δ*inlC* ActAp::mTagRFP
Obtained from Bakardjiev lab, UCSF	*L. monocytogenes* 10403S	Δ*inlP*
JAT983	*L. monocytogenes* 10403S	LLOG486D ActAp::mTagRFP
JAT	*L. monocytogenes* 10403S	Δ*hly*

Table S1: Bacterial strains

Antibody	**Specifications**	**Source**
anti-vimentin	Mouse monoclonal V9	Abcam; ab8069
anti-pan cytokeratin	Mouse monoclonal AE1/AE3	ThermoFisher; 53-9003-80
anti-tubulin	Rabbit monoclonal EP1332Y	Abcam; ab52866
anti-β-catenin		
anti-NF-κB	Rabbit monoclonal E379	Abcam; ab190589
anti-E-cadherin	Rabbit monoclonal 24E10	Cell Signaling; 3195
Reagent	**Specifications**	**Source**
Hoechst	Dissolved at 1 mg/ml in DMSO and used at 1:1000	Thermofisher; D1306
AlexaFluor488 phalloidin	Used at 0.2 μM	Thermo Fisher; A12379

Table S2: Antibodies and reagents

Drug	**Target**	**Concentration**	**Source**
Para-nitroblebbistatin	Myosin II inhibitor	50 μM	Fisher; NC1706059
Y27632	ROCK inhibitor	30 μM	Sigma: 129830-38-2
Z-VAD-FMK	Pancaspase inhibitor	100 μM	MilliporeSigma; 5.30389.0001
GSK'872	RIPK3 inhibitor	5 μM	Fisher; 64-921-0
Rapamycin	mTOR inhibitor	1 μM	Fisher; 53123-88-9
NEMO binding peptide	NF-κB inhibitor	50 μM	Fisher; 48-003-0500UG
LNiL	Src inhibitor	10 μM	Fisher; PHZ1223

Table S3: Inhibitors and working concentrations

Gene (protein)	Product Name	Catalog number
Negative control non-targeting	ON-TARGETplus Non- Targeting Pool	D-001810-10
E-cadherin	Custom CDH1 duplex	CTM-521910 and CTM-521911

Table S4: Synthetic siRNA pools used in this study

Acknowledgements

Our thanks to M. Footer, M. Walkievicz and members of the Theriot Lab for discussions and experimental support. We thank the Stanford Cell Sciences Imaging Facility for using their Atomic Force Microscope. This part of the project was supported, in part, by Award Number 1S10OD021514-01 from the National Center for Research Resources (NCRR). Its

contents are solely the responsibility of the authors and do not necessarily represent the official views of the NCRR or the National Institutes of Health. RNA Seq and RT-qPCR were performed by Arraystar Inc. and multiplex immunoassay by PBL Assay Sciences. This work was supported by NIH R01AI036929 (J.A.T), HHMI (J.A.T) and the American Heart Association, Award number: 18CDA34070047 (E.E.B).

REFERENCES

1. Lamason, R. L.; Bastounis, E.; Kafai, N. M.; Serrano, R.; Del Alamo, J. C.; Theriot, J. A.; Welch, M. D., Rickettsia Sca4 Reduces Vinculin-Mediated Intercellular Tension to Promote Spread. *Cell* **2016,** *167* (3), 670-683.e10.
2. Faralla, C.; Bastounis, E. E.; Ortega, F. E.; Light, S. H.; Rizzuto, G.; Nocadello, S.; Anderson, W. F.; Robbins, J. R.; Theriot, J. A.; Bakardjiev, A. I., Listeria monocytogenes InlP interacts with afadin and facilitates basement membrane crossing. *bioRxiv* **2018**.
3. Rajabian, T.; Gavicherla, B.; Heisig, M.; Muller-Altrock, S.; Goebel, W.; Gray-Owen, S. D.; Ireton, K., The bacterial virulence factor InlC perturbs apical cell junctions and promotes cell-to-cell spread of Listeria. *Nat Cell Biol* **2009,** *11* (10), 1212-8.
4. Faralla, C.; Bastounis, E. E.; Ortega, F. E.; Light, S. H.; Rizzuto, G.; Gao, L.; Marciano, D. K.; Nocadello, S.; Anderson, W. F.; Robbins, J. R.; Theriot, J. A.; Bakardjiev, A. I., Listeria monocytogenes InlP interacts with afadin and facilitates basement membrane crossing. *PLoS Pathog* **2018,** *14* (5), e1007094.
5. Ortega, F. E.; Koslover, E. F.; Theriot, J. A., Listeria monocytogenes cell-to-cell spread in epithelia is heterogeneous and dominated by rare pioneer bacteria. *eLife* **2019,** *8*, e40032.
6. Saw, T. B.; Doostmohammadi, A.; Nier, V.; Kocgozlu, L.; Thampi, S.; Toyama, Y.; Marcq, P.; Lim, C. T.; Yeomans, J. M.; Ladoux, B., Topological defects in epithelia govern cell death and extrusion. *Nature* **2017,** *544*, 212.
7. Kocgozlu, L.; Saw, Thuan B.; Le, Anh P.; Yow, I.; Shagirov, M.; Wong, E.; Mège, R.-M.; Lim, Chwee T.; Toyama, Y.; Ladoux, B., Epithelial Cell Packing Induces Distinct Modes of Cell Extrusions. *Current Biology* **2016,** *26* (21), 2942-2950.
8. Park, J. A.; Atia, L.; Mitchel, J. A.; Fredberg, J. J.; Butler, J. P., Collective migration and cell jamming in asthma, cancer and development. *J Cell Sci* **2016,** *129* (18), 3375-83.
9. Mitchel, J. A.; Das, A.; O'Sullivan, M. J.; Stancil, I. T.; DeCamp, S. J.; Koehler, S.; Butler, J. P.; Fredberg, J. J.; Nieto, M. A.; Bi, D.; Park, J.-A., The unjamming transition is distinct from the epithelial-to-mesenchymal transition. *bioRxiv* **2019**, 665018.
10. Bastounis, E.; Meili, R.; Álvarez-González, B.; Francois, J.; del Álamo, J. C.; Firtel, R. A.; Lasheras, J. C., Both contractile axial and lateral traction force dynamics drive amoeboid cell motility. *The Journal of Cell Biology* **2014,** *204* (6), 1045-1061.
11. del Álamo, J. C.; Meili, R.; Alonso-Latorre, B.; Rodríguez-Rodríguez, J.; Aliseda, A.; Firtel, R. A.; Lasheras, J. C., Spatio-temporal analysis of eukaryotic cell motility by improved force cytometry. *Proc. Nat. Acad. Sci.* **2007,** *104* (33), 13343-8.
12. Bastounis, E. E.; Yeh, Y. T.; Theriot, J. A., Subendothelial stiffness alters endothelial cell traction force generation while exerting a minimal effect on the transcriptome. *Sci Rep* **2019,** *9* (1), 18209.
13. Rengarajan, M.; Hayer, A.; Theriot, J. A., Endothelial Cells Use a Formin-Dependent Phagocytosis-Like Process to Internalize the Bacterium Listeria monocytogenes. *PLoS Pathog* **2016,** *12* (5), e1005603.
14. Sunyer, R.; Conte, V.; Escribano, J.; Elosegui-Artola, A.; Labernadie, A.; Valon, L.; Navajas, D.; Garcia-Aznar, J. M.; Munoz, J. J.; Roca-Cusachs, P.; Trepat, X., Collective cell

durotaxis emerges from long-range intercellular force transmission. *Science* **2016,** *353* (6304), 1157-61.
15. Ebner, K.; Bandion, A.; Binder, B. R.; de Martin, R.; Schmid, J. A., GMCSF activates NF-kappaB via direct interaction of the GMCSF receptor with IkappaB kinase beta. *Blood* **2003,** *102* (1), 192-9.
16. Schreck, R.; Baeuerle, P. A., NF-kappa B as inducible transcriptional activator of the granulocyte-macrophage colony-stimulating factor gene. *Mol Cell Biol* **1990,** *10* (3), 1281-6.
17. Hildebrand, D. G.; Alexander, E.; Horber, S.; Lehle, S.; Obermayer, K.; Munck, N. A.; Rothfuss, O.; Frick, J. S.; Morimatsu, M.; Schmitz, I.; Roth, J.; Ehrchen, J. M.; Essmann, F.; Schulze-Osthoff, K., IkappaBzeta is a transcriptional key regulator of CCL2/MCP-1. *J Immunol* **2013,** *190* (9), 4812-20.
18. Ishikado, A.; Nishio, Y.; Yamane, K.; Mukose, A.; Morino, K.; Murakami, Y.; Sekine, O.; Makino, T.; Maegawa, H.; Kashiwagi, A., Soy phosphatidylcholine inhibited TLR4-mediated MCP-1 expression in vascular cells. *Atherosclerosis* **2009,** *205* (2), 404-12.
19. Teferedegne, B.; Green, M. R.; Guo, Z.; Boss, J. M., Mechanism of action of a distal NF-kappaB-dependent enhancer. *Mol Cell Biol* **2006,** *26* (15), 5759-70.
20. Feng, G.; Ohmori, Y.; Chang, P. L., Production of chemokine CXCL1/KC by okadaic acid through the nuclear factor-kappaB pathway. *Carcinogenesis* **2006,** *27* (1), 43-52.
21. Manna, S. K.; Ramesh, G. T., Interleukin-8 induces nuclear transcription factor-kappaB through a TRAF6-dependent pathway. *J Biol Chem* **2005,** *280* (8), 7010-21.
22. Hoesel, B.; Schmid, J. A., The complexity of NF-kappaB signaling in inflammation and cancer. *Mol Cancer* **2013,** *12*, 86.
23. Kang, H. B.; Kim, Y. E.; Kwon, H. J.; Sok, D. E.; Lee, Y., Enhancement of NF-kappaB expression and activity upon differentiation of human embryonic stem cell line SNUhES3. *Stem Cells Dev* **2007,** *16* (4), 615-23.
24. Li, S.; Lu, J.; Chen, Y.; Xiong, N.; Li, L.; Zhang, J.; Yang, H.; Wu, C.; Zeng, H.; Liu, Y., MCP-1-induced ERK/GSK-3beta/Snail signaling facilitates the epithelial-mesenchymal transition and promotes the migration of MCF-7 human breast carcinoma cells. *Cell Mol Immunol* **2017,** *14* (7), 621-630.
25. Zhang, T.; Balachandran, S., Bayonets over bombs: RIPK3 and MLKL restrict Listeria without triggering necroptosis. *J Cell Biol* **2019,** *218* (6), 1773-1775.
26. Dai, S.; Hirayama, T.; Abbas, S.; Abu-Amer, Y., The IkappaB kinase (IKK) inhibitor, NEMO-binding domain peptide, blocks osteoclastogenesis and bone erosion in inflammatory arthritis. *J Biol Chem* **2004,** *279* (36), 37219-22.
27. McFarland, A. P.; Burke, T. P.; Carletti, A. A.; Glover, R. C.; Tabakh, H.; Welch, M. D.; Woodward, J. J., RECON-Dependent Inflammation in Hepatocytes Enhances Listeria monocytogenes Cell-to-Cell Spread. *mBio* **2018,** *9* (3), e00526-18.
28. Dan, H. C.; Cooper, M. J.; Cogswell, P. C.; Duncan, J. A.; Ting, J. P. Y.; Baldwin, A. S., Akt-dependent regulation of NF-{kappa}B is controlled by mTOR and Raptor in association with IKK. *Genes & development* **2008,** *22* (11), 1490-1500.
29. Weichhart, T.; Hengstschläger, M.; Linke, M., Regulation of innate immune cell function by mTOR. *Nature reviews. Immunology* **2015,** *15* (10), 599-614.
30. Engstrom, P.; Burke, T. P.; Mitchell, G.; Ingabire, N.; Mark, K. G.; Golovkine, G.; Iavarone, A. T.; Rape, M.; Cox, J. S.; Welch, M. D., Evasion of autophagy mediated by Rickettsia surface protein OmpB is critical for virulence. *Nat Microbiol* **2019,** *4* (12), 2538-2551.
31. Ohsawa, S.; Vaughen, J.; Igaki, T., Cell Extrusion: A Stress-Responsive Force for Good or Evil in Epithelial Homeostasis. *Developmental cell* **2018,** *44* (3), 284-296.
32. Grieve, A. G.; Rabouille, C., Extracellular cleavage of E-cadherin promotes epithelial cell extrusion. *Journal of Cell Science* **2014,** *127* (15), 3331.
33. Matamoro-Vidal, A.; Levayer, R., Multiple Influences of Mechanical Forces on Cell Competition. *Current Biology* **2019,** *29* (15), R762-R774.

34. Senoo-Matsuda, N.; Johnston, L. A., Soluble factors mediate competitive and cooperative interactions between cells expressing different levels of Drosophila Myc. *Proceedings of the National Academy of Sciences* **2007,** *104* (47), 18543.
35. Hogan, C.; Dupre-Crochet, S.; Norman, M.; Kajita, M.; Zimmermann, C.; Pelling, A. E.; Piddini, E.; Baena-Lopez, L. A.; Vincent, J. P.; Itoh, Y.; Hosoya, H.; Pichaud, F.; Fujita, Y., Characterization of the interface between normal and transformed epithelial cells. In *Nat Cell Biol*, England, 2009; Vol. 11, pp 460-7.
36. Lubkov, V.; Bar-Sagi, D., E-cadherin-mediated cell coupling is required for apoptotic cell extrusion. *Curr Biol* **2014,** *24* (8), 868-74.
37. Leung, C. T.; Brugge, J. S., Outgrowth of single oncogene-expressing cells from suppressive epithelial environments. *Nature* **2012,** *482* (7385), 410-3.
38. Wagstaff, L.; Goschorska, M.; Kozyrska, K.; Duclos, G.; Kucinski, I.; Chessel, A.; Hampton-O'Neil, L.; Bradshaw, C. R.; Allen, G. E.; Rawlins, E. L.; Silberzan, P.; Carazo Salas, R. E.; Piddini, E., Mechanical cell competition kills cells via induction of lethal p53 levels. *Nat Commun* **2016,** *7*, 11373.
39. Kajita, M.; Hogan, C.; Harris, A. R.; Dupre-Crochet, S.; Itasaki, N.; Kawakami, K.; Charras, G.; Tada, M.; Fujita, Y., Interaction with surrounding normal epithelial cells influences signalling pathways and behaviour of Src-transformed cells. *Journal of Cell Science* **2010,** *123* (2), 171.
40. Chiba, T.; Ishihara, E.; Miyamura, N.; Narumi, R.; Kajita, M.; Fujita, Y.; Suzuki, A.; Ogawa, Y.; Nishina, H., MDCK cells expressing constitutively active Yes-associated protein (YAP) undergo apical extrusion depending on neighboring cell status. *Scientific Reports* **2016,** *6* (1), 28383.
41. Ishihara, E.; Nishina, H., The Hippo-YAP Pathway Regulates 3D Organ Formation and Homeostasis. *Cancers* **2018,** *10* (4), 122.
42. Moreno, E.; Valon, L.; Levillayer, F.; Levayer, R., Competition for Space Induces Cell Elimination through Compaction-Driven ERK Downregulation. *Curr Biol* **2019,** *29* (1), 23-34.e8.
43. Rahman, M. M.; McFadden, G., Modulation of NF-kappaB signalling by microbial pathogens. In *Nat Rev Microbiol*, England, 2011; Vol. 9, pp 291-306.
44. Jiang, T.; Grabiner, B.; Zhu, Y.; Jiang, C.; Li, H.; You, Y.; Lang, J.; Hung, M.-C.; Lin, X., CARMA3 is crucial for EGFR-Induced activation of NF-κB and tumor progression. *Cancer research* **2011,** *71* (6), 2183-2192.
45. Santoro, M. G.; Rossi, A.; Amici, C., NF-kappaB and virus infection: who controls whom. *Embo j* **2003,** *22* (11), 2552-60.
46. Brubaker, R. R., Interleukin-10 and Inhibition of Innate Immunity to Yersiniae: Roles of Yops and LcrV (V Antigen). *Infection and Immunity* **2003,** *71* (7), 3673.
47. Curto, P.; Riley, S. P.; Simoes, I.; Martinez, J. J., Macrophages Infected by a Pathogen and a Non-pathogen Spotted Fever Group Rickettsia Reveal Differential Reprogramming Signatures Early in Infection. *Front Cell Infect Microbiol* **2019,** *9*, 97.
48. Chen, J.; Chen, Z. J., Regulation of NF-κB by ubiquitination. *Current opinion in immunology* **2013,** *25* (1), 4-12.
49. Chen, Z. J., Ubiquitin signalling in the NF-kappaB pathway. *Nature cell biology* **2005,** *7* (8), 758-765.
50. Iwai, K., Diverse ubiquitin signaling in NF-kappaB activation. *Trends Cell Biol* **2012,** *22* (7), 355-64.
51. Gouin, E.; Adib-Conquy, M.; Balestrino, D.; Nahori, M. A.; Villiers, V.; Colland, F.; Dramsi, S.; Dussurget, O.; Cossart, P., The Listeria monocytogenes InlC protein interferes with innate immune responses by targeting the I{kappa}B kinase subunit IKK{alpha}. *Proc Natl Acad Sci U S A* **2010,** *107* (40), 17333-8.

52. Mansell, A.; Braun, L.; Cossart, P.; O'Neill, L. A., A novel function of InlB from Listeria monocytogenes: activation of NF-kappaB in J774 macrophages. *Cell Microbiol* **2000,** *2* (2), 127-36.
53. Drolia, R.; Tenguria, S.; Durkes, A. C.; Turner, J. R.; Bhunia, A. K., Listeria Adhesion Protein Induces Intestinal Epithelial Barrier Dysfunction for Bacterial Translocation. *Cell Host Microbe* **2018,** *23* (4), 470-484.e7.
54. Pannekoek, W.-J.; de Rooij, J.; Gloerich, M., Force transduction by cadherin adhesions in morphogenesis. *F1000Research* **2019,** *8*, F1000 Faculty Rev-1044.
55. Pentecost, M.; Otto, G.; Theriot, J. A.; Amieva, M. R., Listeria monocytogenes Invades the Epithelial Junctions at Sites of Cell Extrusion. *PLOS Pathogens* **2006,** *2* (1), e3.
56. Knodler, L. A.; Vallance, B. A.; Celli, J.; Winfree, S.; Hansen, B.; Montero, M.; Steele-Mortimer, O., Dissemination of invasive Salmonella via bacterial-induced extrusion of mucosal epithelia. *Proc Natl Acad Sci U S A* **2010,** *107* (41), 17733-8.
57. Co, J. Y.; Margalef-Catala, M.; Li, X.; Mah, A. T.; Kuo, C. J.; Monack, D. M.; Amieva, M. R., Controlling Epithelial Polarity: A Human Enteroid Model for Host-Pathogen Interactions. *Cell Rep* **2019,** *26* (9), 2509-2520.e4.
58. Ortega, F. E.; Rengarajan, M.; Chavez, N.; Radhakrishnan, P.; Gloerich, M.; Bianchini, J.; Siemers, K.; Luckett, W. S.; Lauer, P.; Nelson, W. J.; Theriot, J. A., Adhesion to the host cell surface is sufficient to mediate Listeria monocytogenes entry into epithelial cells. *Mol Biol Cell* **2017**.
59. Perez, T. D.; Tamada, M.; Sheetz, M. P.; Nelson, W. J., Immediate-early signaling induced by E-cadherin engagement and adhesion. *J Biol Chem* **2008,** *283* (8), 5014-22.
60. Bastounis, E. E.; Ortega, F. E.; Serrano, R.; Theriot, J. A., A Multi-well Format Polyacrylamide-based Assay for Studying the Effect of Extracellular Matrix Stiffness on the Bacterial Infection of Adherent Cells. *J Vis Exp* **2018,** (137).
61. Faralla, C.; Rizzuto, G. A.; Lowe, D. E.; Kim, B.; Cooke, C.; Shiow, L. R.; Bakardjiev, A. I., InlP, a New Virulence Factor with Strong Placental Tropism. *Infect Immun* **2016,** *84* (12), 3584-3596.
62. Edelstein, A. D.; Tsuchida, M. A.; Amodaj, N.; Pinkard, H.; Vale, R. D.; Stuurman, N., Advanced methods of microscope control using μManager software. *Journal of Biological Methods; Vol 1, No 2 (2014)* **2014**.
63. Tarantino, N.; Tinevez, J.-Y.; Crowell, E. F.; Boisson, B.; Henriques, R.; Mhlanga, M.; Agou, F.; Israël, A.; Laplantine, E., TNF and IL-1 exhibit distinct ubiquitin requirements for inducing NEMO–IKK supramolecular structures. *The Journal of Cell Biology* **2014,** *204* (2), 231.
64. Aigouy, B.; Umetsu, D.; Eaton, S., Segmentation and Quantitative Analysis of Epithelial Tissues. *Methods Mol Biol* **2016,** *1478*, 227-239.
65. Puspoki, Z.; Storath, M.; Sage, D.; Unser, M., Transforms and Operators for Directional Bioimage Analysis: A Survey. *Adv Anat Embryol Cell Biol* **2016,** *219*, 69-93.
66. Escribano, J.; Chen, M. B.; Moeendarbary, E.; Cao, X.; Shenoy, V.; Garcia-Aznar, J. M.; Kamm, R. D.; Spill, F., Balance of mechanical forces drives endothelial gap formation and may facilitate cancer and immune-cell extravasation. *PLoS computational biology* **2019,** *15* (5), e1006395-e1006395.
67. Schmedt, T.; Chen, Y.; Nguyen, T. T.; Li, S.; Bonanno, J. A.; Jurkunas, U. V., Telomerase immortalization of human corneal endothelial cells yields functional hexagonal monolayers. *PLoS One* **2012,** *7* (12), e51427.
68. O'Dea, R. D.; King, J. R., Continuum limits of pattern formation in hexagonal-cell monolayers. *J Math Biol* **2012,** *64* (3), 579-610.
69. Borau, C.; Kamm, R. D.; Garcia-Aznar, J. M., Mechano-sensing and cell migration: a 3D model approach. *Phys Biol* **2011,** *8* (6), 066008.
70. Moreo, P.; Garcia-Aznar, J. M.; Doblare, M., Modeling mechanosensing and its effect on the migration and proliferation of adherent cells. *Acta Biomater* **2008,** *4* (3), 613-21.

71. Escribano, J.; Sunyer, R.; Sanchez, M. T.; Trepat, X.; Roca-Cusachs, P.; Garcia-Aznar, J. M., A hybrid computational model for collective cell durotaxis. *Biomech Model Mechanobiol* **2018,** *17* (4), 1037-1052.

Figure 1

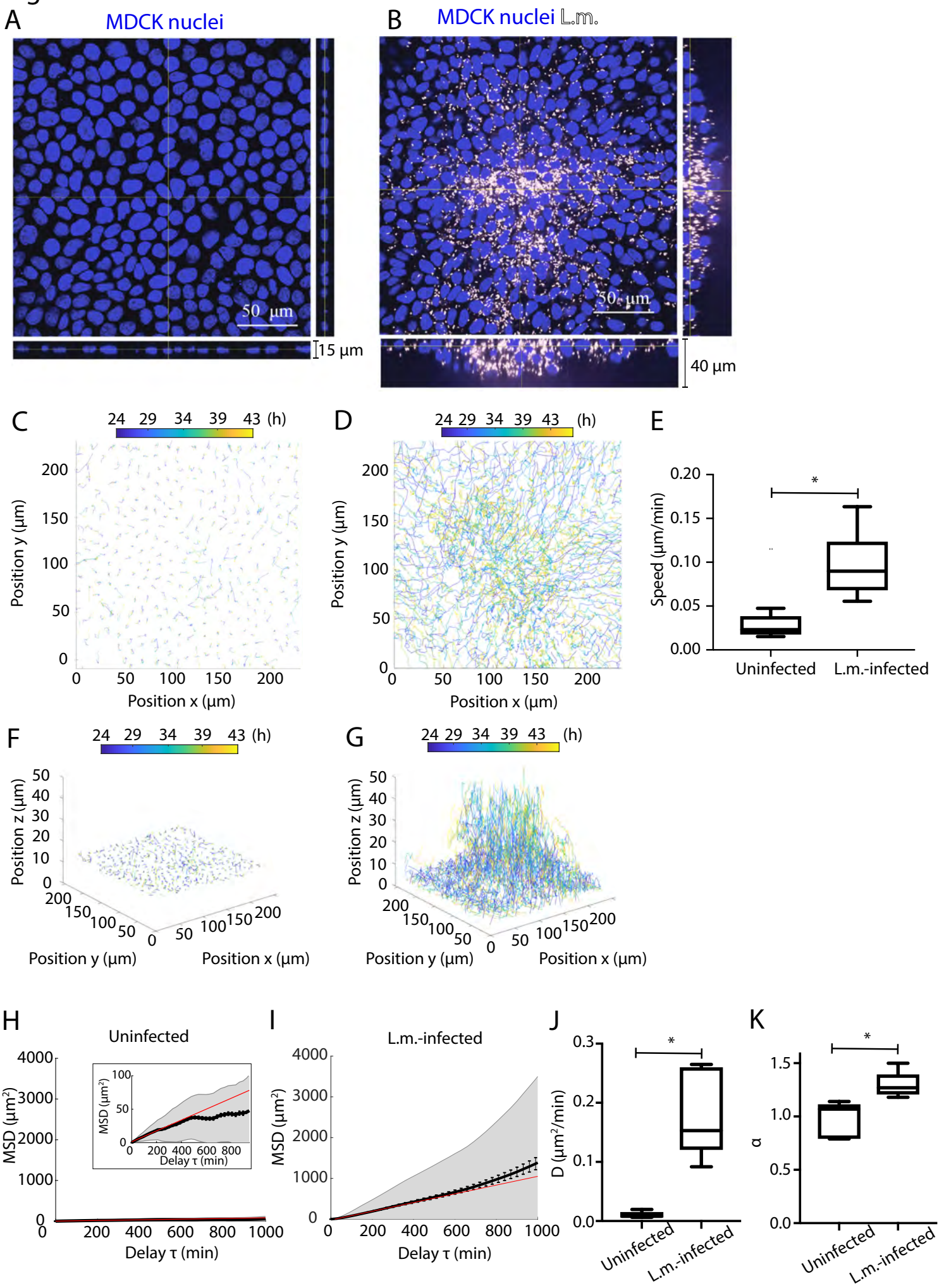
A
MDCK nuclei
50 µm
15 µm
B
MDCK nuclei L.m.
50 µm
40 µm
C
24 29 34 39 43 (h)
Position y (µm)
Position x (µm)
D
24 29 34 39 43 (h)
Position y (µm)
Position x (µm)
E
Speed (µm/min)
Uninfected
L.m.-infected
F
24 29 34 39 43 (h)
Position z (µm)
Position y (µm)
Position x (µm)
G
24 29 34 39 43 (h)
Position z (µm)
Position y (µm)
Position x (µm)
H
Uninfected
MSD (µm²)
Delay τ (min)
I
L.m.-infected
MSD (µm²)
Delay τ (min)
J
D (µm²/min)
Uninfected
L.m.-infected
K
α
Uninfected
L.m.-infected

Figure 2

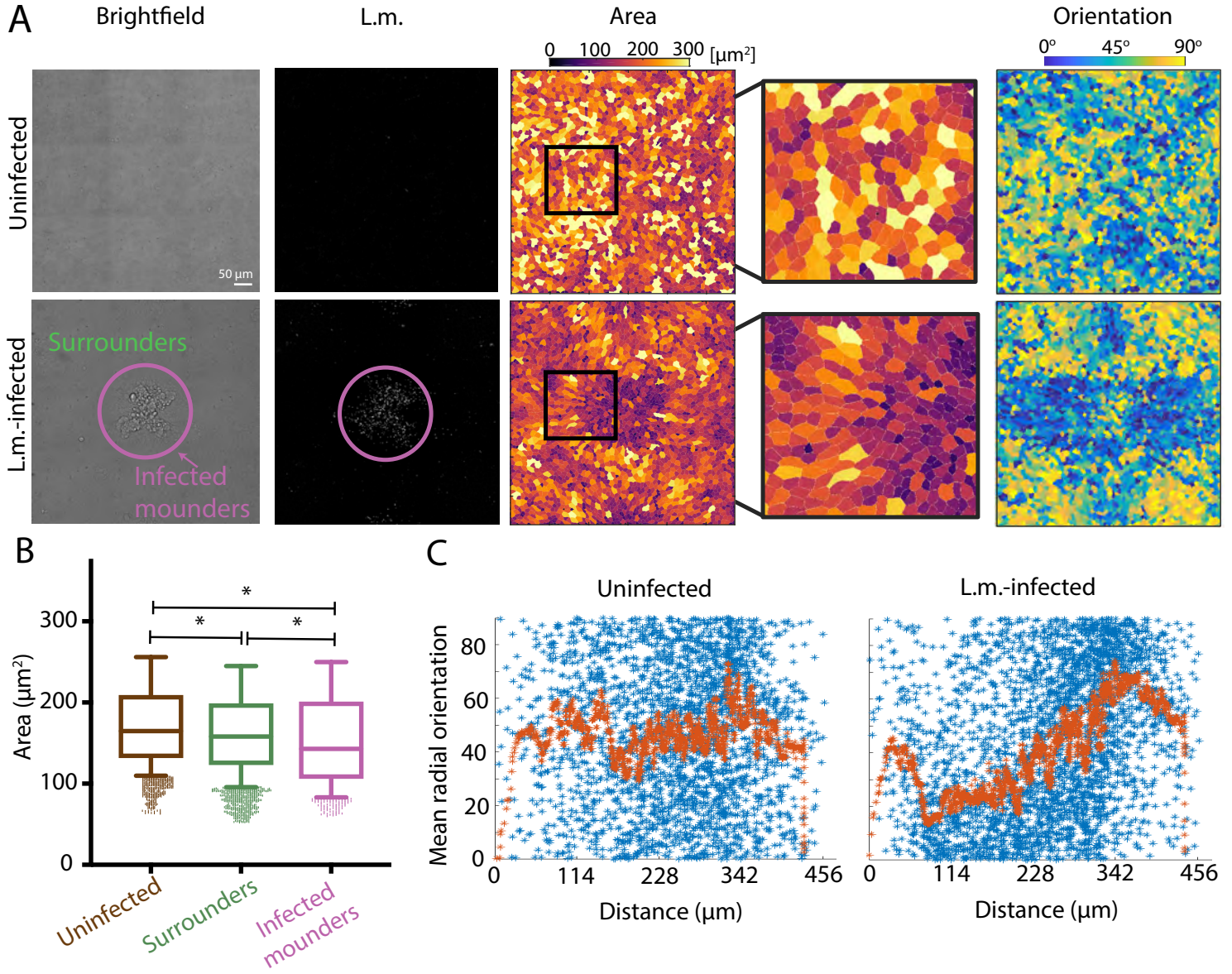
A
Brightfield
L.m.
Area
Orientation
0 100 200 300 [μm²]
0° 45° 90°
Uninfected
L.m.-infected
50 μm
Surrounders
Infected mounders
B
Area (μm²)
300
200
100
0
*
*
*
Uninfected
Surrounders
Infected mounders
C
Uninfected
L.m.-infected
Mean radial orientation
80
60
40
20
0
0 114 228 342 456
Distance (μm)

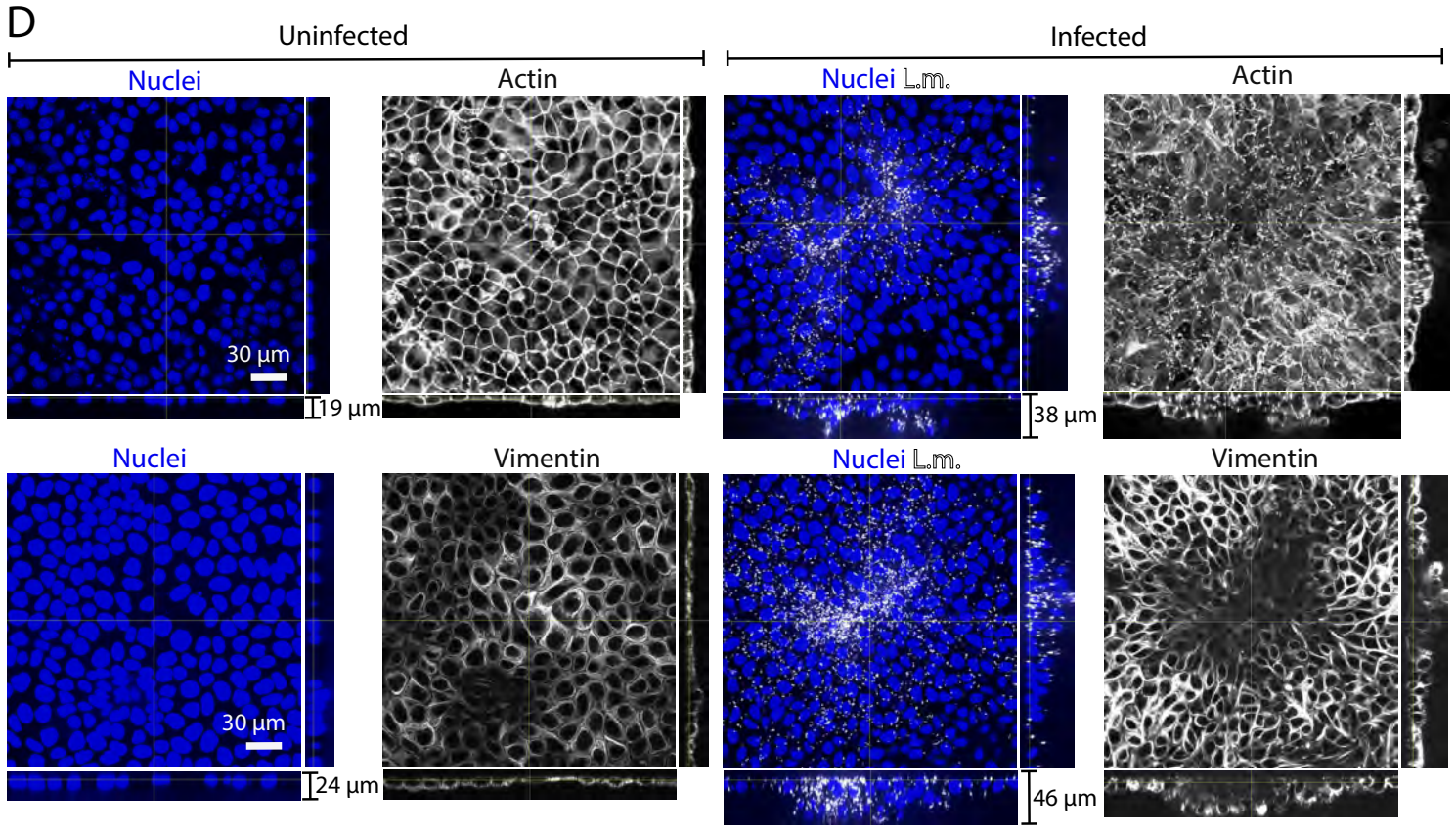
D
Uninfected
Infected
Nuclei
Actin
Nuclei L.m.
Actin
30 μm
19 μm
38 μm
Nuclei
Vimentin
Nuclei L.m.
Vimentin
30 μm
24 μm
46 μm

Figure 3

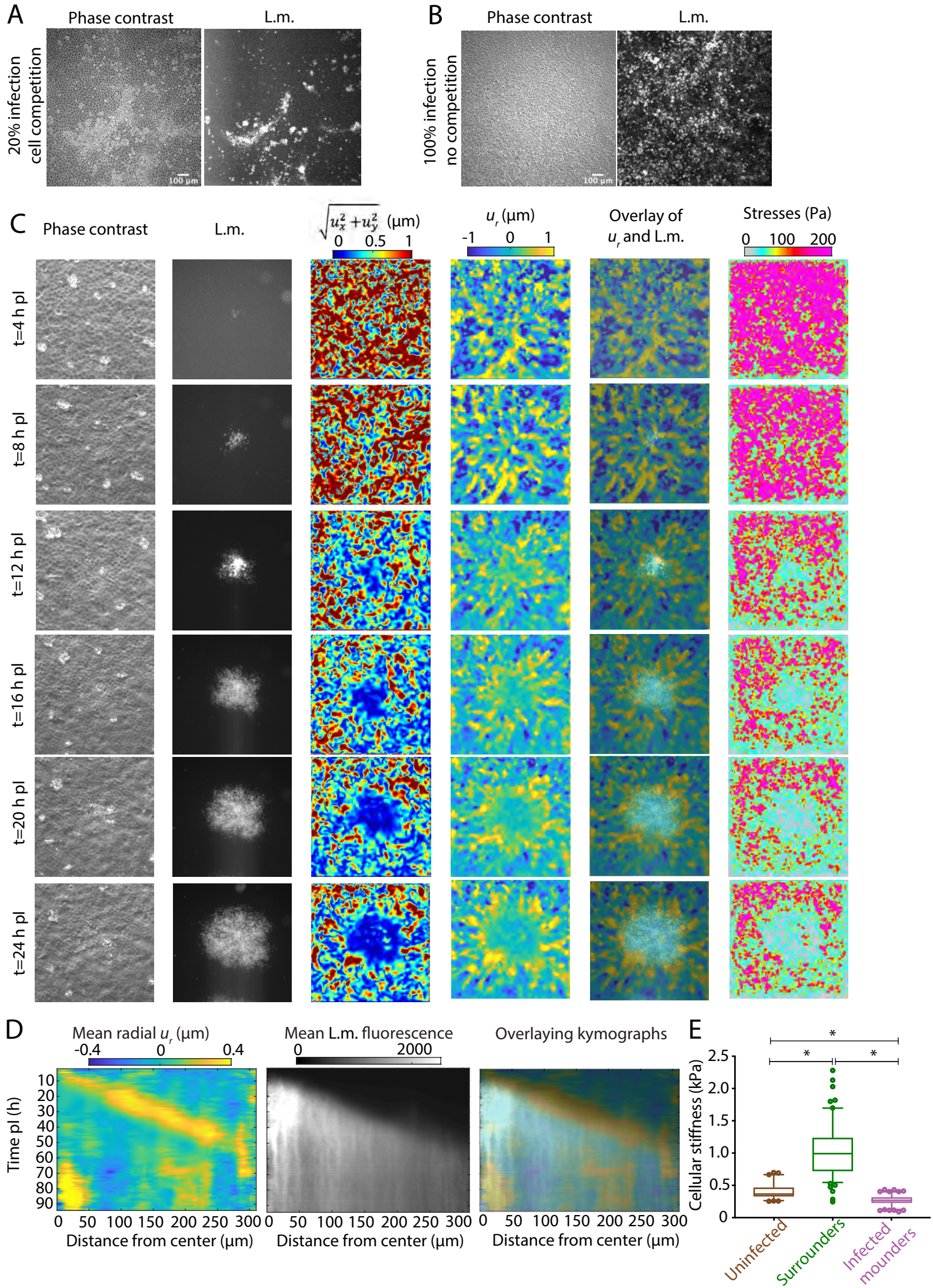
A
Phase contrast
L.m.
20% infection
cell competition
100 µm
B
Phase contrast
L.m.
100% infection
no competition
100 µm
C
Phase contrast
L.m.
$\sqrt{u_x^2+u_y^2}$ (µm)
0 0.5 1
u_r (µm)
-1 0 1
Overlay of
u_r and L.m.
Stresses (Pa)
0 100 200
t=4 h pl
t=8 h pl
t=12 h pl
t=16 h pl
t=20 h pl
t=24 h pl
D
Mean radial u_r (µm)
-0.4 0 0.4
Mean L.m. fluorescence
0 2000
Overlaying kymographs
Time pl (h)
10 20 30 40 50 60 70 80 90
0 50 100 150 200 250 300
Distance from center (µm)
E
Cellular stiffness (kPa)
0 0.5 1.0 1.5 2.0 2.5
*
Uninfected
Surrounders
Infected mounders

Figure 4

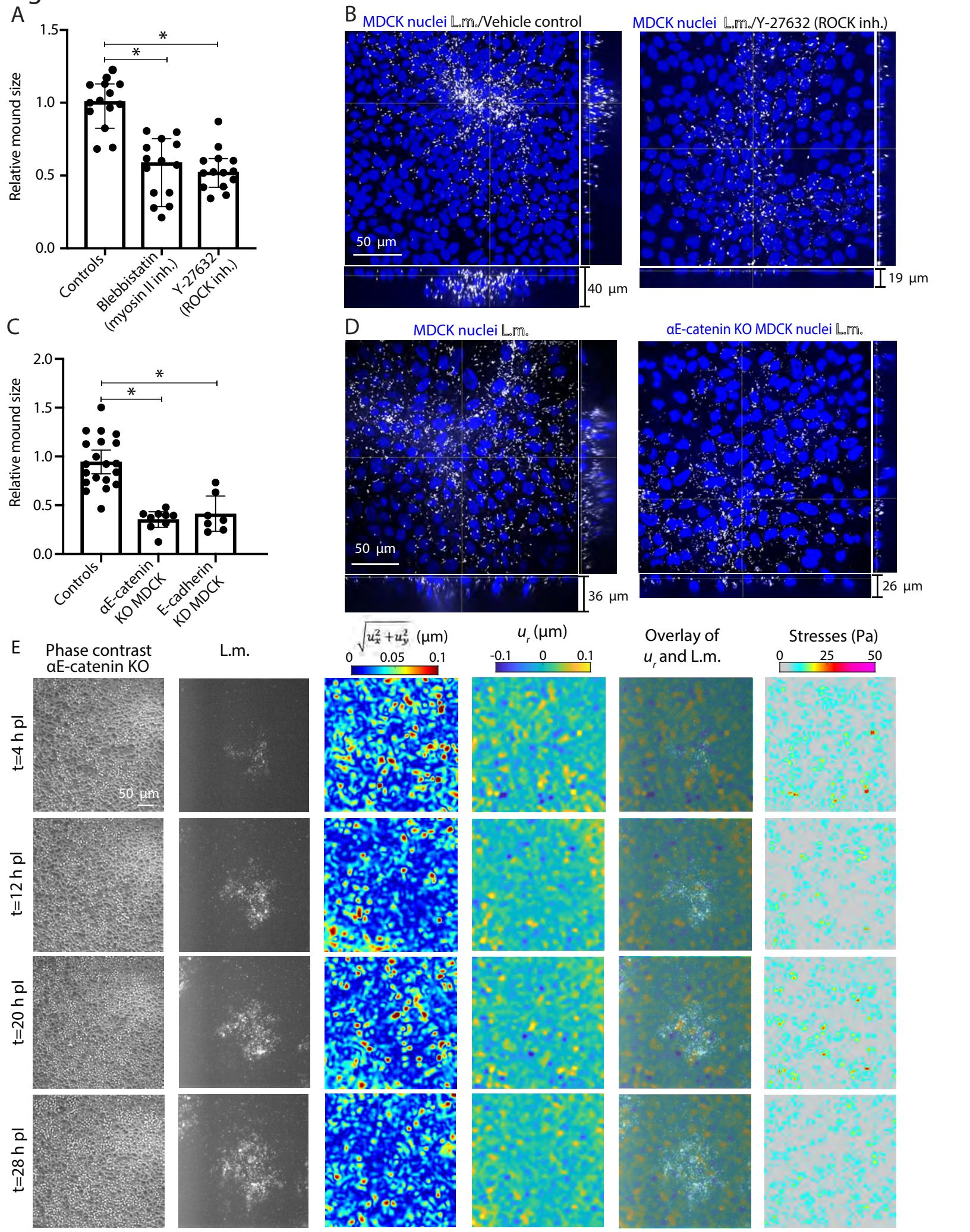
A
Relative mound size
1.5
1.0
0.5
0.0
*
*
Controls
Blebbistatin (myosin II inh.)
Y-27632 (ROCK inh.)
B
MDCK nuclei L.m./Vehicle control
MDCK nuclei L.m./Y-27632 (ROCK inh.)
50 µm
40 µm
19 µm
C
Relative mound size
2.0
1.5
1.0
0.5
0.0
*
*
Controls
αE-catenin KO MDCK
E-cadherin KD MDCK
D
MDCK nuclei L.m.
αE-catenin KO MDCK nuclei L.m.
50 µm
36 µm
26 µm
E
Phase contrast αE-catenin KO
L.m.
$\sqrt{u_x^2+u_y^2}$ (µm)
0 0.05 0.1
u_r (µm)
-0.1 0 0.1
Overlay of u_r and L.m.
Stresses (Pa)
0 25 50
t=4 h pl
t=12 h pl
t=20 h pl
t=28 h pl
50 µm

Figure 5

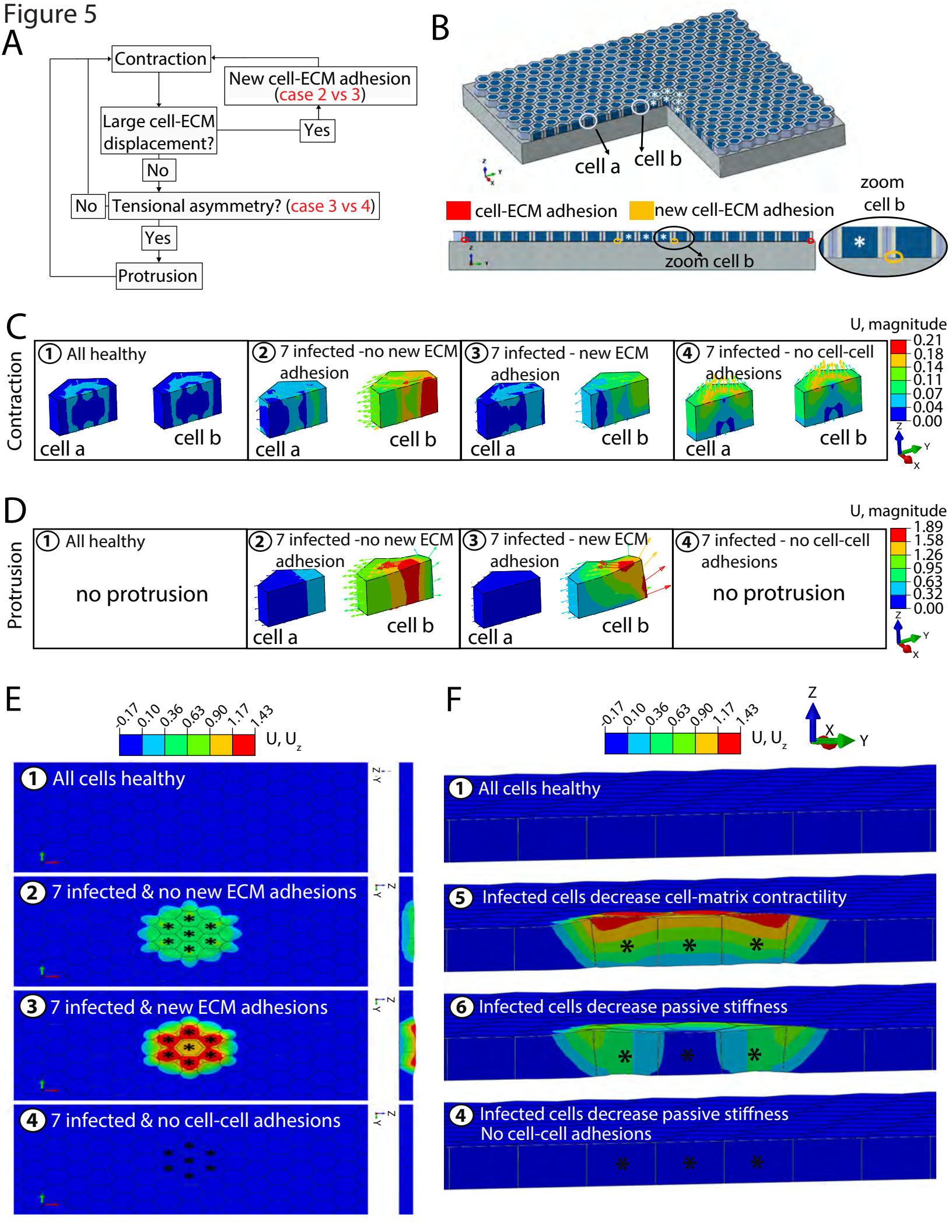
A
Contraction
New cell-ECM adhesion (case 2 vs 3)
Large cell-ECM displacement?
Yes
No
No
Tensional asymmetry? (case 3 vs 4)
Yes
Protrusion
B
cell a
cell b
zoom cell b
cell-ECM adhesion
new cell-ECM adhesion
zoom cell b
C
Contraction
U, magnitude
0.21
0.18
0.14
0.11
0.07
0.04
0.00
1 All healthy
cell a
cell b
2 7 infected -no new ECM adhesion
cell a
cell b
3 7 infected - new ECM adhesion
cell a
cell b
4 7 infected - no cell-cell adhesions
cell a
cell b
D
Protrusion
U, magnitude
1.89
1.58
1.26
0.95
0.63
0.32
0.00
1 All healthy
no protrusion
2 7 infected -no new ECM adhesion
cell a
cell b
3 7 infected - new ECM adhesion
cell a
cell b
4 7 infected - no cell-cell adhesions
no protrusion
E
-0.17
0.10
0.36
0.63
0.90
1.17
1.43
U, U_z
1 All cells healthy
2 7 infected & no new ECM adhesions
3 7 infected & new ECM adhesions
4 7 infected & no cell-cell adhesions
F
-0.17
0.10
0.36
0.63
0.90
1.17
1.43
U, U_z
Z
X
Y
1 All cells healthy
5 Infected cells decrease cell-matrix contractility
6 Infected cells decrease passive stiffness
4 Infected cells decrease passive stiffness
No cell-cell adhesions

Figure 6

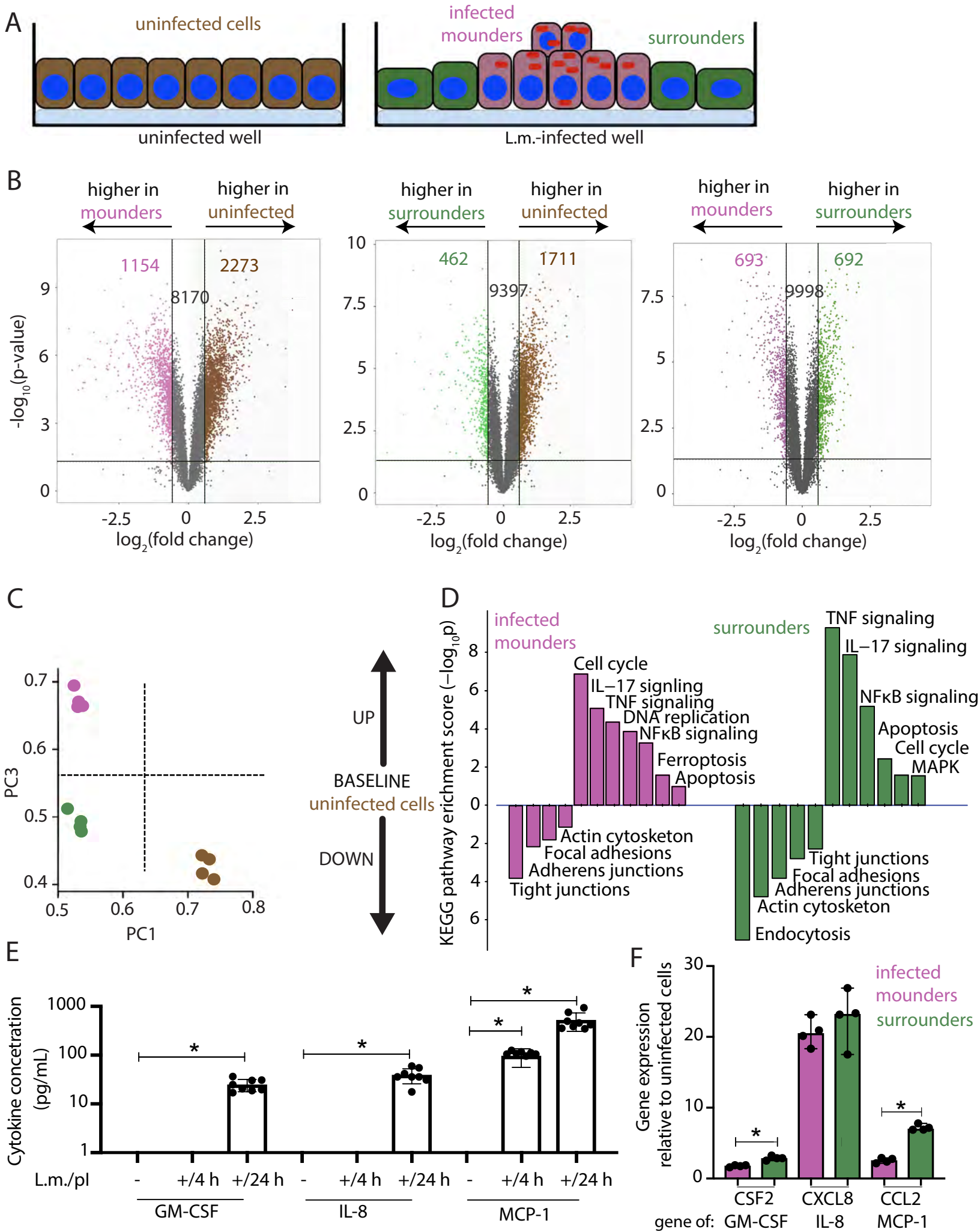
A
uninfected cells
uninfected well
infected mounders
surrounders
L.m.-infected well
B
higher in mounders
higher in uninfected
1154
2273
8170
-log10(p-value)
log2(fold change)
higher in surrounders
higher in uninfected
462
1711
9397
higher in mounders
higher in surrounders
693
692
9998
C
PC3
PC1
UP
BASELINE
uninfected cells
DOWN
D
infected mounders
surrounders
KEGG pathway enrichment score (−log10p)
Cell cycle
IL−17 signling
TNF signaling
DNA replication
NFκB signaling
Ferroptosis
Apoptosis
Actin cytosketon
Focal adhesions
Adherens junctions
Tight junctions
TNF signaling
IL−17 signaling
NFκB signaling
Apoptosis
Cell cycle
MAPK
Tight junctions
Focal adhesions
Adherens junctions
Actin cytosketon
Endocytosis
E
Cytokine concetration (pg/mL)
L.m./pl
-
+/4 h
+/24 h
GM-CSF
IL-8
MCP-1
F
Gene expression relative to uninfected cells
infected mounders
surrounders
CSF2
CXCL8
CCL2
gene of:
GM-CSF
IL-8
MCP-1

Figure 7

A

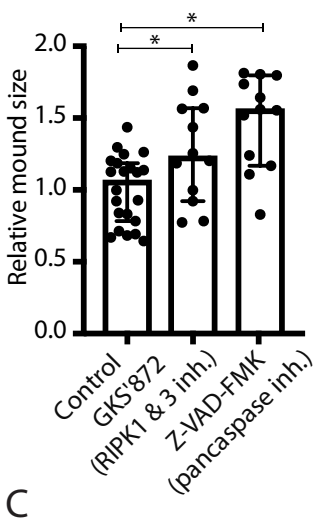

B

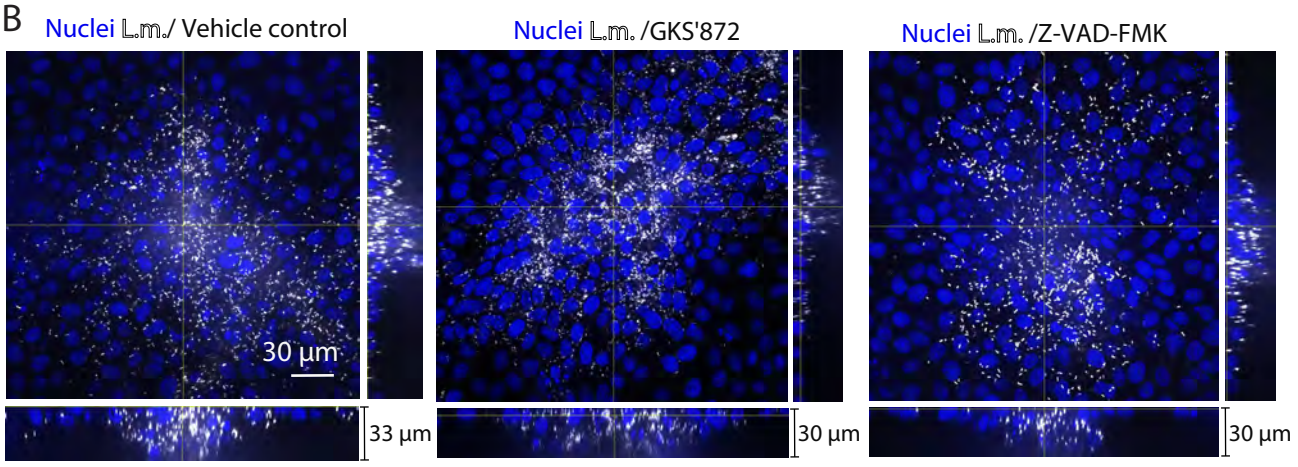

C

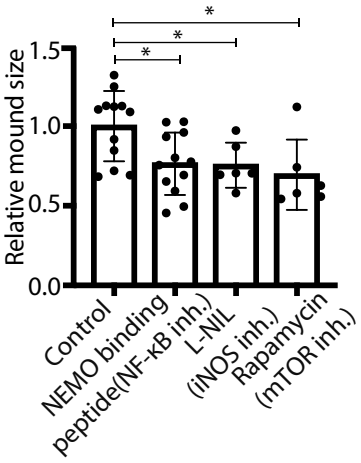

D

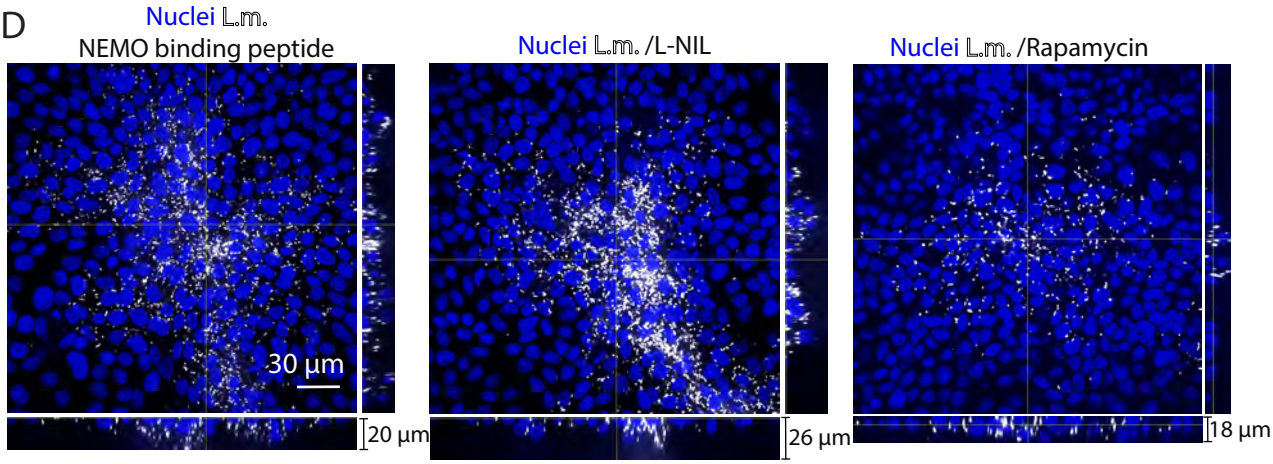

E

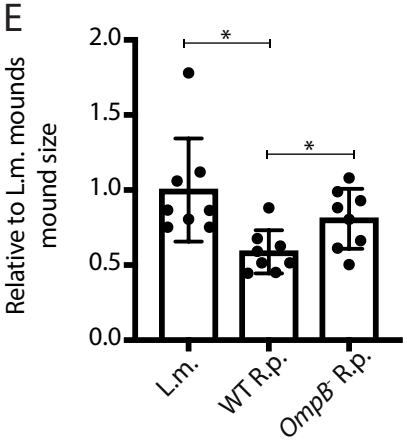

F

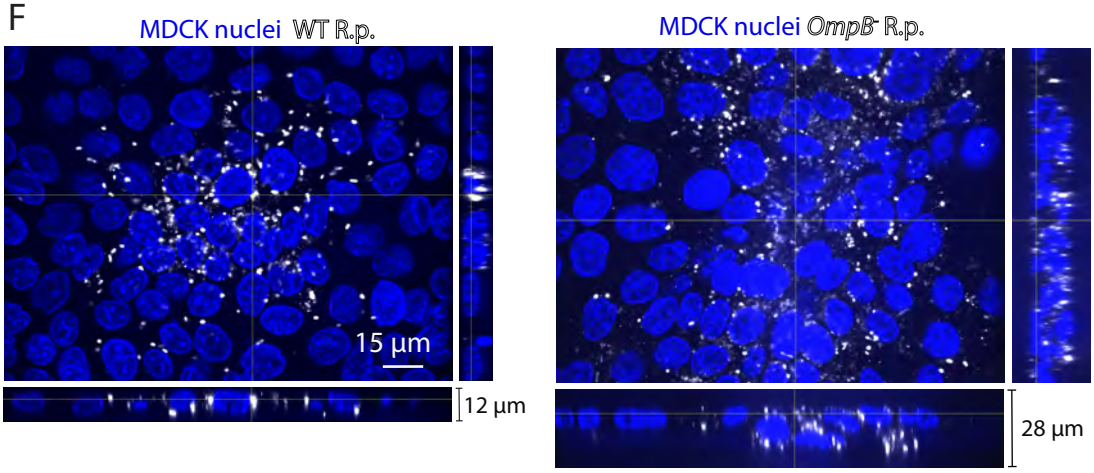

Supplemental Figure 1

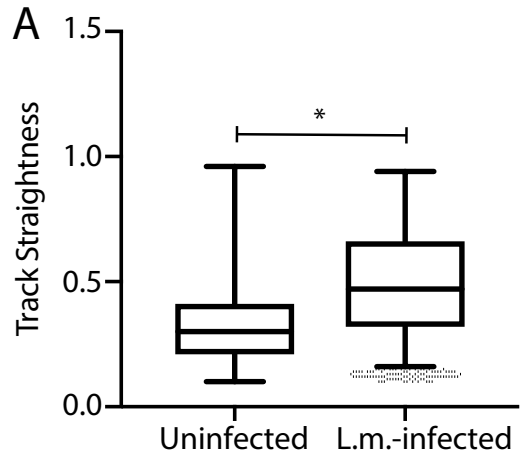

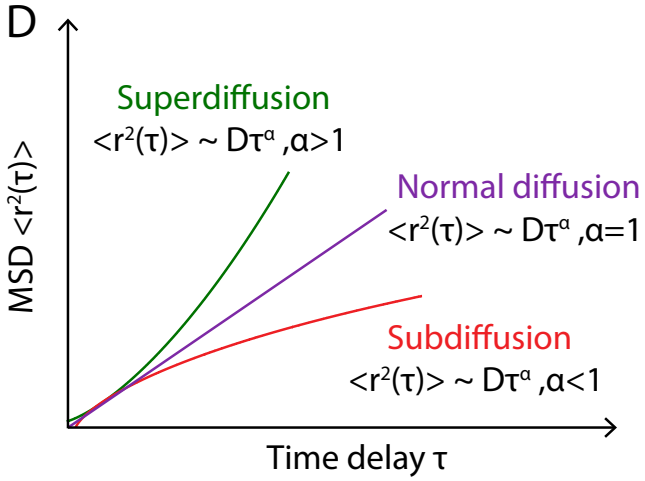

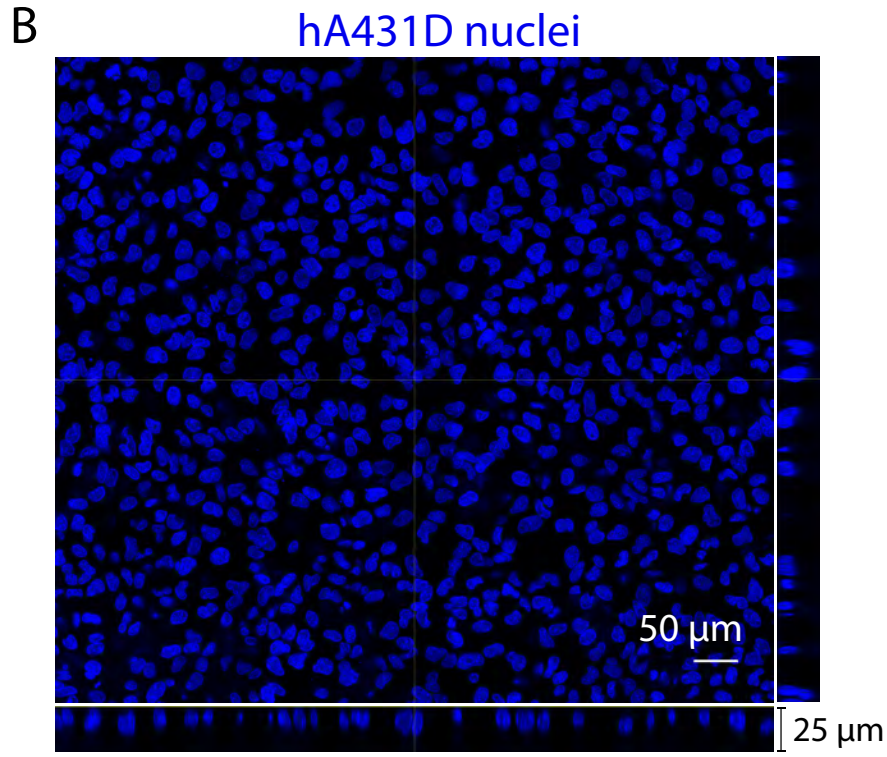

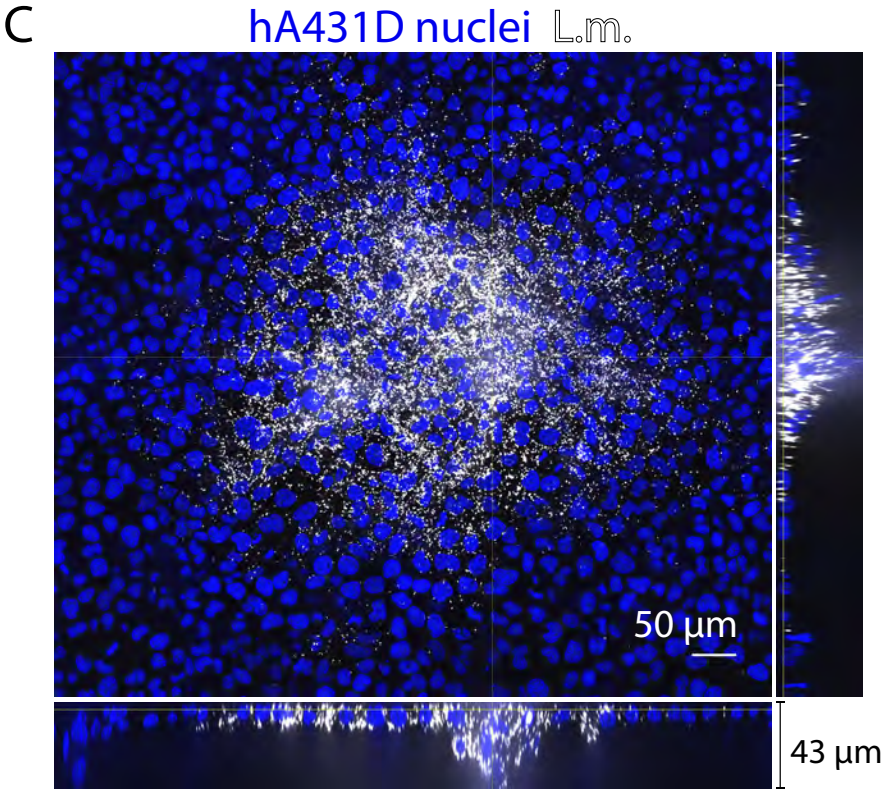

Supplemental Figure 2

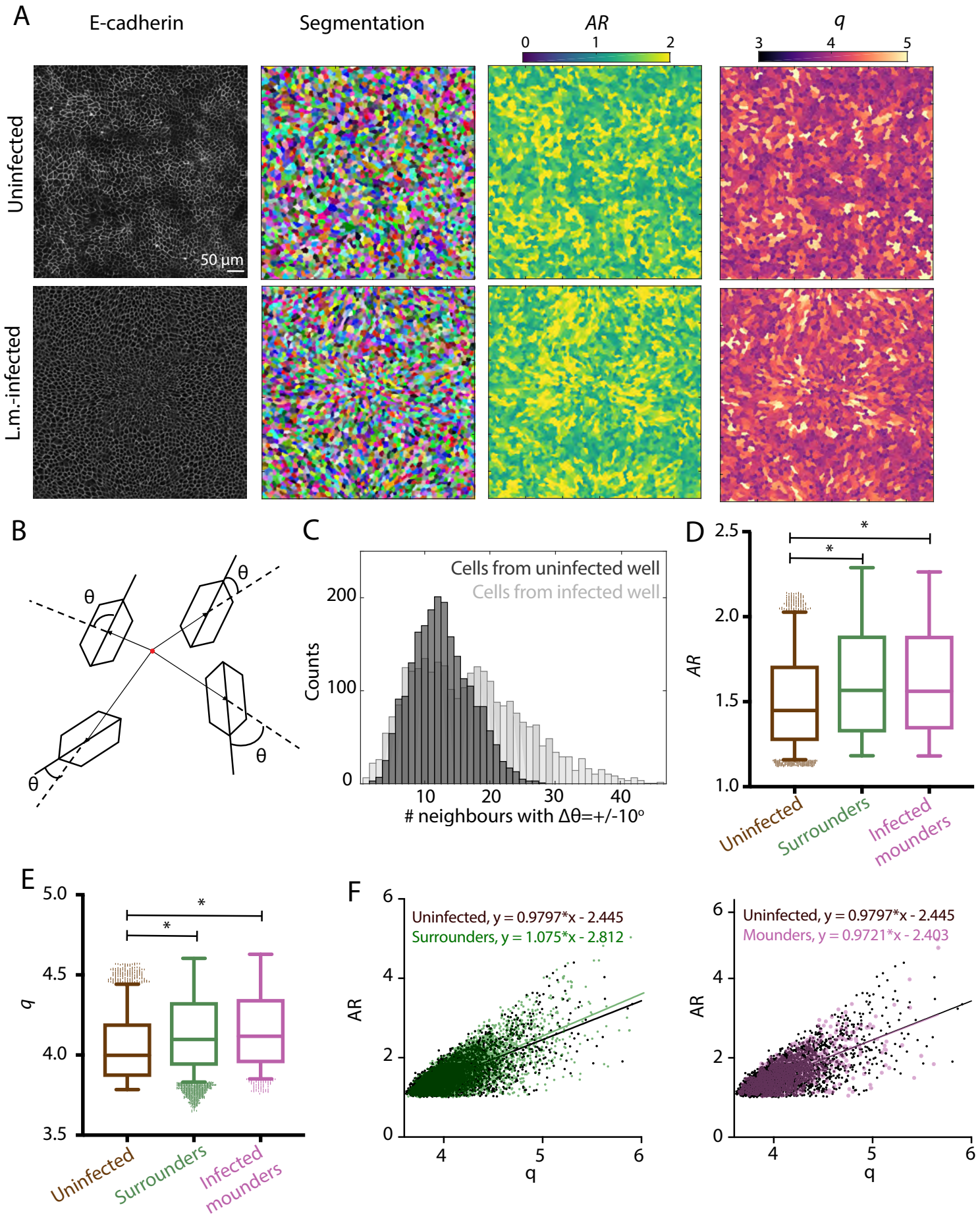

Supplemental Figure 3

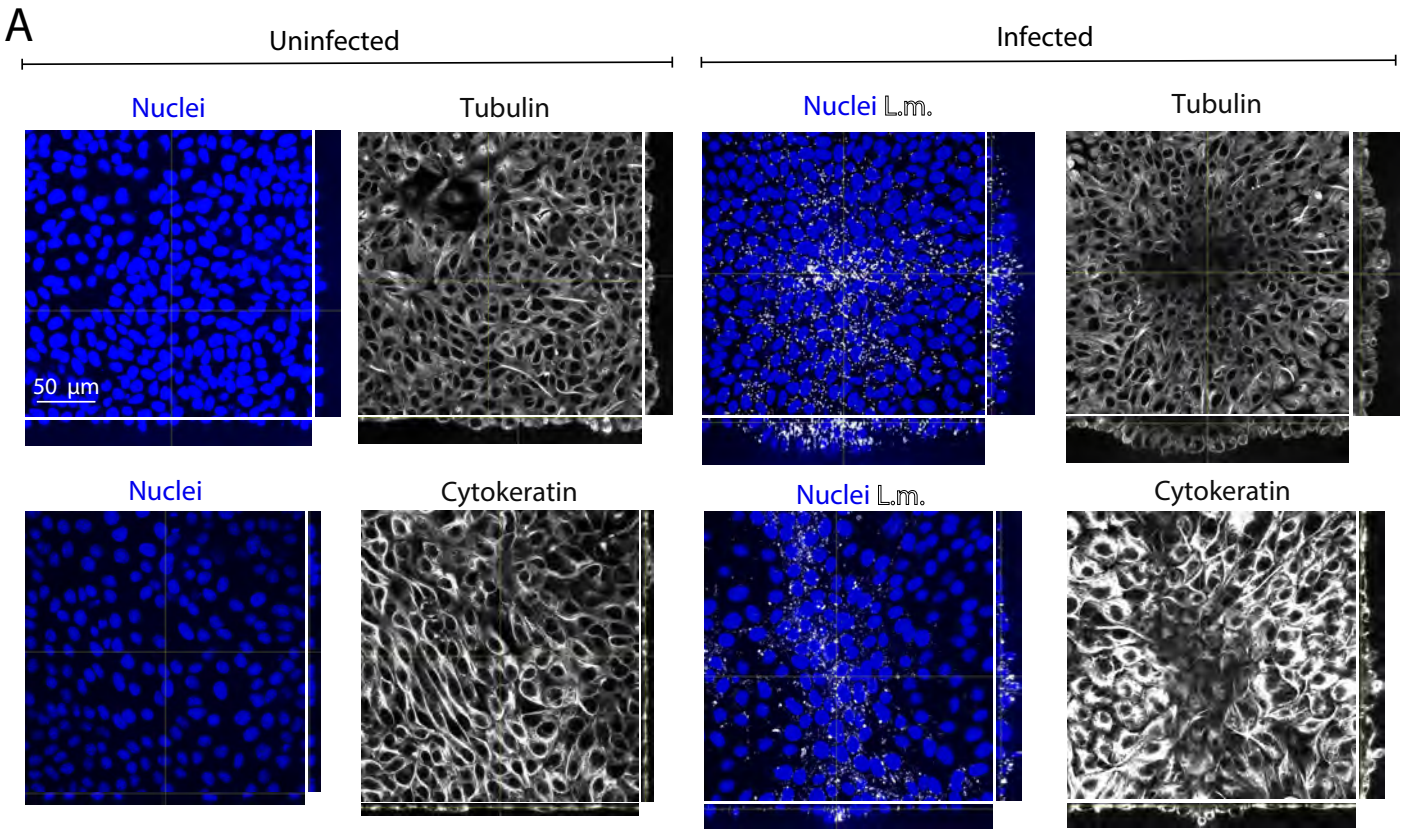

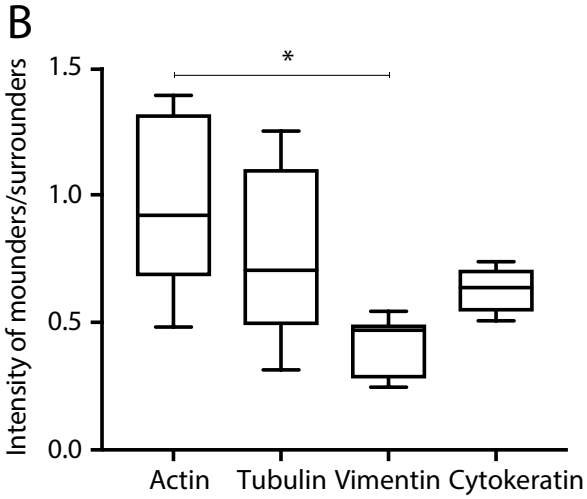

Supplemental Figure 4

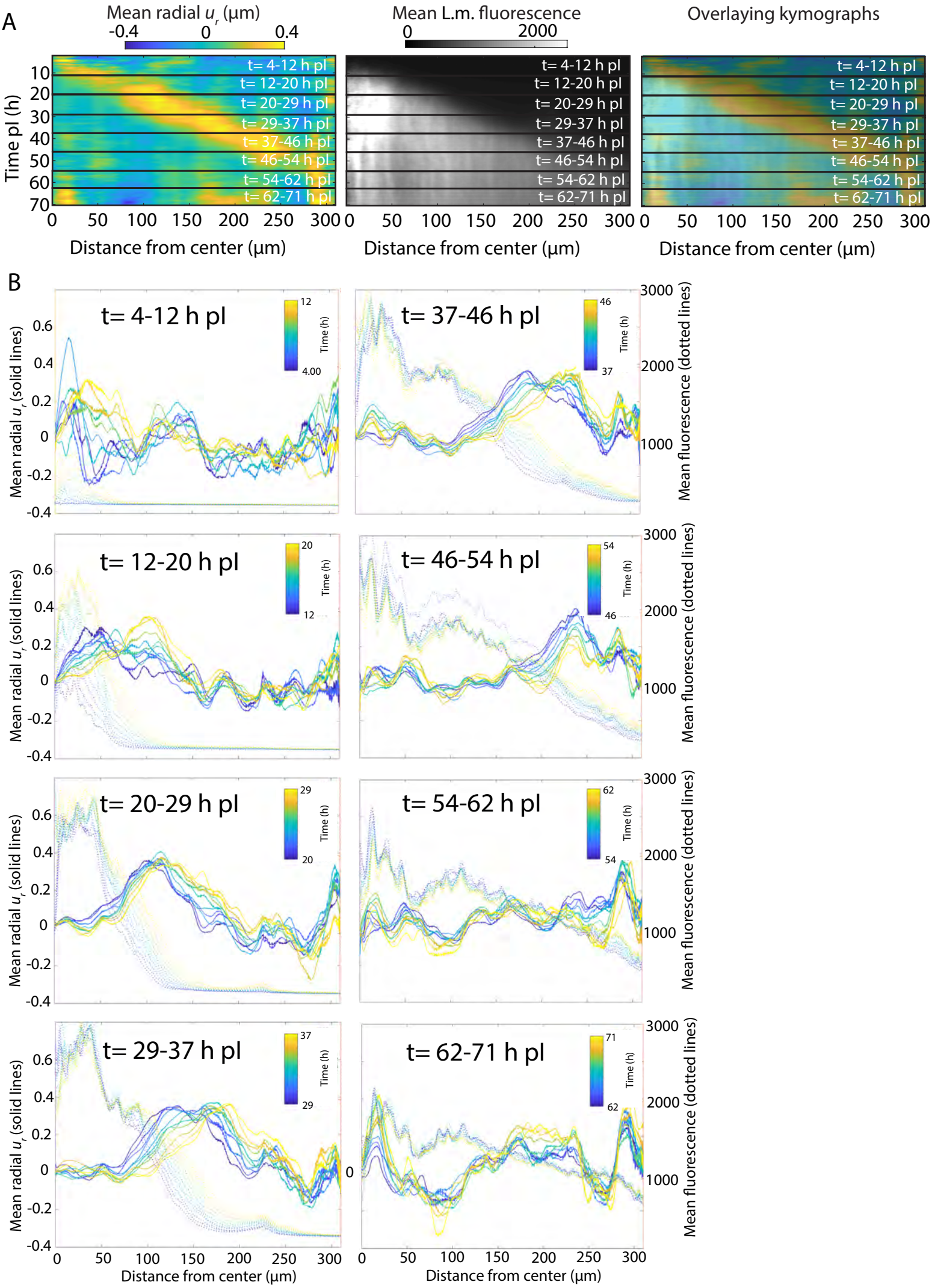

Supplemental Figure 5

A

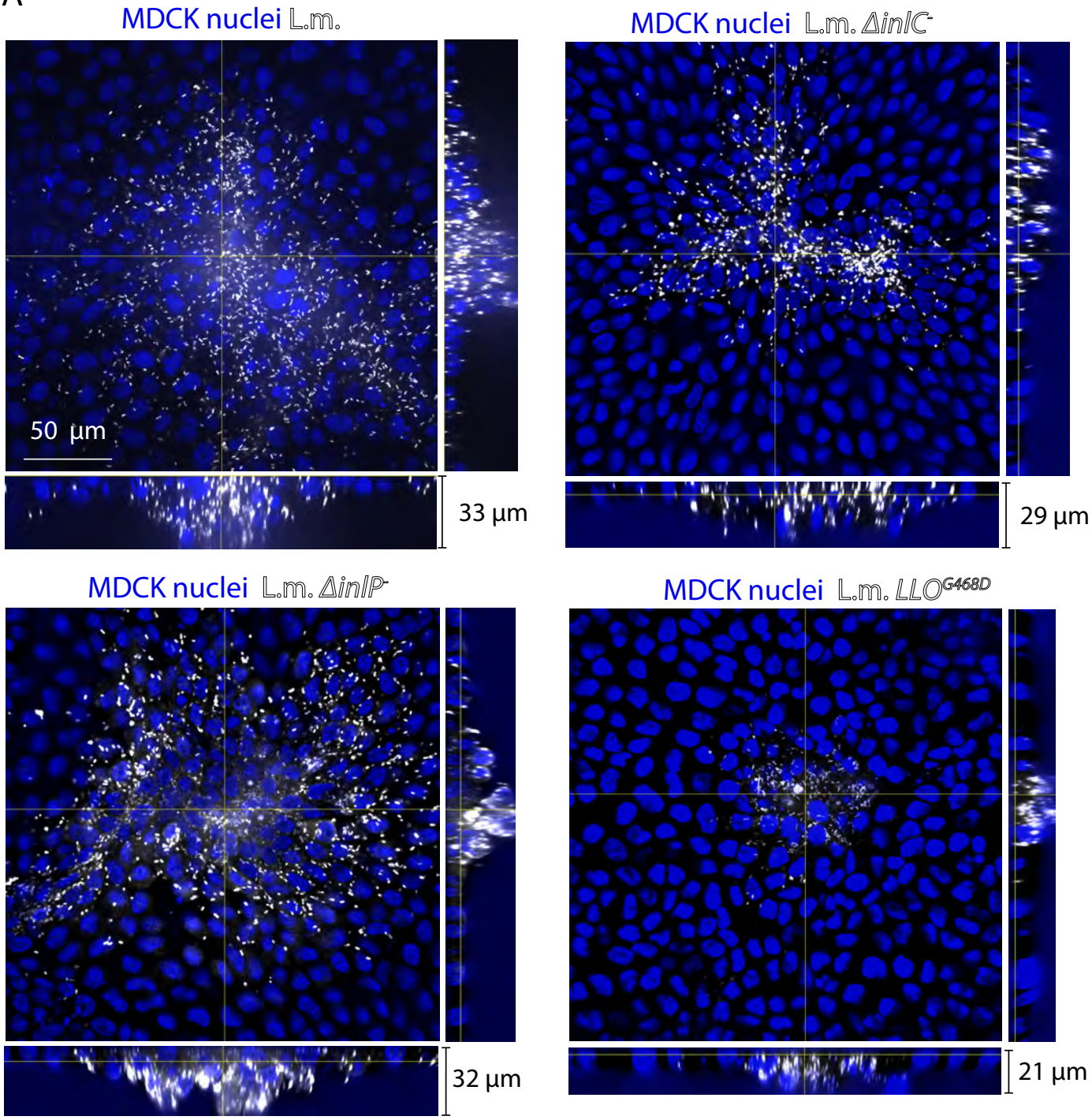

B

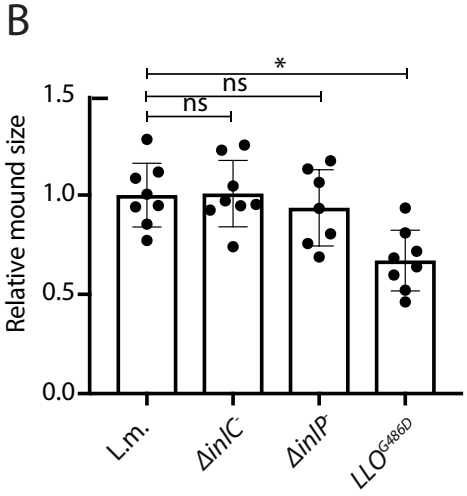

C

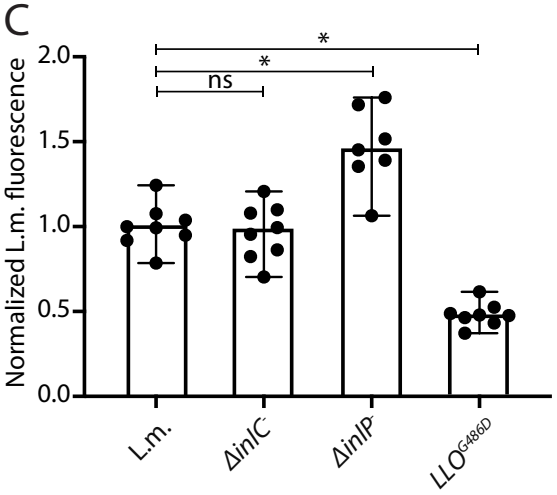

Supplemental Figure 6

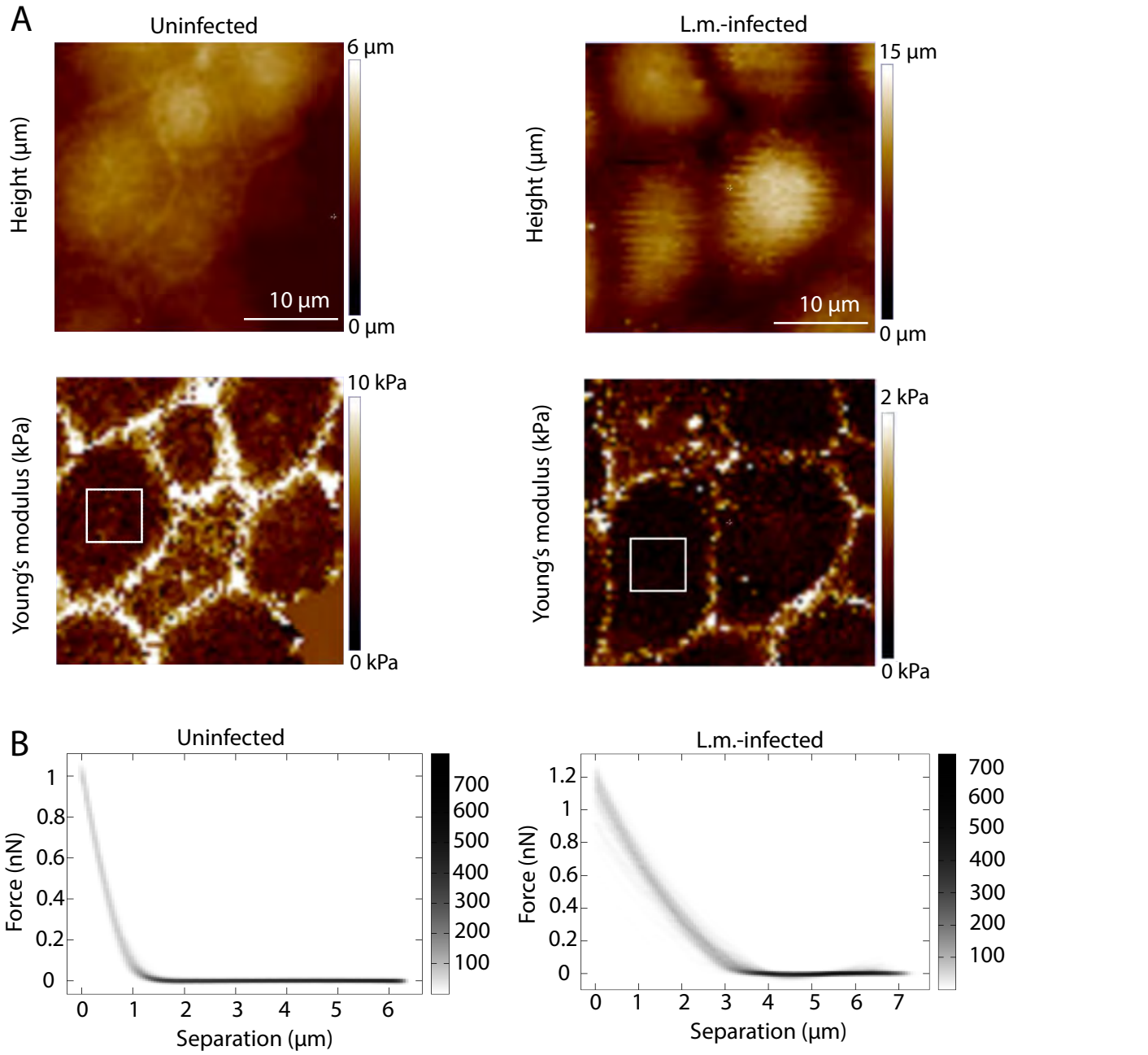

Supplemental Figure 7

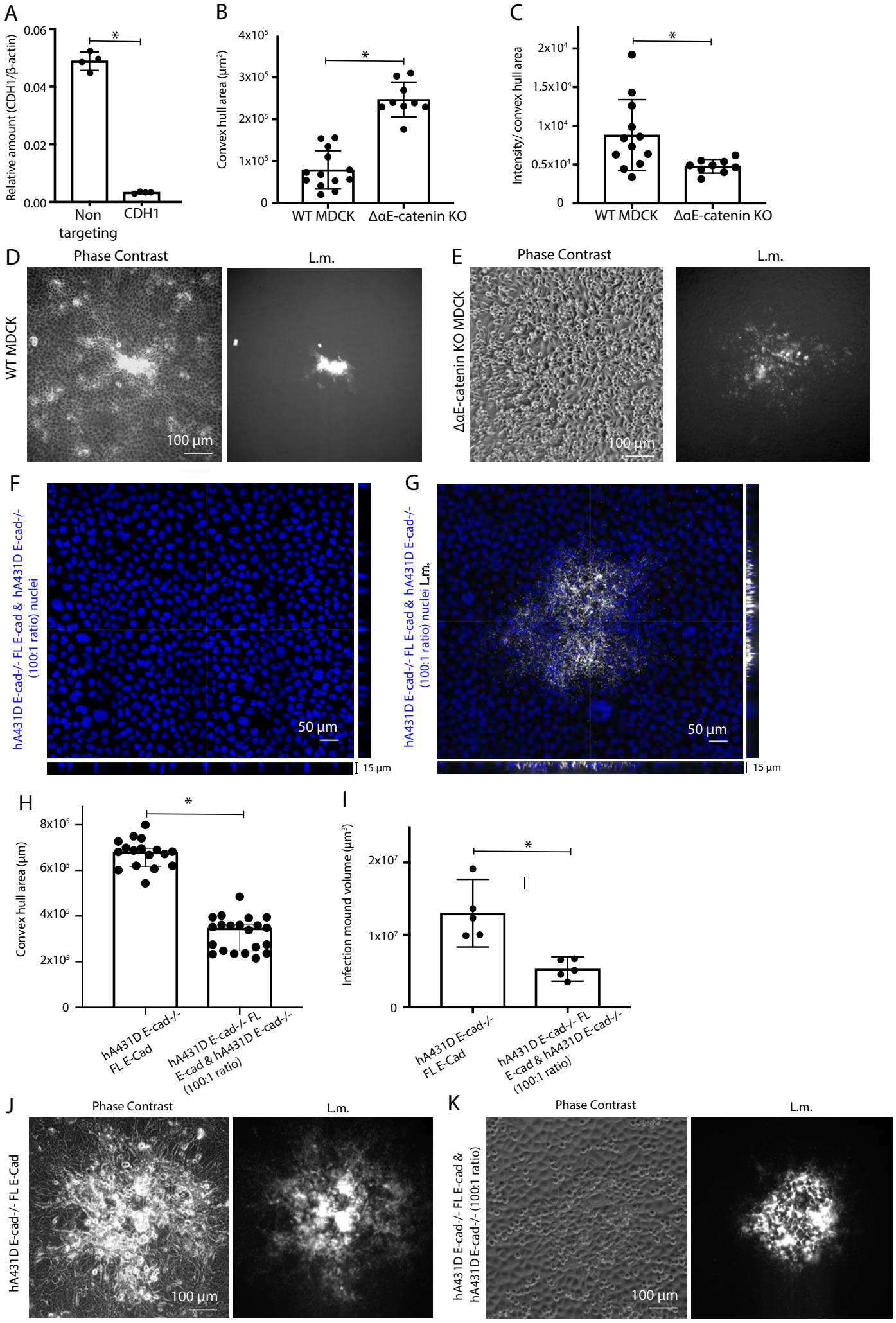

Supplemental Figure 8

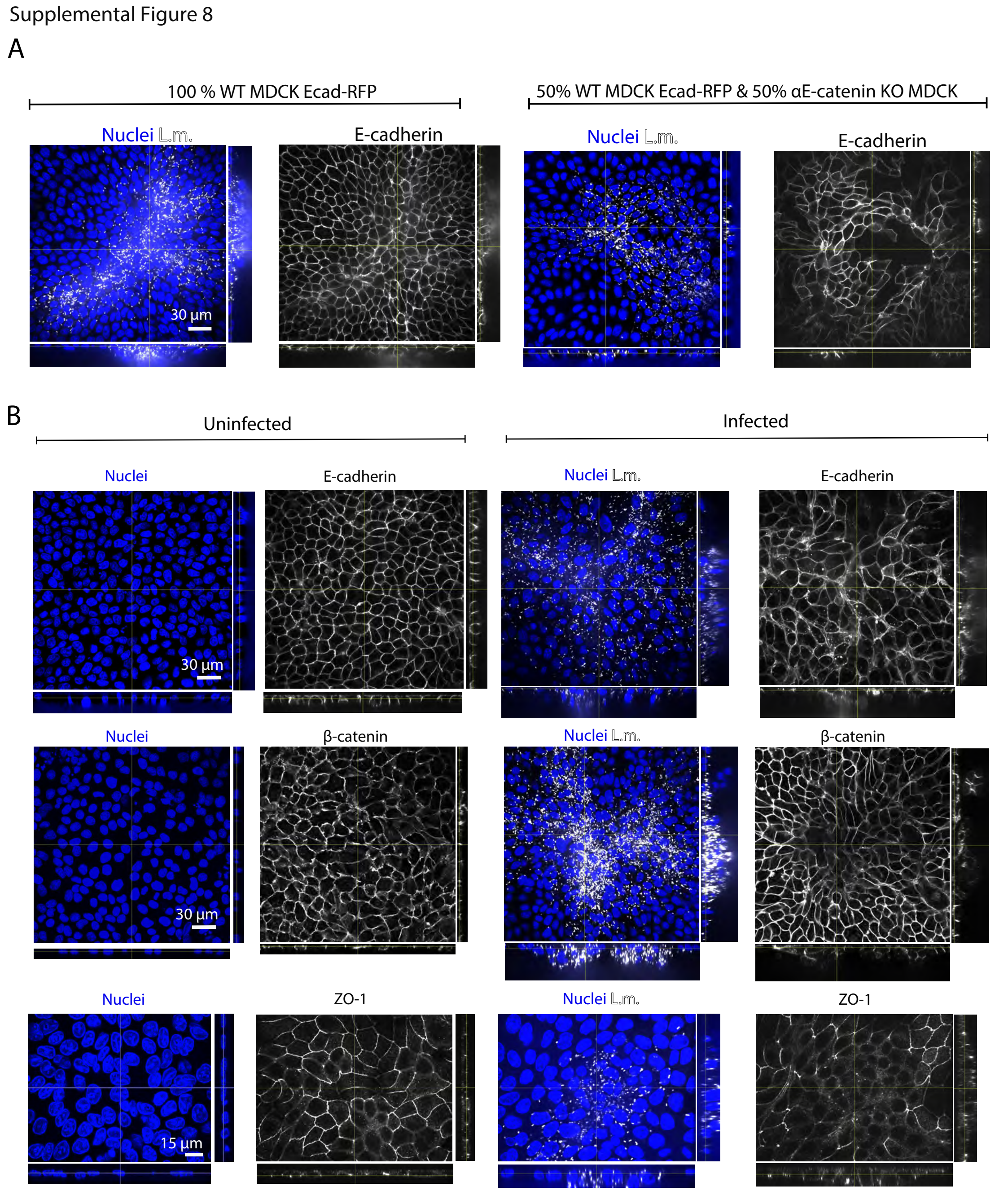

Supplemental Figure S9

A

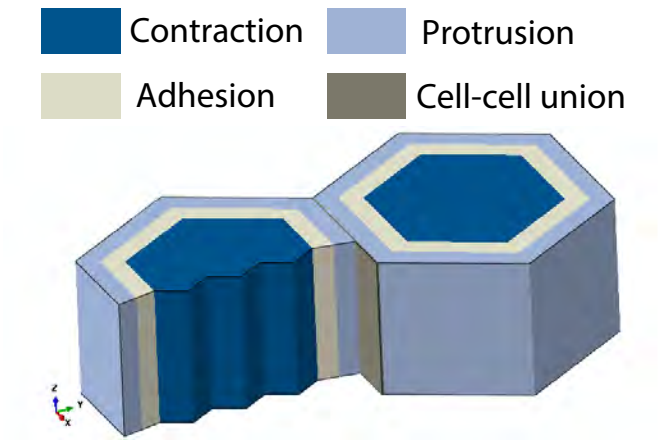

B

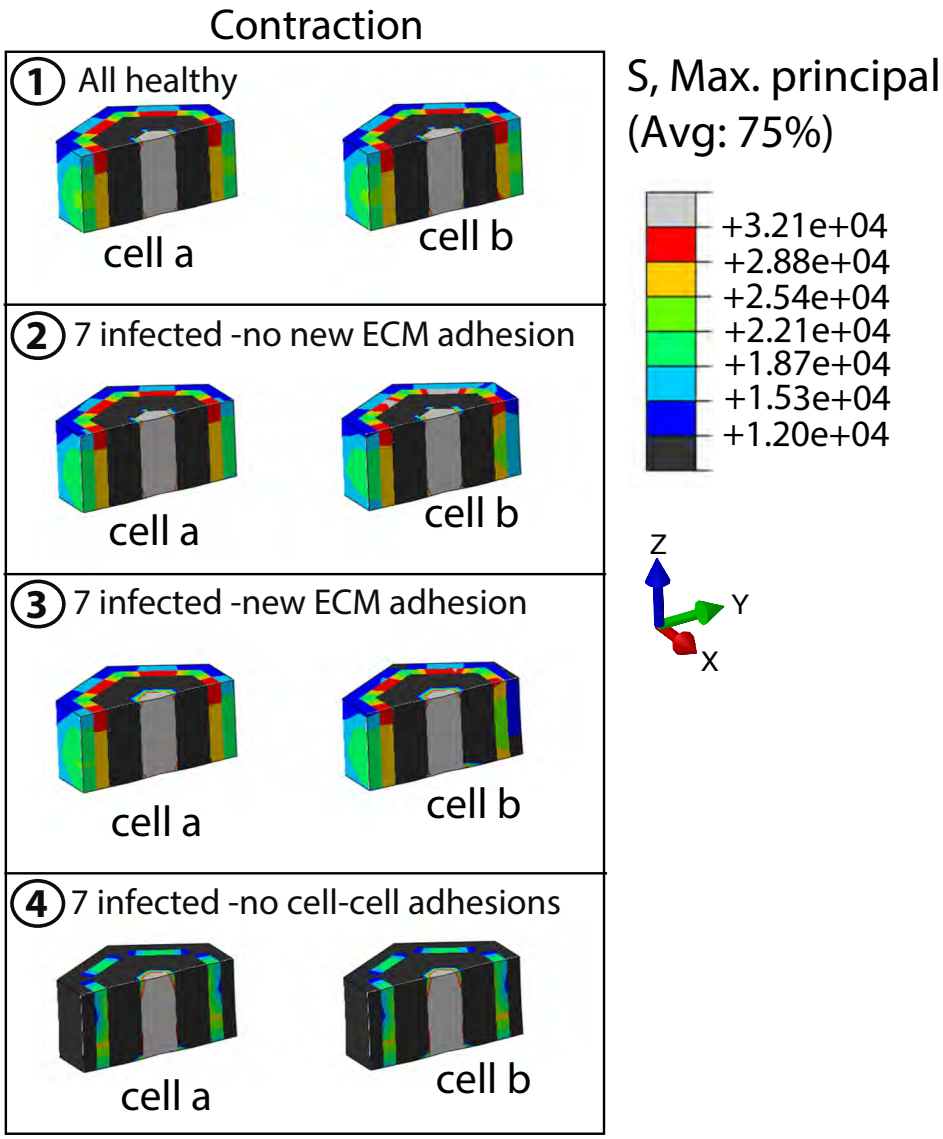

C

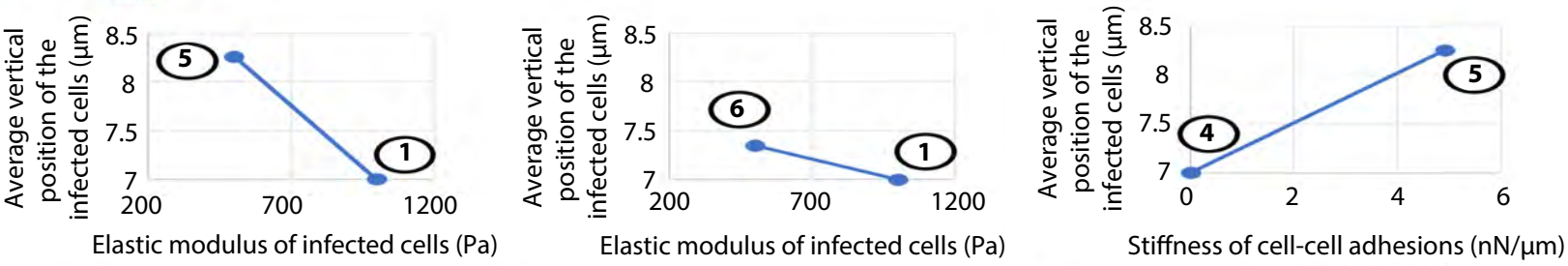

Supplemental Figure 10

A Uninfected vs Infected mounders

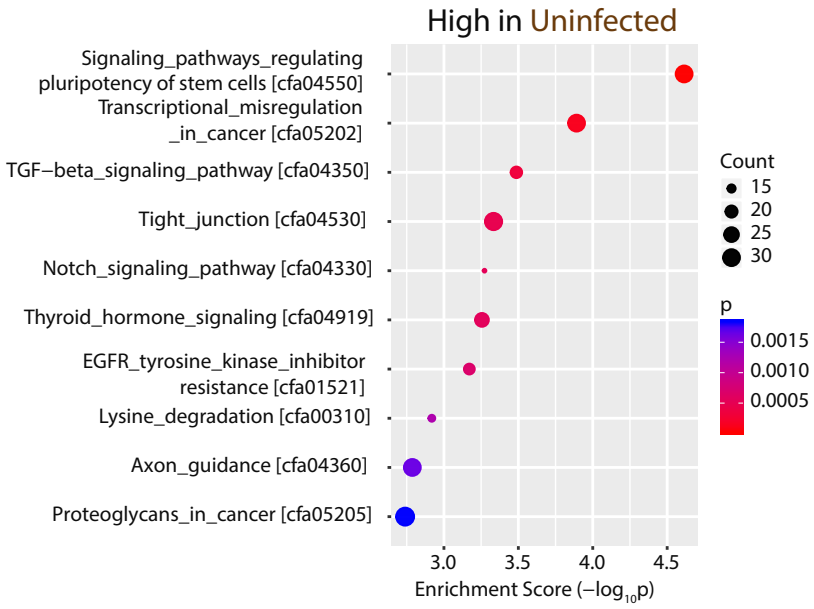

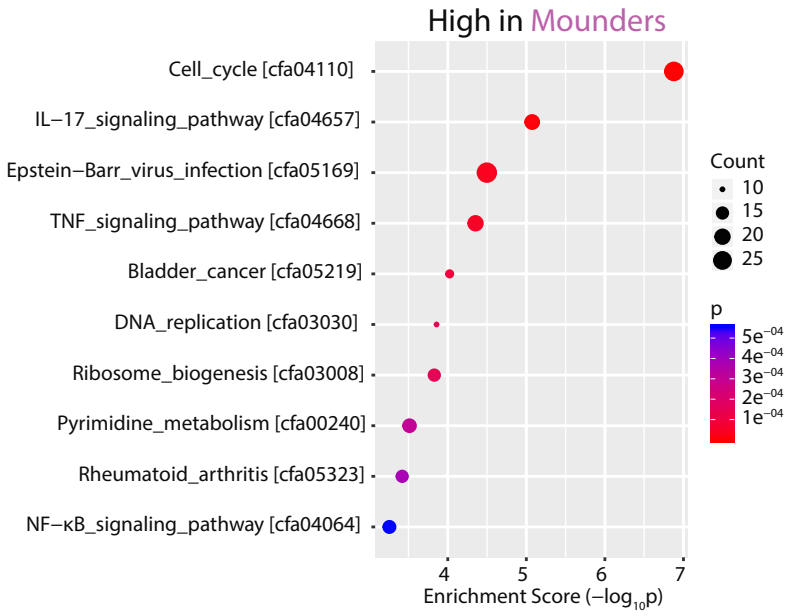

B Uninfected vs Surrounders

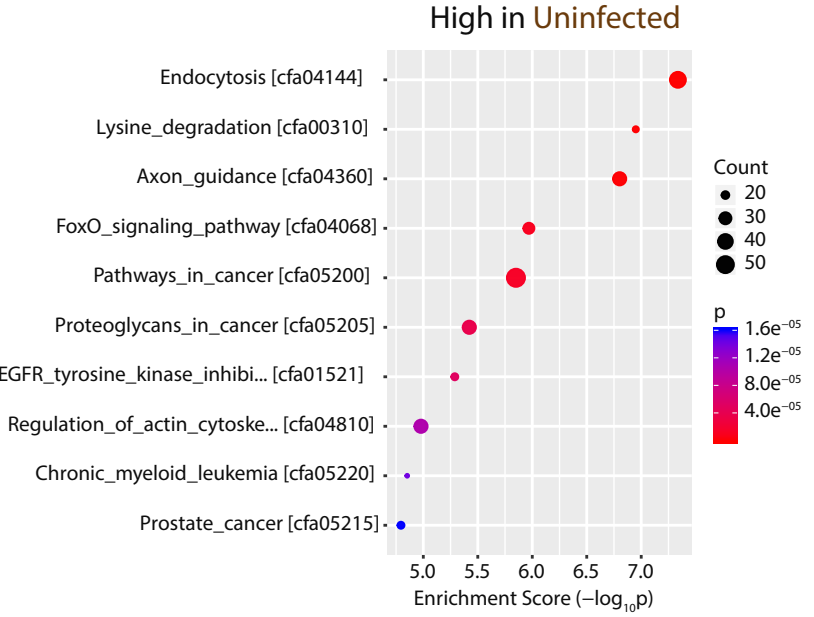

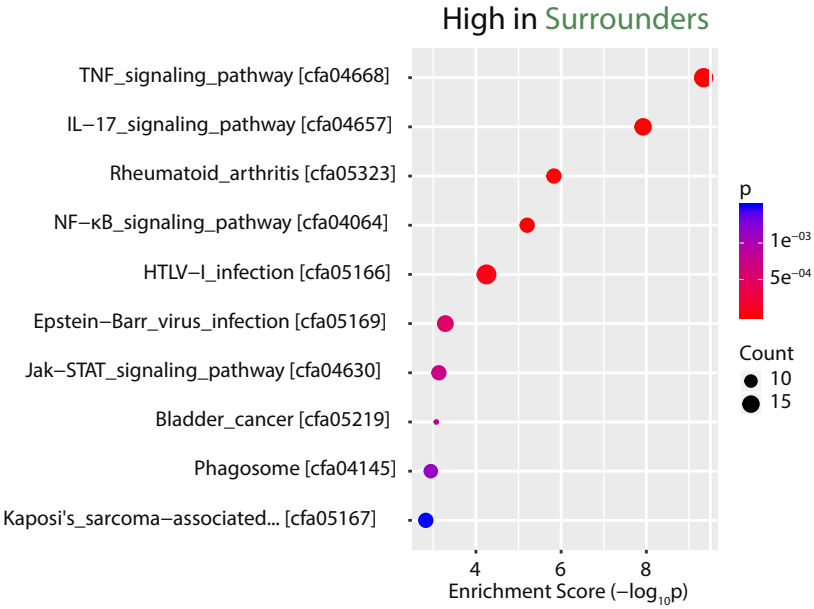

C Mounders vs Surrounders

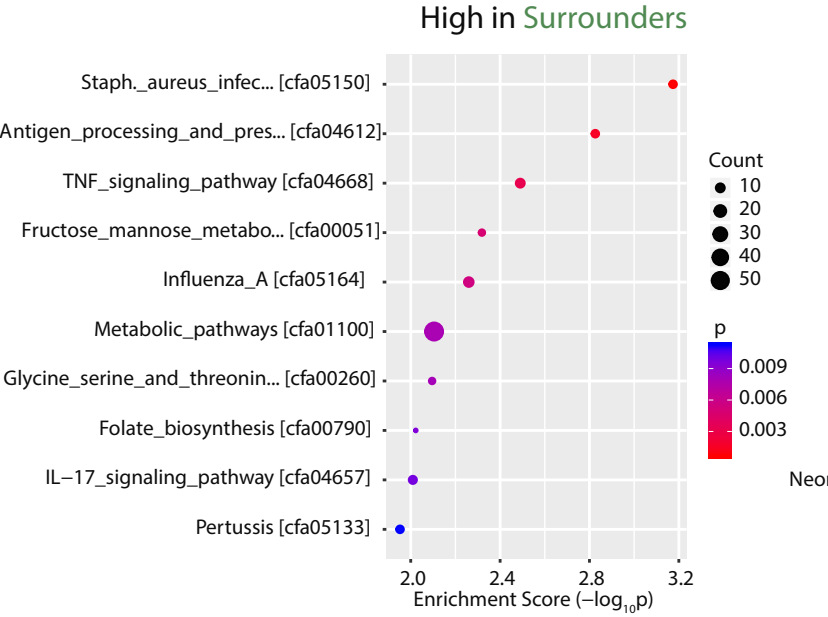

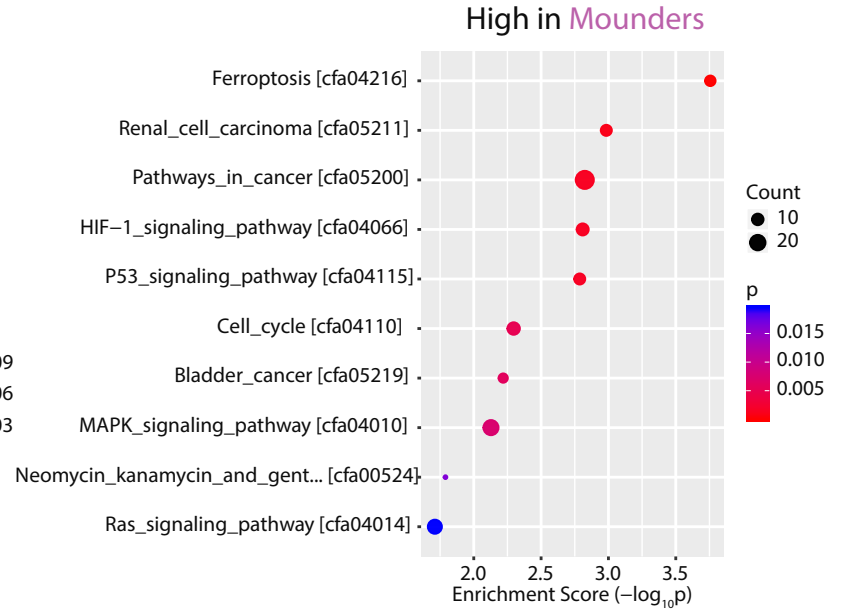

Supplemental Figure 11

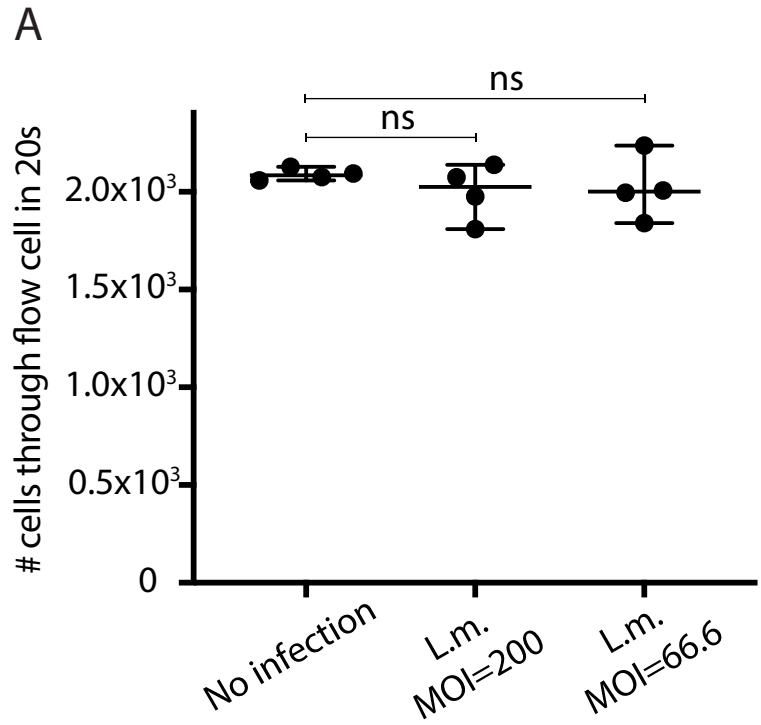

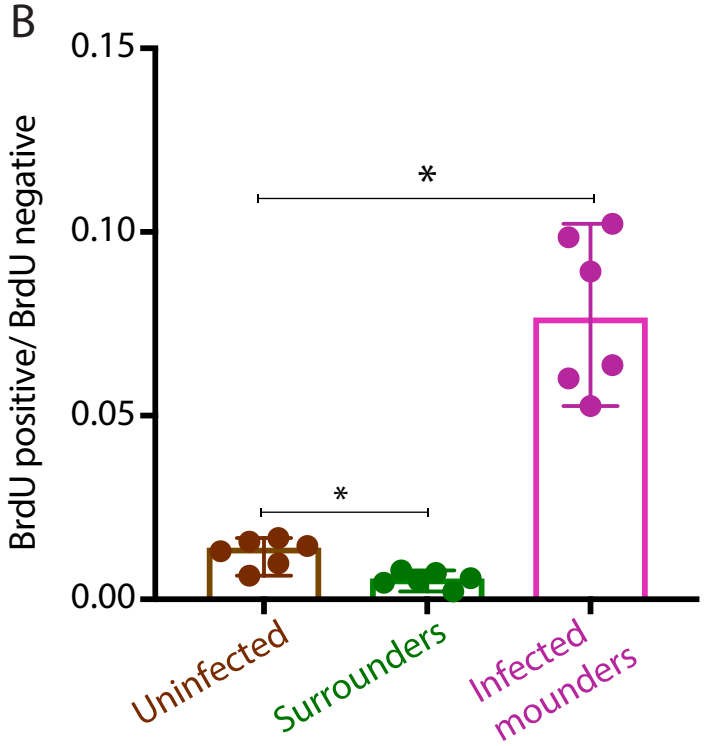

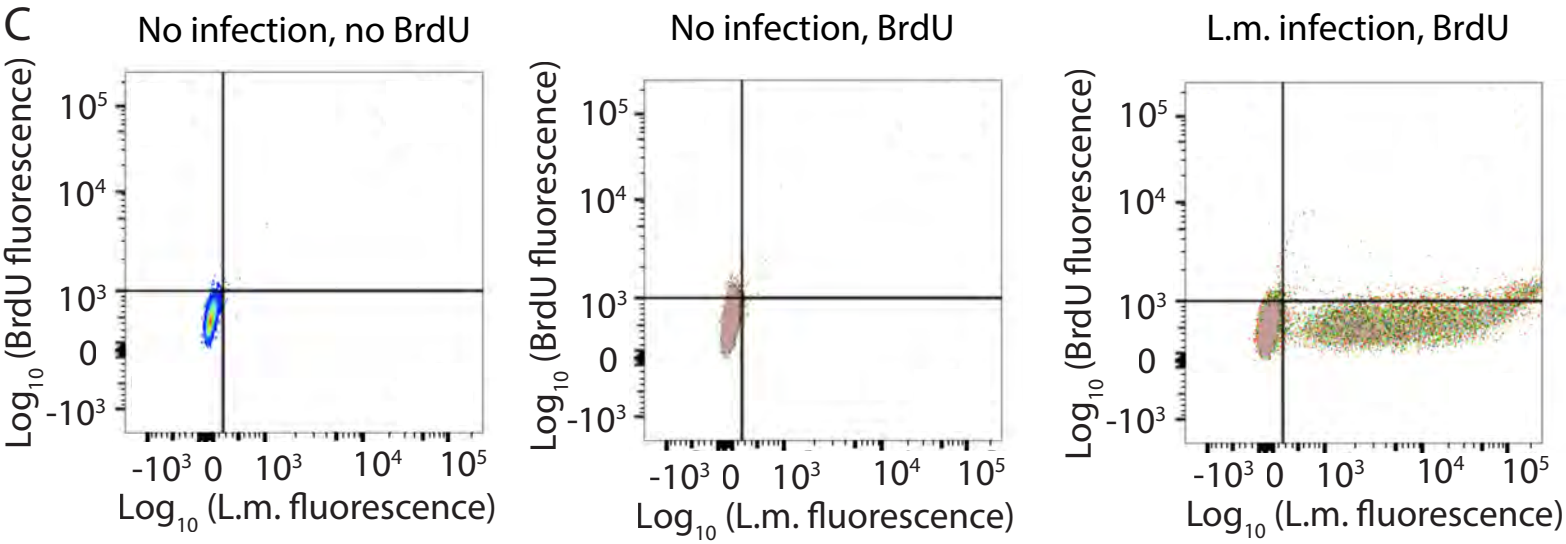

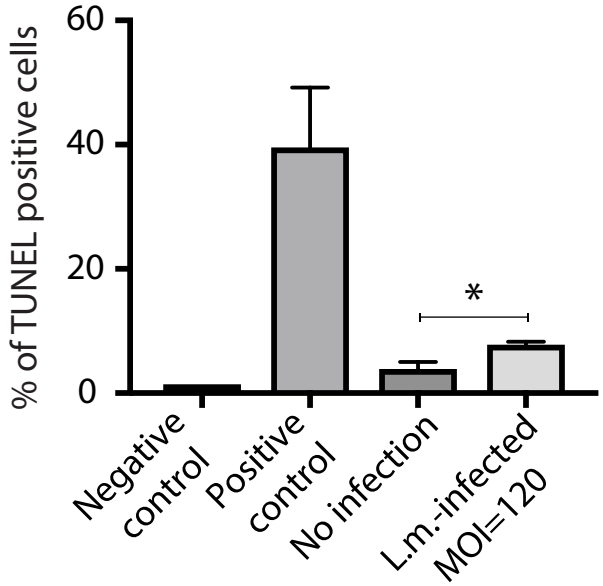

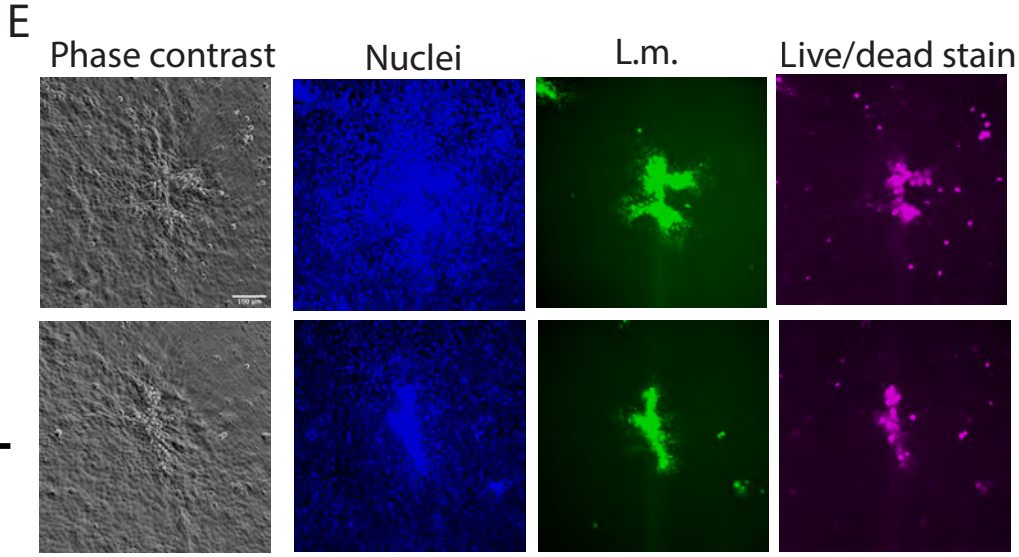

Supplemental Figure 12

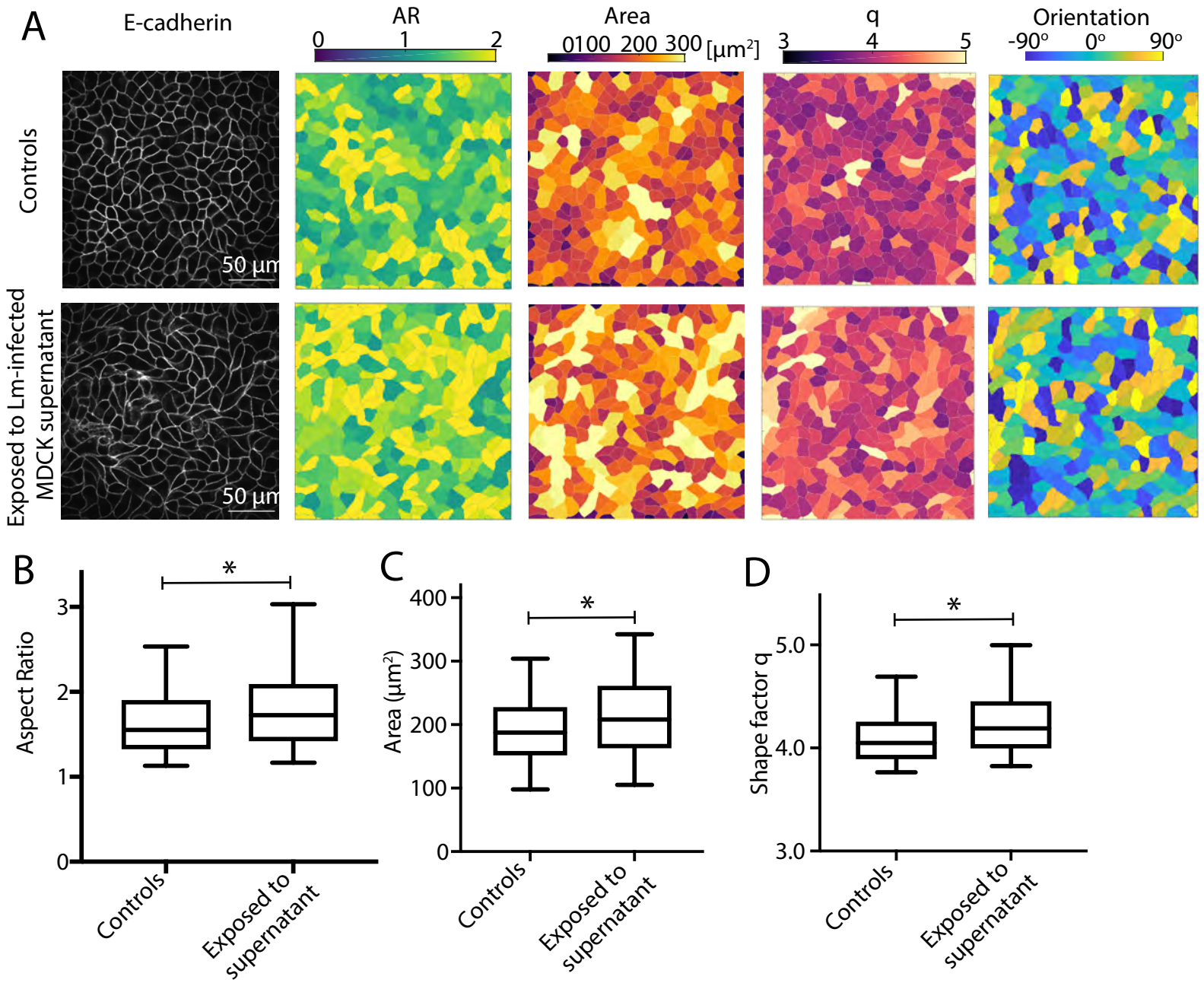

Supplemental Figure 13

A

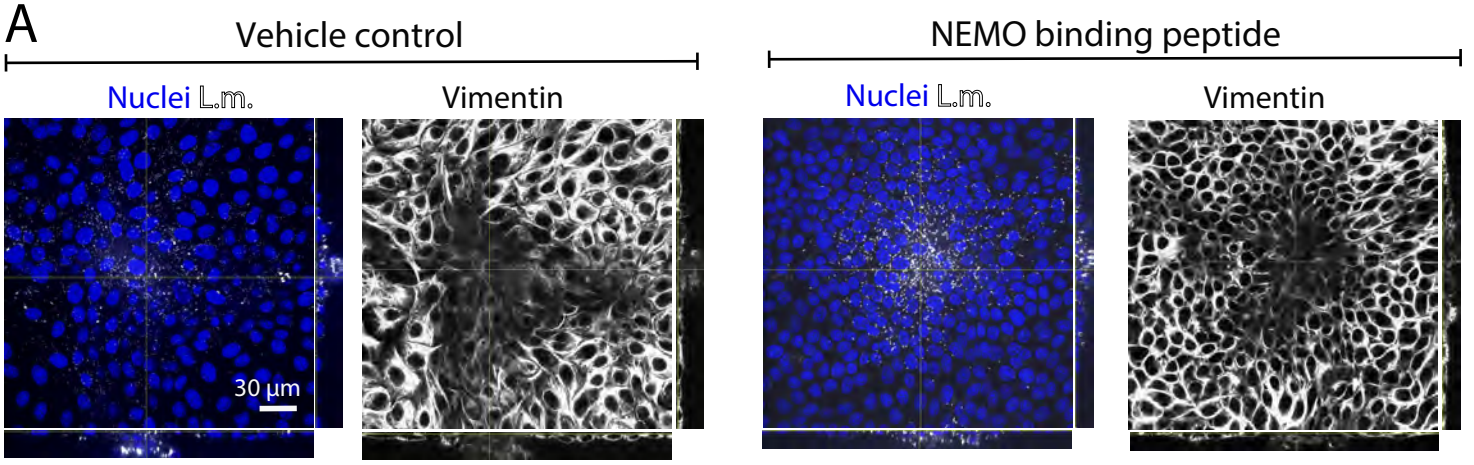

B

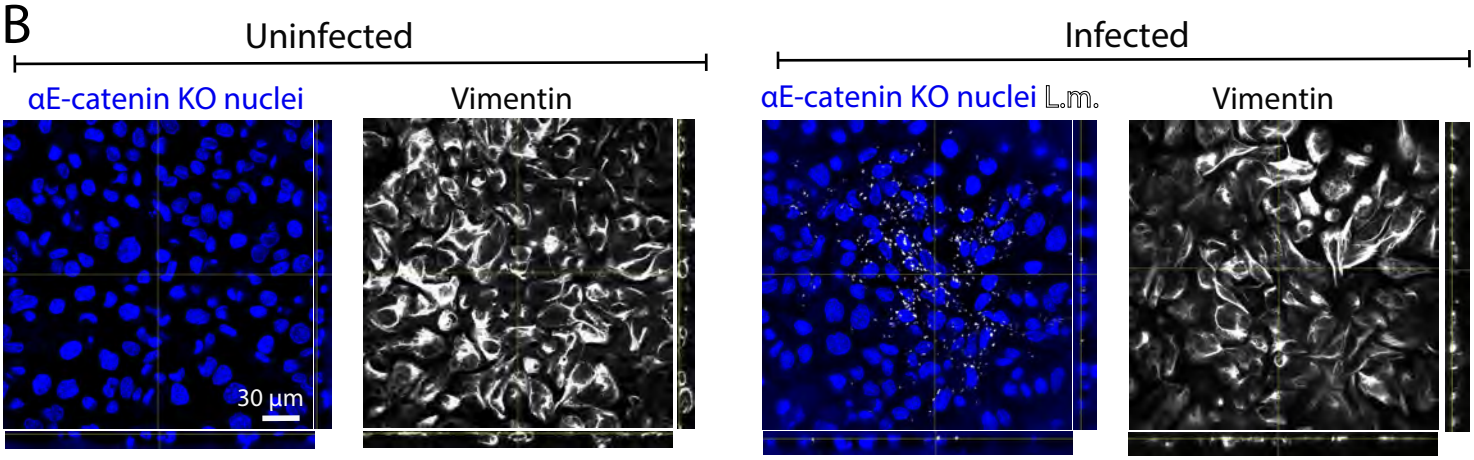

C

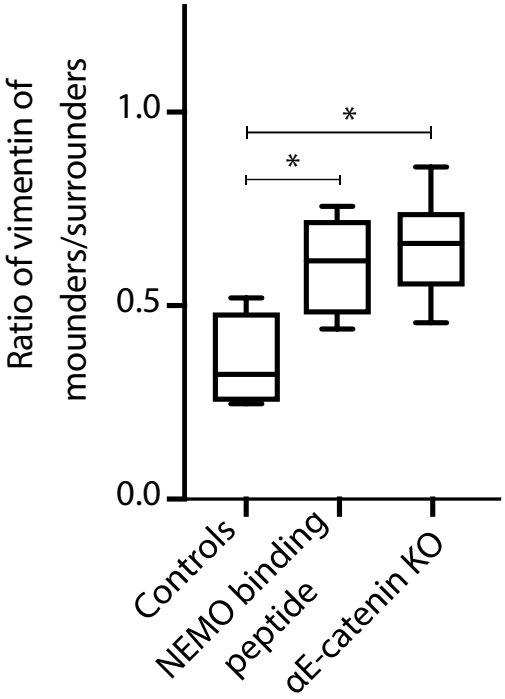
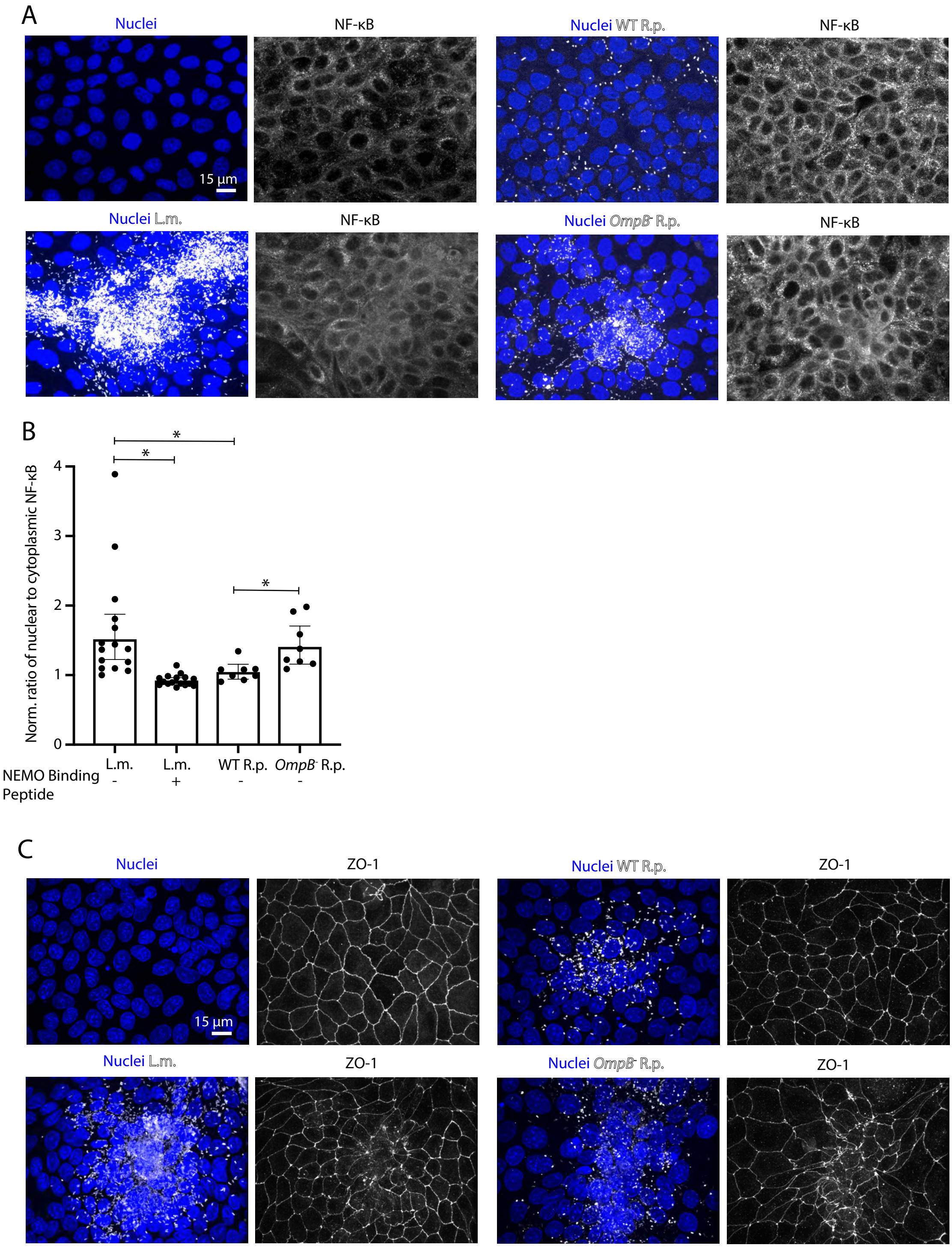
Supplemental Figure 14